Deuterium Nuclear Magnetic Resonance (NMR) and Rheology of Microgel Colloids at Ambient and High Pressure

by

© **Suhad Adnan Sbeih**
M.Sc., University of Jordan, 2009
B.Sc., University of Jordan, 2006

A thesis submitted to the
School of Graduate Studies
in the partial fulfillment of the
requirements for the degree of
Doctor of Philosophy

Department of Physics and Physical Oceanography
Memorial University of Newfoundland

January, 2018

St. John's Newfoundland

Abstract

Microgel colloids exhibit a polymer collapse transition resulting in a large reduction in colloid particle volume at high temperatures or pressures. They are of interest because of their potential for applications in areas, like drug delivery and chemical separation, that involve the uptake, encapsulation and release of small or biological molecules. The goal of this work is to obtain a microscopic understanding of the internal structure and microscopic dynamics of microgels by examining the temperature and pressure dependence of the collapse transition. Deuterium NMR (^{2}H NMR) has been used to probe the microscopic dynamics of crosslinked poly N-isopropylacrylamide (polynipam) chains, in microgel colloids, as a function of temperature and pressure for a series of four crosslink densities (C_d). Each crosslinked microgel colloids was synthesized with deuteron labels on the nipam backbone (d3 nipam). Macroscopic properties of unlabeled colloids having the same crosslink densities were characterized by dynamic light scattering (DLS) and rheology. Rheological characterization as a function of temperature (T) and particle concentration (C), and for 4 crosslink densities, showed that the microgel viscosity decreases as temperature is increased. The Krieger-Dougherty model of the relative viscosity as a function of volume fraction was employed for viscosity analysis. The measured viscosity in the colloidal regime (at high T, low C) collapsed onto one line when plotted against volume fraction. This yields a measure of the water content in the particles as function of T. The water volume fraction in the microgel particle at 45°C was always found to be ~ 0.6 for any C_d. ^{2}H NMR spectra of the d3 nipam suspensions for all C_d indicated freely moving chains at low temperature and a nearly immobilized fraction above 35°C. This is consistent with DLS observations of a transition from swollen to collapsed colloids. Nipam segments in the collapsed phase of the d3 nipam suspension were more mobile than those in the dry powder. This suggests significant amounts of water in the collapsed phase, a finding consistent with the rheology

observations. Variable pressure NMR (up to 90 MPa) showed a slight increase in transition temperature with pressure for all C_d values studied.

Acknowledgements

I would like to express my deep appreciation and gratitude to my supervisors Prof. Michael Morrow and Prof. Anand Yethiraj for their support, guidance, motivation, patience, and valuable efforts during my PhD program. Their great knowledge helped me a lot to become an expert in my field. Also, I would like to thank my supervisory committee, Dr. Kristin Poduska and Dr. Qiying Chen, for their useful comments during the annual meetings.

I would like to express my deep thanks to my parents, Dr. Adnan Sbeih and Mrs. Saida Sabri. Through their constant love and support I have achieved great things. They have accompanied me through bad times and good times. I hope some day that I will be the way they are. I would like to thank my sisters Tala Sbeih and Sawsan Sbeih and my brothers Dr. Adel Sbeih and Ezz Eldin Sbeih for their constant encouragement, sincere care and support. No matter how bad a situation is they always find a way to make me feel better.

I would like to thank my colleagues and friends at MUN, Gagandeep Sandhu, Nury Paula, Dr. Ahmed Oraby, Mona Braim, Zena Aljabal, Dr. Abdullah Alodhayb, Dr. Ahmad Almudallal, Ameera Alrashidi, Shahrazad Malek, Hadeel Alodus, Maryam Alharbi, Haifa Alqahtani, Hanin Alghaidi, and Khawlah Alfeid for their continuous support. They made my stay in St. John's joyful and lovely.

I am thankful for Dr. Valerie Booth for giving me the chance to use instruments for purification and characterization of my samples. I would like to thank Ms. Donna Jackman and Mr. Craig Skinner for their assistance in using the purification instruments in biochemistry department. In addition, I want to extend my thanks to the staff in physics department for their cooperation and support through my program.

Last but not the least, I would like to thank the German Jordanian University (GJU) for their encouragement and offering me the study leave for my PhD continuance. I would like to thank the Department of Physics and Physical Oceanography, the School of Graduate Studies at Memorial University, and the National Sciences and Engineering Research Council (NSERC) of Canada for the funding.

Contents

List of Figures

List of Tables

List of Abbreviations

nipam	N-isopropylacrylamide
polynipam	poly N-isopropylacrylamide
VPT	Volume Phase Transition
VPTT	Volume Phase Transition Temperature
pH	potential of Hydrogen
LCST	Lower Critical Solution Temperature
UCST	Upper Critical Solution Temperature
DNA	Deoxyribonucleic acid
TEM	Transmission Electron Microscopy
DWS	Diffusion Wave Spectroscopy
UV	Ultraviolet
MD	Molecular Dynamics
SASA	Solvent Accessible Surface Area
H-bonds	Hydrogen bonds
PEGMA	poly (ethylene glycol) methacrylate
NMR	Nuclear Magnetic Resonance

^{1}H NMR	Proton Nuclear Magnetic Resonance
^{2}H	Deuterium
^{2}H NMR	Deuterium Nuclear Magnetic Resonance
DSC	Differential Scanning Calorimetry
DLS	Dynamic Light Scattering
MASS	Magic Angle Spinning Sample
SANS	Small Angle Neutron Scattering
MSD	Mean Square Displacement
CLSM	Confocal Laser Scanning Microscopy
MAA	methacrylic acid
EA	ethyl acrylate
PCS	Photon Correlation Spectroscopy
QELS	Quasi-Elastic Light Scattering
rf	radio frequency
FID	Free Induction Decay
EFG	Electric Field Gradient
C-D bond	Carbon-Deuterium bond
QCC	Quadrupole Coupling Constant
BIS	N,N'-methylenebisacrylamide
SDS	Sodium Dodecyl Sulfate
KPS	Potassium Persulfate

KD	Krieger-Dougherty
SAOS	Small Amplitude Oscillatory Shear

List of Variables

T	temperature
P	pressure
C_d	crosslink density
C	concentration
ΔF_{mix}	free energy change for mixing
ΔU_{mix}	internal energy change for mixing
ΔS_{mix}	entropy change for mixing
dP	change in pressure
dT	change in temperature
χ	mixing parameter
ϕ	volume fraction
ϕ_{eff}	effective volume fraction
R_H	hydrodynamic radius
ΔS	change in entropy
ΔV	change in volume
$R_{swollen}$	radius of swollen particle

$R_{collapsed}$	radius of collapsed particle
$g(r)$	pair correlation function
R_e	Reynolds number
F_S	Stokes force
ζ	drag coefficient
D	Diffusion coefficient
$\dot{\gamma}$	shear strain rate
σ	shear stress
σ_0	yield stress
η_0	zero shear viscosity
η_∞	infinite shear viscosity
ω	angular frequency
G'	storage modulus
G''	loss modulus
δ	phase shift
η_{rel}	relative viscosity
$\hat{I}$	angular momentum
$\hat{\mu}$	magnetic moment
$\vec{B_0}$	magnetic field along z direction
$\hat{H_z}$	Zeeman Hamiltonian
$\hat{H_Q}$	Quadrupole Hamiltonian

ν	linear frequency
M_n	n^{th} spectral moment
T_{2e}	quadrupole echo decay time
T_1	spin-lattice relaxation time
A	quadrupole echo amplitude
τ	pulse separation
τ_c	correlation time
v_p	particle's volume
S	swelling factor
dt	dwell time
$m_{apparent}$	apparent exponent of power law

Chapter 1

Introduction to Microgels

Microgel particles are made of crosslinked polymers that form colloidal dispersions in water [1]. The particle sizes of microgel colloids range typically from 100 nm to 1 μm [2]. They undergo a volume phase transition from swollen to collapsed as temperature is raised. Due to their thermoresponsive nature, they have attracted much attention in recent years [1].

Thermoresponsive polymers that are made from poly N-isopropylacrylamide (polynipam) were first synthesized in the 1950s [3]. During recent decades, these thermo-sensitive polymer networks have been the subject of many investigations due to their potential use as drug delivery systems, tissue engineering techniques, and chemical separation media [2].

The focus on polynipam has increased because it can respond to external stimuli like temperature, pressure, pH, and electric fields [4–8]. The tunability of microgels makes them a good model in which to study the phase behavior of polymeric-colloidal suspensions as a function of temperature, pressure, C_d, pH or ionic strength, especially, around the volume phase transition temperature (VPTT) of the microgel. Further, responsive microgel particles provide the possibility to fabricate smart colloidal materials for applications as carrier systems, optical switches, or sensors [9]. This promotes questions about the features of the thermoreversible transition in soft matter that we are going to investigate. This work is done to develop a microscopic picture about the structure and dynamics of the nipam microgels.

1.1 Temperature dependent phase transition

A microgel particle is a hybrid between colloidal and polymeric systems and is often pictured as a dense core, made of crosslinked chains, and a fuzzy shell, made of loose chains (see Figure 1.1 (a)). Poly N-isopropylacrylamide (polynipam) is a polymer which has a lower critical solution temperature (LCST) approximately in the range of 30°C - 35°C [3]. When heated in water above the LCST, it undergoes a reversible phase transition from a swollen hydrated state to a collapsed and less hydrated state. Upon lowering the temperature, the microgel particles swell to about twice their collapsed volume [9].

Below the LCST, the microgel is highly solvated owing to hydrogen bonding between water molecules and amide residues of the polymer chains. Above the LCST, the hydrogen bonds are broken due to the increase in energy, and nipam polymer chains undergo a transition from an extended-coil to a collapsed-globule state [2,10]. In polynipam microgels, this coil-to-globule transition appears as the VPTT, and the volume of the particle is reduced by about half (see Figure 1.1 (b)). The volume transitions resulting from changes of temperature have been widely studied for polynipam microgels.

1.2 Swelling behavior

At room temperature these microgels have a low refractive index difference with water due to their high water content. At high temperatures, the particle volume is smaller and the refractive index difference with water is increased [1]. The swelling behavior of microgels is governed by imbalance between repulsive and attractive forces acting in the particles. For charged microgels, when ionic repulsion forces and osmotic swelling pressures exceed attractive hydrophobic interactions between nipam monomers, such as hydrogen bonding and van der Waals interactions, swelling occurs [2,6].

The equilibrium volume of a microgel particle happens when the net osmotic pressure

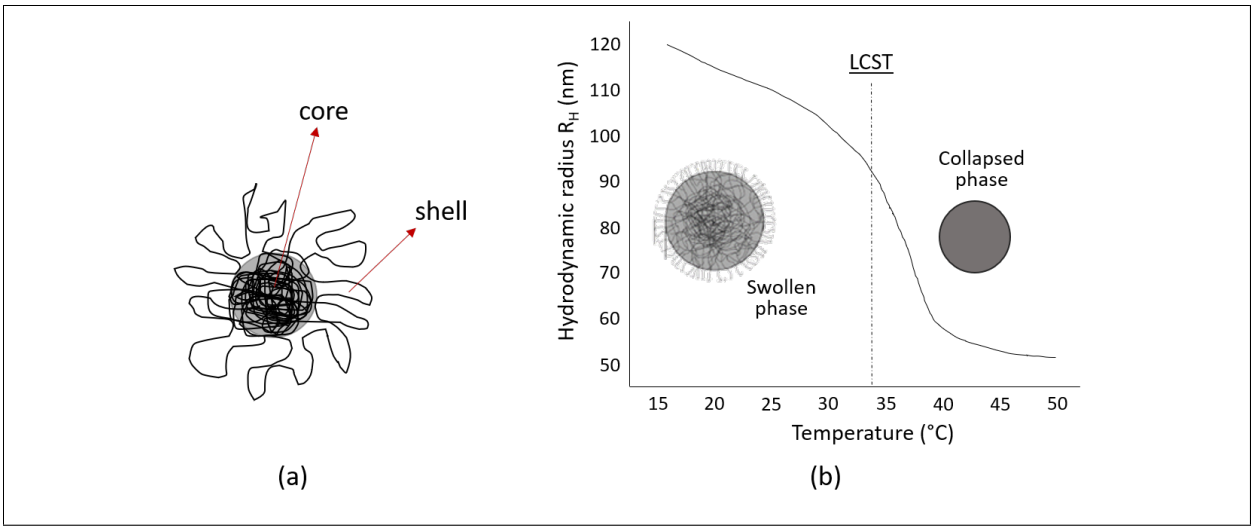

Figure 1.1: (a) A microgel particle consists of a highly crosslinked core and loose chains forming the shell (b) Swelling curve of polynipam: Hydrodynamic radius as a function of temperature, showing the LCST around 33°C. These are DLS measurements of our polynipam sample.

equals to zero. There are two contributions giving rise to the osmotic pressure: the elasticity of the microgel network and the polymer-solvent mixing energy [11]. The Helmholtz free energy change for mixing can be applied to the mixing of a polymer with a solvent at constant temperature, and is given by [12]

$$\Delta F_{mix} = \Delta U_{mix} - T\Delta S_{mix}. \tag{1.1}$$

The second term on the RHS is an entropic term and it always acts to promote mixing. The first term is energetic and is given by [13]

$$\Delta U_{mix} = \chi\phi(1-\phi)k_BT, \tag{1.2}$$

where ϕ is the volume fraction of the polymer and k_B is the Boltzmann constant. ΔU_{mix} can be positive (opposing mixing), zero (ideal mixtures) or negative (promoting mixing) depending on the sign of χ, the mixing parameter. Flory introduced this parameter [14]. It is a dimensionless measure of the differences in the interaction energies between species

in a mixture. It reflects the affinity between the polymer and the solvent molecules in a polymer-solvent mixture. The modeling of polymer solution free energy in terms of ϕ and χ is known as Flory-Huggins solution theory [12].

Typically, the coil-globule transition in polymers is associated with an upper critical solution temperature (UCST) not a LCST. In this case, collapse occurs with cooling and results from the polymer-polymer attractions being dominant at low temperature while entropic terms favor mixing at high temperature.

Whether the system has an UCST and thus a globule-coil (unmixed to mixed states) transition or a LCST and a coil-globule transition, with raising temperature, depends on the balance between the two terms in the free energy change for mixing, equation (1.2). In fact, the first term includes T implicitly, so both terms are entropic-like. With increasing temperature, a negative overall sign of ΔF_{mix} means an energetically favourable polymer-solvent mixing and an UCST while a positive sign indicates an energetically unfavourable polymer-solvent mixing and a LCST [15].

The coil globule transition in microgels arises from the hydrophobic interaction above LCST, where the hydrogen bonds that are formed between the amide nitrogen or the carbonyl oxygen of polynipam and the hydroxyl hydrogen from water molecules are broken. Thus the transition is likely driven largely by the increase of entropy of the water molecules being liberated from the polynipam network.

1.3 Hydrostatic pressure effect

The Clausius–Clapeyron equation describes how changes in pressure and temperature are related at a phase transition. It can be used to derive the pressure-temperature ($P-T$) diagram for the studied system. The slope of a phase boundary on a $P-T$ phase diagram

depends on the change in entropy (ΔS) and change in volume (ΔV) at the transition through

$$\frac{dP}{dT} = \frac{\Delta S}{\Delta V}. \tag{1.3}$$

The Clausius–Clapeyron equation gives a way to relate the effect of increasing the pressure to the thermodynamics of the system. In particular, whether the transition temperature increases or decreases with pressure can be related to the change in entropy and volume at a transition.

1.4 Previous studies

Polynipam has been progressively attracting researchers' attention over the past few decades. That is mainly because of its interesting thermal behavior in water solutions, that is the reversible solubility [3]. Much work has been focused on the properties of polynipam microgels. Saunders and Vincent [16] presented a detailed overview of the polynipam microgel system in terms of swelling, and small-angle neutron scattering (SANS) data. Although some theories of microgel swelling assume a uniform swelling and thus uniform crosslink distribution, they suggested that the internal structure of a microgel particle that is prepared by emulsion polymerization is not likely to consist of a homogeneous distribution of the cross-linking monomer, but that its density would decrease from the center to the outer edge of the microgel particle. Guillermo *et al.* [17] used proton NMR and reinforced the hypothesis about the heterogeneous internal structure of microgel particles by analysing the dependence of proton magnetic relaxation rates on polymer concentration. They distinguished different structural regions by detecting different proton mobilities. According to their results they suggested a core-shell structure with a relative core volume that increases with increasing crosslinker concentration.

Dynamic light scattering (DLS) measurements of the particle's hydrodynamic radius (and thus the particle's volume) as a function of temperature, were done by Senff and

Richtering [18] and Stieger *et al.* [19] and revealed that microgel swelling capacity is governed by the crosslinker concentration. The ratio of the particle volume in the swollen phase (measured at $T <$ LCST) to the particle volume in the collapsed phase (measured at $T >$ LCST), known as the swelling factor $(R_{swollen}/R_{collapsed})^3$, is usually presented as a measure of the swelling capacity. According to these studies, the swelling capacity was found to decrease as the crosslink density was increased. Similar measurements, using DLS, were performed by Contreras-Caceres *et al.* [20]. These papers produced swelling ratio *versus* crosslink density data that can be compared to results obtained from this work.

Andersson and Maunu [21] studied the phase transition in polynipam microgels with different crosslink densities using ^{1}H NMR, optical absorbance, and differential scanning calorimetry (DSC). They found that the proton NMR signals from the side chain protons and the backbone protons broadened and became nearly undetectable above the collapse transition. From absorbance, they found that the collapse transition temperature increases slightly with crosslink density. Their DSC measurements showed that transition enthalpy of the endothermic collapse transition decreases slightly with increasing crosslink density. In an earlier work, Badiger *et al.* [22] used solid-state ^{1}H magic angle spinning sample (MASS) NMR to study polynipam hydrogels with a higher transition temperature, about 42°C. They observed a significant increase in the line width as the gel went through the LCST. That was an indication of a significant attenuation of the polymer segments' mobility above the transition temperature.

Using SANS, Stieger *et al.* [19] also investigated the structural changes of polynipam induced by temperature and found that the core-shell inhomogeneous structure of the microgel particles is composed of a highly crosslinked core described by a radial box density profile and a shell in which the crosslink density decreases with increasing distance to the core and reaches zero at the surface of the microgel particle. They found that above LCST, the radial density profile shows a constant value over the whole particle volume that looks like the box profile of a homogeneous sphere (step function). However below LCST, the volume

fraction of the inner part of the particle decreased while the volume of the more diffuse shell increased [1, 19].

Dielectric spectroscopy studies done by Su *et al.* showed that the spatial distribution of crosslinking density does affect the swelling capacity but not the LCST [23].

Senff and Richtering [4] investigated the rheological properties of microgel colloids as a function of temperature. They employed the relative viscosity in dilute solution, measured by a viscometer, to determine the effective volume fraction ϕ_{eff} as a function of concentration for different temperatures. They did DLS experiments and measured the hydrodynamic radius R_H for different temperatures. They also performed rheology experiments and measured the viscosity as a function of the shear rate at different temperatures. Both R_H and ϕ_{eff} decreased with increasing temperature which was consistent with the decrease in shear viscosity and elastic properties with temperature. They found that the relative zero shear viscosity behavior for the microgel particles at low ϕ_{eff}, that is above LCST, resembled hard sphere behavior. On the other hand, microgel particles at high ϕ_{eff} had soft sphere elastic behaviors when they came into contact below LCST.

Scheffold *et al.* [9] used confocal microscopy studies to find the effective volume fraction of the microgel particles. It dropped from 0.9 to 0.2 with increasing temperature. They also investigated the effect of temperature on the particle's diffusion by measuring the mean square displacement (MSD) with time, using diffusion wave spectroscopy (DWS). Below LCST, they observed a plateau value of the MSD which characterizes elastic properties of the particles in the swollen phase while above the LCST, in the collapsed phase, a hard sphere like behavior was seen.

Chambon *et al.* [24] synthesized thermally responsive branched copolymers based on nipam and poly(ethylene glycol) methacrylate (PEGMA) monomers. They characterized the synthesized polymers using ^{1}H NMR measurements for the polymers in D_2O water. They also used DSC, DLS, and temperature dependent fluorescence experiments for polymer characterization. They found that the monomer residues and the short primary chain lengths

within these branched copolymer structures result in the effective dampening out of nipam thermo-responsivity [24].

Shewan and Stokes [25] employed the Krieger-Dougherty model of relative viscosity behavior in dilute and concentrated hard sphere suspensions to analyze viscosity in soft sphere microgel systems. They also studied the effect of particle elasticity on the viscosity of microgel suspensions at different volume fractions and found that there is no direct relation between the elasticity of the particle and the viscosity behavior up to the close-packing fraction.

Molecular dynamics (MD) simulations, at different temperatures, of the the thermo-responsive polynipam polymers were performed to investigate the origin of the LCST transition at the atomic level by Liu *et al.* [26]. From the measured dynamics trajectories of the polymer they derived the radius of gyration, the solvent (water) accessible surface area (SASA), the intermolecular and intramolecular hydrogen bonding, torsional energies, and side chain conformation. The LCST inferred from their predicted dependence of radius of gyration on temperature was in agreement with their experimental LCST value from visible spectrum transmittance. A consistent change in polymer hydrophobicity at the LCST was shown from the temperature dependence of the SASA. A significant decrease in SASA indicated the clear change of the polymer interaction with water and its transition from being hydrophilic to hydrophobic. At the transition, they also noticed a drop in the number of constantly formed intermolecular H-bonds between nipam and water molecules while almost no presence of intramolecular H-bonds between polymer parts. This was an indication that the polymer loses contact with water and becomes more hydrophobic and more compact at the transition. They observed a decrease in the torsional energy of the isopropyl groups that are in rotation with respect to the backbone, as temperature increased. That was inferred from the change in the conformational state of the polymer when going from being coil to globule.

Pressure is another important variable but the challenge of doing elevated pressure mea-

surements is reflected by the small number of reported experiments where the effect of hydrostatic pressure on microgel behavior was studied. Lietor-Santos *et al.* [5] studied the effect of hydrostatic pressure on the microgel particles and found that increasing pressure, to ∼350 MPa, results in a decrease of microgel particle volume. They interpreted their results as showing that the application of external pressure increases the Flory parameter of polymer-solvent mixing and thus decreases polymer-solvent miscibility. They also compared the pressure and temperature roles in microgel deswelling, over the studied ranges of pressure (0.1 MPa to 600 MPa) and temperature (20°C to 50°C), and found that they have similar roles. However, the pressure-induced deswelling is smoother than the temperature-induced deswelling which makes pressure more precise for tuning of microgel volume. They suggested that understanding the pressure effects on microgel swelling behavior can lead to significant improvements in technological applications such as oil extraction processes, where the pressure at the oil level is much greater than the pressure at the ground level.

Microgels have been proposed for applications like drug delivery. Wang *et al.* [27] designed microgels based on the nipam copolymers and DNA cross linkers, that exhibited highly selective killing efficiency for target cancer cells while also having excellent biocompatibility. Macromolecules of nucleotides (Aptamers) that have accurate recognition of cancer cells were introduced to nipam monomers and linker DNA by photo-initiated free radical polymerization. They characterized the thermoresponsive behavior of the synthesized DNA microgels using a microrheology device that employs the scattering DWS theory for the determination of their volume. The volume reduction happened between 32°C and 45°C. Also, they found that particle volume at 37°C decreases with time which implies continued drug release at the human body temperature. An anti cancer drug was encapsulated into the aptamer-functionalized DNA microgels. They examined the release profiles of the drug from the microgels utilizing ultraviolet (UV) spectroscopy at different temperatures and acidity level. They found that >70% and <20% of the encapsulated drug was released at 37°C (under acidic condition) and at 25°C, respectively, indicating the efficiency of the drug release in

the tumor region and the stability of the drug-encapsulated microgels at room temperature. They also used fluorescence microscopy imaging to investigate the drug uptake by the cancer cells. They found the relative targeted cancer cells viability was only about 30% after incubation with the drug loaded aptamer-functionalized DNA microgels.

Microgels have been the subject of numerous studies because of the constant demand to develop new technologies for applications such as food processing, water purification, the paint industry, and many medical and biological applications.

1.5 Motivating questions and experimental strategy

Microgels are an important class of condensed matter system with an interesting and potentially useful transition. They are particularly interesting as a model that can help us to understand systems whose constituent particles have internal structures that are sensitive to external conditions. Previous studies addressed questions about the phase behavior in colloidal suspensions such as: (1) How do material properties like the particle volume and internal structure respond to pressure?; (2) How do microgel properties depend on crosslink density?; (3) What is the nature of interparticle interactions in a colloidal suspension?; and (4) Why do colloidal microstructures have complicated behavior and how to simplify the problem of understanding it?

The understanding of the structure and dynamics of many solid polymers is of interest [26]. NMR spectroscopy in general is useful for these kinds of studies [24]. Solid state NMR, in particular, is a useful analytical method to study the dynamics of labeled segments in polymers and nanoparticles. However, the solid state NMR signal is very broad in comparison with solution NMR. Selective positions in the molecule can be independently investigated through this technique when they are labelled with an isotope having a low natural abundance. Deuterium NMR spectroscopy of solids is a powerful technique to provide a molecular-level information about segment reorientation in a material of interest [28].

It has been suggested that the microgel particles that are prepared by free radical polymerization generally consist of a dense core and a fuzzy shell with decreasing density probably due to the difference between monomer-monomer and monomer-crosslinker reaction rates [29]. The crosslink density in microgel particles affects the thermo-responsive behavior and degree of swelling or collapse at the transition. The previously proposed core-shell structure of the microgel particle by Stieger *et al.* [19] had a radial density distribution of the crosslinker from the center of the particle below LCST, and a constant value of crosslinker density over the whole particle above LCST. Callejas-Fernandez *et al.* [30] and Conley *et al.* [31] reinforced the assumption of the core-shell structure of microgels, the first by doing theoretical fitting of the experimental light scattering curves and the second by using super-resolution microscopy of dye labelled microgels. Crosslinking concentration is expected to have an important effect on the properties and the microstructure of microgels. A number of studies have examined the effect of crosslinking density and spatial distribution on the swelling factor of microgels [17–20, 23]. Most of these studies have focused on the transition in the microgels. The effect of crosslink density on microgel properties has been studied here using ^{2}H NMR after first using DLS to characterize particle size in a series of microgels synthesized with varying crosslinker to monomer ratios. Among the questions we asked during this work was: how does the average core volume vary with the fraction of crosslinks?

The effect of pH on microgel pressure-temperature ($P-T$) phase diagrams was studied by Kunugi *et al.* [32]. They used DLS at elevated pressures and subzero temperatures and measured the cloud point in aqueous solutions of microgels. The $P-T$ diagrams obtained showed that near or at atmospheric pressure, the transition temperature increased with increasing pressure but decreased with increasing pressure at pressures higher than 150 MPa. They also showed that the $P-T$ diagram can be fitted to a part of an ellipsoid curve in the temperature range from $\sim$0°C to 40°C, and in the pressure range from 0.1 MPa to 300 MPa. They found two regions on the transition curve at which $\Delta P/\Delta T > 0$ and thus $\Delta S > 0$ (see Clausius-Clapeyron equation (1.3)). An increase in entropy at these two points,

corresponded to two cases of phase transitions from the collapsed phase to the swollen phase: either a transition by increasing pressure up to ∼50 MPa and around 35°C, or a transition by increasing temperature near 0°C and at elevated pressures. In the current work, variable pressure deuterium NMR was used to study the effect of the crosslink density on the $P-T$ diagrams for microgel systems.

While there are models of microgel structure that are constructed to be consistent with SANS studies [1, 11, 19], there are no independent tests or quantitation of these models. In SANS, the model for the form factor assumes spherical particles and SANS is most useful at low particle packing fractions, where the form factor is independent of the packing fraction. Once particles overlap, they may depart from being spherical. This study also uses deuterium NMR spectroscopy to provide an independent characterization of microscopic dynamics of the microgel in the swollen and collapsed phases. Results obtained by ^{2}H NMR are less sensitive to particle shape. In order to simplify the interpretation of a studied microgel system, selective isotopic substitution in the polymer structure would be helpful.

A good understanding of how pressure affects the microgel particle structure, even at low pressures, might improve the usage of microgels in oil industry applications where these particles experience pressure variations. Variable pressure deuterium NMR, in the pressure range from 0.1 MPa to 140 MPa, is used to compare the properties of microgel phases obtained by varying pressure to those obtained by varying temperature.

Another parameter that influences the behavior of the microgel systems, is the crosslink density, C_d. While the effect of C_d on microgel properties has been studied extensively [17–20, 23], ^{2}H NMR studies provide a complementary approach to investigate how the C_d affect important microgel properties like polymer motions in the swollen phase, the partitioning of polymer between the core and the shell in the collapsed phase and the magnitude in the discontinuity in microgel properties at the transition.

Using particle coordinates and the pair correlation function $g(r)$ from Laser Scanning Microscopy (CLSM) and computer modeling, Mohanty *et al.* [33] showed that the micro

structure in suspensions of swollen microgel particles is consistent with a model of particles interacting through a soft Hertzian or harmonic potential. In that study, the goal was to obtain the interaction potential as a function of the interparticle distance between microgel particles in order to gain a better understanding of microgel phase behavior. The work reported here complements that study by investigating microgel particle elasticity and softness part of the rheological characterization of microgel.

The characterization of rheological properties is useful to investigate the phase transition behavior and the effect of microgel particle C_d on the viscosity behavior over a wide range of volume fractions. Tan *et al.* [34] previously investigated the rheological properties of four different systems of microgels by varying the degree of neuteralization of Methacrylic acid (MAA) groups, salt concentration, microgel crosslink density, and molar ratio of MAA to ethyl acrylate (EA) groups. They measured the viscosity in dilute to concentrated suspensions of the four different systems and their viscosity data all agreed with the Krieger-Dougherty model that can be used to describe the relative viscosity behavior in dilute and concentrated hard sphere suspensions. In our work, viscosities obtained from steady shear flow curve measurements were utilized to understand the phase behavior as a function of concentration and/or volume fraction. The Krieger-Dougherty model was employed to understand the crosslink density effect on the microgel viscosity behavior and to get detailed information on the volume fractions that constitute the polynipam and the water in the microgel particle. Another important objective of doing the rheology characterization was to relate the microscopic dynamics of the polymer segments revealed from ^{2}H NMR to the macroscopic behavior observed from rheology.

In this thesis, there are reported results of a series of studies of synthesized nipam polymers using deuterium NMR spectroscopy, DLS measurements, and rheological characterization with changing crosslink density C_d, and temperature. Also is described an investigation of microgel phase behavior when varying pressure by carrying out variable pressure NMR experiments.

In summary, a systematic study of how the nature of the collapse transition in microgels is affected by the crosslink density (C_d) has been carried out. The microgels were synthesized in our labs to control the C_d. Also, both deuterated and hydrogenated monomers were used in the synthesis for making samples needed to perform ^{2}H NMR and rheological studies. DLS was employed to characterize the particle volume for all the studied syntheses. ^{2}H NMR variable pressure experiments were conducted to study the effect of pressure on the phase transition in microgels.

1.6 Thesis structure

A brief background about diffusion and rheology in colloidal systems is presented in Chapter 2. That includes an overview of Brownian motion and the Stokes-Einstein relation, the Newtonian and non-Newtonian flow behaviours, the Cross model for the flow behaviour in pseudoplastic materials, steady shear and oscillatory shear tests, and the role of volume fraction in the viscosity of colloidal suspensions.

Theoretical background about solid state ^{2}H NMR is covered in Chapter 3.

In Chapter 4, the microgel synthesis, dynamic light scattering, and ^{2}H NMR experimental methods are discussed along with the equations that support the analytical methods.

The DLS determinations of particle volumes for the synthesized microgels at different crosslink densities are presented in the first part of Chapter 5. The second part deals with rheological study results for the hydrogenated microgels at different crosslink densities and concentrations.

^{2}H NMR experiments are presented in Chapter 6. Ambient pressure measurements for the sidechain and backbone deuterated polymers that were made at the same crosslink density are presented first. Results for differently crosslinked microgels of the backbone deuterated polymers are then presented. After that, variable pressure studies for the same set of differently crosslinked polymers, deuterated at the backbone, are presented along with

the resulting pressure-temperature phase diagrams.

Finally, the discussion and conclusion of this work are presented in Chapter 7.

Chapter 2

Diffusion and Rheology in Colloids and Gels

A colloidal dispersion consists of micron or sub micron size particles that are dispersed in a liquid medium. The addition of particles into a liquid usually affects its flow properties. Common examples of colloidal dispersions include paints, lotions, milk, and blood. When the particles in a colloidal dispersion are denser than the liquid they will tend to sediment because of the effect of gravitational forces. For small particles that are less dense than the liquid, they will undergo a continuous random thermal motion. The viscosity of the liquid medium will hinder the particles' motions [35]. The amplitudes of particles' motions tend to be increased by reducing the viscosity of the liquid medium, reducing the size of the particles, or increasing the temperature.

2.1 Reynolds number and Brownian motion

The dimensionless quantity of a fluid system, its Reynolds number, is the ratio of inertia to viscosity of the fluid. In other words, this number measures how fast the fluid is moving relative to how viscous it is. For a moving particle with radius R and velocity v in a liquid

of density ρ and viscosity η, the Reynolds number Re is given by [13]

$$Re = \frac{\rho v R}{\eta}. \tag{2.1}$$

The mechanism of fluid drag depends on the Re value. When $Re << 1$ the viscous forces of the fluid prevail the inertial forces. In this regime, the drag viscous force (Stokes force) F_S, is given by Stokes' law

$$F_S = 6\pi\eta R v. \tag{2.2}$$

The term $(6\pi\eta R)$ is defined as the the drag coefficient (ζ) between the liquid and the particle. In colloidal dispersions, where particles are small and Re is low, the so called "Laminar flow" occurs when the fluid is very viscous or is flowing in a slow and uniform motion with no disturbance.

The phenomenon of the constant random motion that is performed by small particles that exists in a medium was first observed by Robert Brown in 1827 and thus was named as "Brownian motion" [13]. In fact, these particles are freely moving in the 3 dimensions with a constant net force and a zero mean of the total particle displacement, at any time. However, the total mean square displacement (MSD) of the particle is proportional to time.

For a diffusing particle with radius R in a liquid with viscosity η, the diffusion coefficient (D) of the particle is related to the drag coefficient ζ, in Stokes' law, and is given by the Einstein formula [13]

$$D = \frac{k_B T}{\zeta}, \tag{2.3}$$

where k_B is the Boltzmann constant, and $k_B T$ is the thermal energy of the particle. The MSD of a diffusing particle in 3 dimensions is given by [36]

$$\langle \Delta r^2(t) \rangle = 6Dt. \tag{2.4}$$

2.2 Stokes-Einstein relation and hydrodynamic radius

Dynamic light scattering (DLS), also known as photon correlation spectroscopy (PCS) and quasi-elastic light scattering (QELS), measures time-dependent fluctuations in the intensity of scattered light that occur because the particles in a dilute suspension are undergoing Brownian motion. The measured intensity time correlation function is analyzed to obtain the relaxation rate distribution function. From the mean relaxation rate value, D is obtained [37]. This can be related to particle radius using the Stokes-Einstein equation,

$$D = \frac{k_B T}{6\pi\eta R_H}. \tag{2.5}$$

This equation relates D for a diffusing particle in a fluid of viscosity η at temperature T to its hydrodynamic radius R_H. This equation can be used only when assuming infinite dilution, that is if the volume fraction of the particles in the suspension, ϕ, is very small in a way that $K\phi << 1$, where K is a hydrodynamic factor that accounts for the slowing down of diffusion at finite volume fraction.

2.3 Rheology and flow behavior

2.3.1 Newtonian fluids, non-Newtonian fluids, and flow curves

When a shear stress (σ) is applied to a substance, it ideally behaves either like a Hookean solid that deforms elastically or like a Newtonian liquid that flows with a uniform viscosity. The Hookean solid produces a "shear strain" (γ) that is proportional to the applied stress σ and the proportionality constant is the elastic modulus (E). A Newtonian liquid, like water, flows with a constant "shear strain rate" ($\dot{\gamma}$) that is proportional to the applied stress and the proportionality constant is the liquid viscosity (η), that is constant with shear rate and time. Figure 2.1 (a) illustrates an example of applying a shear stress to a material. Some

materials show first elastic then viscous behaviors as a response to an applied stress with time evolution. These are called viscoelastic materials [13, 35].

Most fluids, in fact, have a shear rate dependent viscosity and thus they deviate from the Newtonian behavior. The main four common "non-Newtonian" behaviors are: shear-thinning, shear-thickening, Bingham plastic, and Bingham pseudo-plastic. Shear-thinning and shear-thickening fluids are characterised by decreasing and increasing viscosity, respectively, as a function of shear rate. A Bingham plastic requires a certain applied yield stress after which it starts flowing with a Newtonian behavior. Bingham pseudo-plastic materials have two stages of flow behavior. They start as a Bingham plastic and then they flow as a shear-thinning fluid. Examples of non-Newtonian fluids include a corn starch in water (as a shear thickening suspension), paints, ketchup, gels, and blood (as shear-thinning and Pseudo-plastic fluids).

The shear stress σ, in Pascals (Pa), *versus* the shear strain rate $\dot{\gamma}$, in s^{-1}, relation is called the "flow curve" and for a Newtonian liquid is given by

$$\sigma = \eta\dot{\gamma}, \tag{2.6}$$

where the slope represents the fluid viscosity, η in (Pa·s). Figure 2.1 (b) shows the flow curves for various Newtonian and non-Newtonian fluids [38]. For a Bingham plastic (or yield stress fluid), the relation has the form $\sigma = \eta\dot{\gamma} + \sigma_0$, where σ_0 is the initial "yield" stress before flow begins.

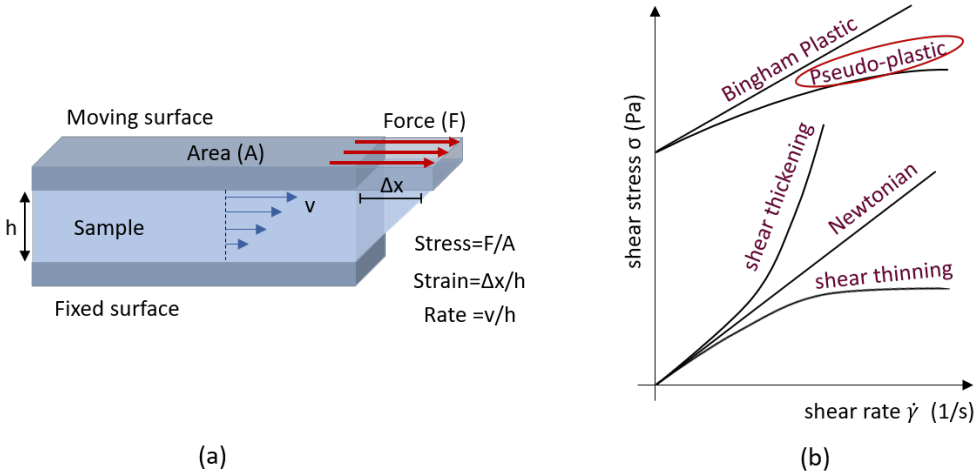

Figure 2.1: a) Schematic representation of applying a shear stress to a sample. b) Flow curves for most common types of fluids. Gels are considered as pseudo-plastic fluids.

For most polymers η is a function of the shear rate, $\eta(\dot{\gamma})$. The flow curve is non-linear, and may have a yield stress behavior (with a σ_0 value). A power law model can generally describe a shear-thinning and shear thickening viscosity behavior. The stress-shear rate relation can then be approximated by a power law as

$$\sigma = K\dot{\gamma}^n, \tag{2.7}$$

where K has the unit of (Pa·s^n) and is called the consistency coefficient. The exponent n is a dimensionless number that indicates the closeness to Newtonian behavior: n=1 for Newtonian; n <1 for shear-thinning; and n >1 for shear thickening fluid. The stress-shear rate relation will be linear on a double logarithmic scale, since the relation can be written as

$$\log\sigma = n * \log\dot{\gamma} + \log K. \tag{2.8}$$

The slope of $\log\sigma$ *versus* $\log\dot{\gamma}$ plot gives n, and the y-intercept gives K.

2.3.2 Review of gels and the Cross equation

Polymer dispersions at high concentrations exhibit a gel-like flow behavior. Over a wide range of shear rate, they show a three-stage viscous response: (a) Newtonian regime at low $\dot{\gamma}$ with a constant zero-shear viscosity η_0 that is followed by; (b) a shear-thinning behavior over a middle $\dot{\gamma}$ range with a decreasing viscosity that can be described by the power law; and (c) another Newtonian regime at high $\dot{\gamma}$ that is characteristic with a constant infinite-shear viscosity η_∞. In 1965, Cross [39] derived a flow equation that reasonably describes a broad range of pseudo-plastic systems and over a wide shear rate range. The Cross model assumes the three stages in the (viscosity-shear rate) behavior in polymers, and is a well established model in literature [4, 40, 41]. This model can be used to find the η_0 and η_∞ values, and is given by the equation

$$\eta - \eta_\infty = \frac{\eta_0 - \eta_\infty}{1 + (\tau\dot{\gamma})^m}, \tag{2.9}$$

where τ is a consistency constant that is related to the relaxation time of the polymer in solution and m is the power law exponent. While Cross [39] had suggested a value $m = 0.67$, it is reasonable [42] to treat m as a variable whose constancy as a function of concentration reflects that there is no qualitative change in the character of the material. Figure 2.2 shows the viscosity-shear rate relation, on a logarithmic scale, consisting of the three parts: low shear viscosity plateau; middle shear power law region; and high shear viscosity plateau, as suggested by Cross. For the case where $\dot{\gamma} << 1$, the Cross equation reduces to $\eta = \eta_0$ and gives the η_0, the low shear viscosity plateau value. On the other hand, when $\dot{\gamma} \to \infty$, the equation reduces to $\eta = \eta_\infty$ and thus gives η_∞, the high shear plateau value.

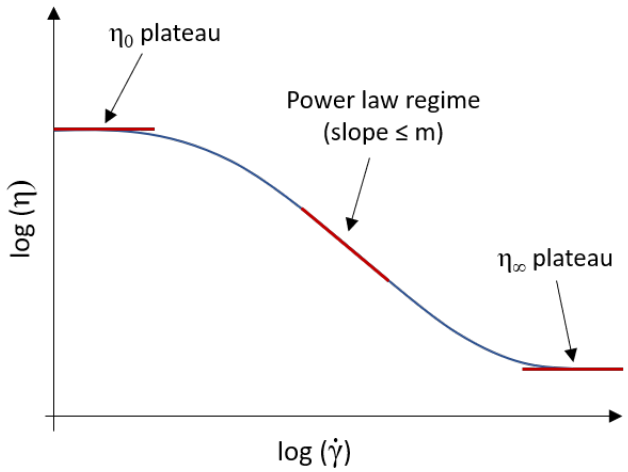

Figure 2.2: A schematic representation of the Cross model of the viscosity-shear rate relation for gels and pseudo-plastic polymers.

In the middle range where $\dot{\gamma}$ is large or $\tau\dot{\gamma} >> 1$, the Cross equation becomes

$$\eta - \eta_\infty = \frac{\eta_0 - \eta_\infty}{(\tau\dot{\gamma})^m}.$$

In the case when $\eta_0 >> \eta_\infty$, the equation becomes

$$\eta \sim \eta_0(\tau\dot{\gamma})^{-m},$$

and this is the "power law regime". The measured slope in this regime will be less than m, but will approach m as η_0/η_∞ increases.

2.3.3 Rotational steady shear using a cone-plate rheometer

The rheometer is used to obtain the flow curves of a fluid by performing the rotational steady shear test on it. The cone and plate geometry of a rheometer consists of a cone that is rotating and a fixed plate, as shown in Figure 2.3. The sample fills the gap between the cone and the plate. The angle between the cone surface and the plate, θ, is usually small ($< 4°$) [38, 43]. The cone is rotated and the torque (τ) is measured, by a sensitive torque

transducer, at different speeds of rotation (ω). By controlling the deformation (or strain) rate, the resulting shear stress is obtained from the measured torque on the cone. The shear stress as a function of shear strain rate (flow curve) is obtained.

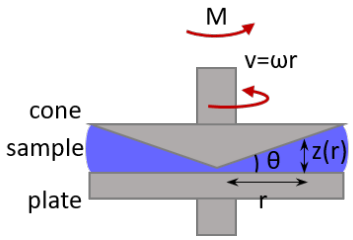

Figure 2.3: The cone-plate rheometer configuration, with an angle (θ). This geometry has a uniform shear rate through the sample.

The gap height z is a function of the radius of the cone, and thus the sample thickness is also a function of the radius. But the shear strain rate $\dot{\gamma}$ through the sample is a constant value that is independent of the radius,

$$\dot{\gamma} = \frac{\omega}{\tan\theta} = \text{constant}. \tag{2.10}$$

Because of that, the cone and plate is the most popular geometry for studying non-Newtonian fluids. It can also be used in an oscillating mode to measure elastic properties.

2.3.4 Small amplitude oscillatory shear

In order to determine the mechanical and viscoelastic properties of a material, time dependent deformations are tested by applying a harmonically oscillating shear strain,

$$\gamma(t) = \gamma_0 \exp(i\omega t), \tag{2.11}$$

to which the material responds with a harmonic shear stress. The resulting stress in a purely elastic-solid is in phase with the deformation (strain). In purely viscous-liquid, the stress is $\pi/2$ out of phase with the strain. Viscoelastic materials exhibit a behavior somewhere in the

middle of these two types of materials, and thus a lag in phase δ (in between 0 and $\pi/2$) [43].

The oscillating strain with a frequency ω is applied to the material and the phase difference between the oscillating strain and stress is measured. Then the stress is given by [12]

$$\sigma(t) = \sigma_0 \exp[i(\omega t + \delta)]. \tag{2.12}$$

Also, the ratio of the amplitudes,(σ_0/γ_0), can be measured to give a parameter G^*, the Dynamic Modulus of Elasticity, which can be written as

$$\begin{aligned} G^* = \frac{\sigma(t)}{\gamma(t)} = \frac{\sigma_0}{\gamma_0}\exp(i\delta) &= \frac{\sigma_0}{\gamma_0}(\cos\delta + i\sin\delta) \\ &= \frac{\sigma_0}{\gamma_0}(\cos\delta) + i\frac{\sigma_0}{\gamma_0}(\sin\delta) \\ &= G' + iG'', \end{aligned} \tag{2.13}$$

where G' is the storage modulus that is related to the elastic response and G'' is the loss modulus that is related to the viscous response of the viscoelastic material. In fact, the oscillatory stress can be written in terms of the elastic modulus E and the viscosity η as

$$\sigma(t) = E\gamma(t) + \eta\dot{\gamma}(t), \tag{2.14a}$$

where E and η are

$$E = G' \text{ and } \eta = \frac{G''}{\omega}. \tag{2.14b}$$

Also, from equation (2.13), the ratio of the loss to storage moduli G''/G' is given by the tangent of the phase difference δ and is called the "loss tangent" [12]

$$\tan\delta = \frac{G''}{G'}. \tag{2.15}$$

At low frequencies, $G' > G''$ for an elastic solid while $G'' > G'$ for a viscous liquid. Thus the loss tangent is < 1 for the elastic material but > 1 for the viscous one.

2.4 Role of volume fraction in rheology of colloidal dispersions

Colloidal dispersions display phase behaviors that depend on temperature, pressure, and suspension concentration. The phase behavior of a hard sphere suspension depends only on the concentration of the suspension, or particularly, the volume fraction of the particles (ϕ) that is defined as the ratio of the volume occupied by the particles to the total volume of the suspension [18]. Figure 2.4 illustrates the hard sphere phase diagram which includes fluid and crystalline phases as well as glassy states [44].

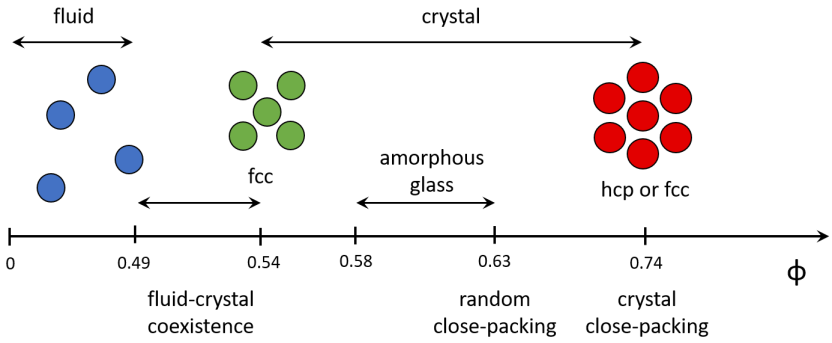

Figure 2.4: Hard spheres phase diagram as a function of the volume fraction ϕ.

2.4.1 Einstein and Batchelor equations

From Einstein's work [45] on dilute suspensions of hard spheres, the relative viscosity η_{rel} (that is the ratio of the suspension zero-shear viscosity to the solvent viscosity) and the suspension volume fraction are related by

$$\eta_{rel} = 1 + 2.5\phi, \tag{2.16}$$

where $\eta_{rel} = \eta_0/\eta_s$. Batchelor [46] has developed an expression relating the relative viscosity of semi-dilute suspensions of hard spheres to the volume fraction, that is given by

$$\eta_{rel} = 1 + 2.5\phi + 5.9\phi^2. \tag{2.17}$$

This expression is expected to be quantitatively applicable only in the low volume fraction regime [13, 35].

2.4.2 Krieger-Dougherty expression for concentrated suspensions

A phenomenological formula for the relative viscosity as a function of volume fraction was proposed by Krieger and Dougherty [47] in order to fit experiments over a larger possible range of volume fractions. The Krieger-Dougherty equation is given by

$$\eta_{rel} = \left(1 - \frac{\phi}{\phi_{max}}\right)^{-2.5\phi_{max}}, \tag{2.18}$$

where ϕ_{max} is the maximum hard sphere random packing fraction, 0.63 [44]. The relative viscosity, η_{rel}, therefore goes to ∞ at $\phi = \phi_{max} = 0.63$. A practical reference point is $\eta_{rel} = 1000$, which occurs when

$$\phi \approx 0.988\phi_{max} \approx 0.62. \tag{2.19}$$

Microgel particles behave like soft spheres that can overlap at low temperatures, in the swollen phase, and thus can have volume fractions that are higher than 1. Also, they are expected to have low volume fractions at high temperatures where they are collapsed and behave more like hard spheres. If the particles are assumed to be hard-sphere-like in the collapsed phase, then the Krieger-Dougherty formula can be used to estimate volume fraction in that phase and dependence of particle volume on temperature, from DLS, can be used to extend the estimation of the effective volume fraction to other temperatures [25].

Chapter 3

Solid State Deuterium NMR Theory

3.1 Introduction

The reason to use deuterium NMR to study soft matter is that it is sensitive to the amplitude of motions that modulate the orientation-dependent quadrupole interaction [48] and can thus be used to characterize molecular segment reorientation and how it changes at a transition.

The nuclear magnetic resonance phenomenon arises from the ability of a nucleus in a magnetic field to resonate upon the absorption of radio frequency energy (generated by an rf pulse) that is tuned to match the energy difference between nuclear energy levels. This requires that the nucleus possesses an intrinsic property called spin, and it has to be non zero spin. Nuclear spin is represented by the angular momentum operator $\hat{I}$ associated with a spin quantum number I. A spinning nucleus possesses a magnetic moment $\hat{\mu}$ and spin angular momentum $\hbar\hat{I}$ which are related by the gyromagnetic ratio γ as $\hat{\mu} = \gamma\hbar\hat{I}$.

In the presence of a strong external magnetic field $\vec{B_0}$ along the z axis, an interaction

between the magnetic field and the nuclear spin is governed by the Zeeman Hamiltonian [49]

$$\begin{aligned} \hat{H_Z} &= -\hat{\mu} \cdot \vec{B_0} \\ &= -\gamma \hbar \hat{I} \cdot \vec{B_0} \\ &= -\gamma \hbar \hat{I_z} B_0 \end{aligned} \tag{3.1}$$

Defining the Larmor frequency as $\omega_0 = -\gamma B_0$, the Zeeman Hamiltonian becomes $\hat{H_Z} = \hbar \omega_0 \hat{I_z}$.

For deuterium, a spin-1 nucleus, $\hat{I_z}$ has three eigenstates with magnetic quantum numbers $m = +1$, 0, -1. In the absence of a magnetic field, they are degenerate. In the presence of a magnetic field, the Zeeman Hamiltonian applies and the energies of the three states are split. According to Zeeman splitting, the three energy states have the energies $E_m = m\hbar\omega_0$, as shown in Figure 3.1(b). Because of the minus sign in the definition of the Zeeman Hamiltonian above, the highest energy level corresponds to the case when the spin is antiparallel to the magnetic field, and the lowest energy level corresponds to the case when the spin is parallel to the magnetic field [49].

A sample consists of a large number of spins. At thermal equilibrium, there is a Boltzmann distribution of nuclear spins over these three states. The relative populations of these energy states are determined by this distribution. The states at the highest energy level will have the smallest population and the net magnetization of the spins over the sample will be in the direction of the static magnetic field $\vec{B_0}$. For deuterium, the difference in relative populations between the highest energy state (with $m = -1$) and the lowest energy state (with $m = +1$) at room temperature is given by $\frac{2}{3}(\hbar\gamma B_0/k_B T)$, where k_B is Boltzmann constant [49]. Because of the small value of the gyromagnetic ratio in deuterium ($\gamma = 41 \times 10^6$ rad$\cdot$s$^{-1}\cdot$T^{-1}), the relative difference in populations is very small. It is about 6.6×10^{-4} in a 9.4 T magnet, for example.

If an rf pulse of the correct frequency and duration is applied in the transverse plane (by an oscillating field), it will tip the net magnetization away from the z axis. The net magne-

tization will then precess about the applied field at the Larmor frequency. This precession is what we actually measure in an NMR experiment. The precessing magnetization vector in the rf coil induces a current in the same coil. This is the free induction decay FID signal that we detect [50]. For deuterium, the spectrum is symmetric, and there are actually two magnetizations precessing in opposite directions so the current in the coil is excited by an oscillating magnetization.

3.2 The quadrupole interaction

Deuterium is a spin-1 nucleus and it thus has a nonspherical charge distribution in the nucleus. This anisotropic charge distribution produces an electric quadrupole moment which is written as eQ [51], where Q is the scalar electric quadrupole moment of the nucleus and e is the proton electric charge e in the nucleus. We use deuterium labeled molecules where the hydrogen atoms in carbon-hydrogen (C-H) bonds locations are replaced by deuterium atoms, so all the deuterons are in carbon-deuterium (C-D) bonds. For a C-D bond there is an electric field gradient (EFG), that depends on the environment of the nucleus as determined by the charge distribution in the chemical bond. The principal axis component of the EFG along the C-D bond which is given by eq, where q is the scalar electric field gradient of the bond and e is the electron charge.

The quadrupole interaction is the electrostatic interaction of the nuclear quadrupole moment and the electric field gradient at the position of the nucleus. The Zeeman levels of a nucleus with a quadrupole moment are perturbed by the quadrupole interaction. The quadrupole interaction depends on the orientation of the electric field gradient in the chemical bonds with respect to the applied field. It is represented by the Quadrupole Hamiltonian $\hat{H}_Q$ and given by [52]

$$\hat{H}_Q = \frac{e^2qQ}{4I(2I-1)}\left[3\hat{I}_z^2 - I(I+1) + \frac{1}{2}\eta\left(\hat{I}_+^2 + \hat{I}_-^2\right)\right] \tag{3.2}$$

in the laboratory reference frame. In this equation $\hat{I_{\pm}} = \hat{I_x} \pm i\hat{I_y}$.

The quadrupole interaction is much smaller than the Zeeman interaction, so it can be treated as a perturbation. Figure 3.1 (c) shows how this interaction shifts the Zeeman energy levels of a deuterium spin. The total Hamiltonian for a deuterium nucleus is given by

$$\hat{H} = \hat{H_Z} + \hat{H_Q} \tag{3.3}$$

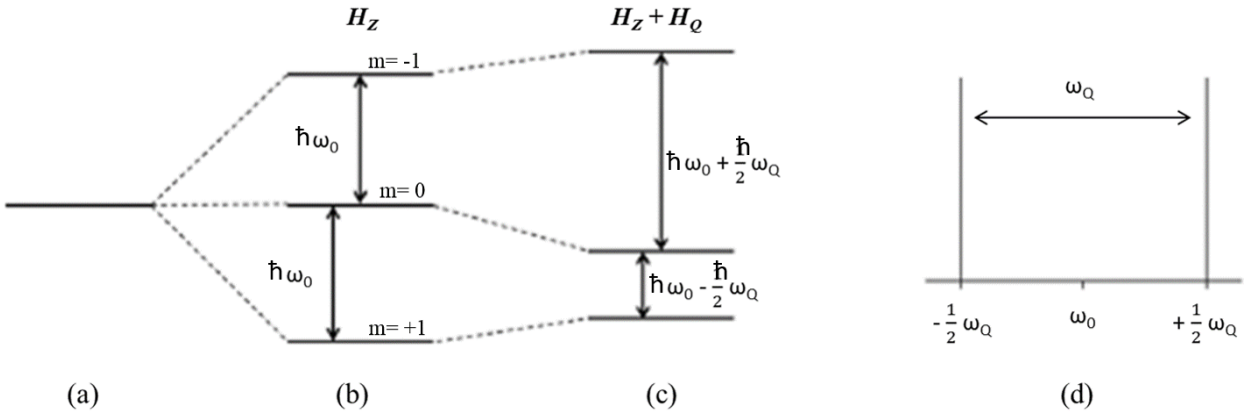

Figure 3.1: Energy levels for a spin-1 nucleus: (a) when $B_0 = 0$ (b) Zeeman splitting in the presence of B_0 (c) Quadrupole interaction effect (d) The corresponding spectrum: two lines, symmetric about ω_0, coming from the two transitions of the deuteron nucleus (m = -1 $\rightarrow$ 0 and m = 0 $\rightarrow$ +1).

The EFG is represented by the symmetric and traceless second rank tensor (V_{ik}) and defined by two independent components in the principal axis system frame: the electric field gradient $V_{zz} = eq$ and the asymmetry parameter $\eta = V_{xx} - V_{yy}/V_{zz}$.

The principal axis system of the electric field gradient (EFG) tensor is defined by the C-D bond and the z direction is normally chosen to be along the bond direction, so that the EFG tensor of a given C-D bond is initially defined in a molecule-fixed frame. The Hamiltonian is written in the lab frame so it is necessary to transform the EFG (V_{ik}) from the molecule-fixed reference frame into the laboratory-fixed coordinate system [53]. This can be accomplished by using Wigner rotation matrices in the spherical coordinates (θ, ϕ). Then the quadrupole

Hamiltonian becomes [52]

$$H_Q = \frac{e^2qQ}{4I(2I-1)}\left[3\hat{I}_z^2 - I\left(I+1\right)\right]\left[\frac{1}{2}\left(3\cos^2\theta - 1\right) + \frac{1}{2}\eta\sin^2\theta\cos 2\phi\right]. \tag{3.4}$$

The total Hamiltonian is then given as

$$H = \hbar\omega_0\hat{I}_z + \frac{e^2qQ}{4I\left(2I-1\right)}\left[3\hat{I}_z^2 - I\left(I+1\right)\right]\left[\frac{1}{2}\left(3\cos^2\theta - 1\right) + \frac{1}{2}\eta\sin^2\theta\cos 2\phi\right]. \tag{3.5}$$

For $I = 1$, the energy eigenvalues corresponding to the total Hamiltonian are given by

$$E_m = m\hbar\omega_0 + \frac{e^2qQ}{4}\left[3m^2 - 2\right]\left[\frac{1}{2}\left(3\cos^2\theta - 1\right) + \frac{1}{2}\eta\sin^2\theta cos2\phi\right] \tag{3.6}$$

Since η for a C-D bond is small (0.007) and can be neglected, the last term vanishes and the energy becomes

$$E_m = m\hbar\omega_0 + \frac{e^2qQ}{4}\left[3m^2 - 2\right]\left[\frac{1}{2}\left(3\cos^2\theta - 1\right)\right] \tag{3.7}$$

The second term in equation 3.7 represents the first order quadrupole interaction perturbation of the Zeeman energy levels. It shifts the levels with $m = \pm 1$ up in energy and the one with m=0 down in energy by twice as much [49]. The energy difference between adjacent energy levels has two different values now and therefore two transitions occur at the resonant frequencies $(\omega_0 \pm \frac{1}{2}\omega_Q)$, provided that ω_Q is defined as

$$\omega_Q = \frac{3}{2}\frac{e^2qQ}{\hbar}\left[\frac{3\cos^2\theta - 1}{2}\right]. \tag{3.8}$$

The spectrum for a sample containing static C-D bonds, with a single orientation, shows a "doublet" of two lines symmetric about the Larmor frequency ω_0 as in Figure 3.1(d).

3.3 Pake powder pattern

The Euler angle θ (in the preceding equation) defines the angle between the EFG principal axis of the C-D bond and the magnetic field. Dry powders consist of a large number of molecules that are randomly oriented. The splitting for a deuteron on a particular C-D bond will be

$$\Delta\nu_Q(\theta) = \frac{3}{2}\frac{e^2qQ}{h}\left[\frac{3\cos^2\theta - 1}{2}\right], \tag{3.9}$$

where $(\frac{e^2qQ}{h})$ is the quadrupole coupling constant, QCC, which is 167±10 kHz for a C-D bond [54]. The ^{2}H NMR spectrum will consist of a superposition of doublets with quadrupolar splittings representing all possible orientations. This line shape, shown in Figure 3.2 (a), is called the "Pake doublet".

For static, randomly oriented C-D bonds, the splitting magnitude, for a given deuteron on a chain of carbons labelled d in this work, depends only on θ which can have any value between 0° and 90° [28], for a given spectral component, with weighting proportional to the orientation probability. So, the highest intensity "edges" (θ = 90° in Figure 3.2(a)) of the spectrum come from the perpendicular orientation and the lowest "shoulders" (θ = 0° in Figure 3.2(a)) comes from the parallel orientation of the C-D bond with respect to the external magnetic field [55]. The quadrupolar splitting is measured between the highest intensity "edges" corresponding to θ=90°. By substituting θ=90° in equation (3.10), the maximum quadrupole splitting is found to be ∼125 kHz [54]. The powder pattern with this splitting can be labelled the "rigid lattice spectrum".

If a C-D bond is attached to a molecular segment that is undergoing axially-symmetric reorientation on a time scale shorter than $\sim 10^{-5}$ s, then the transformation from the molecule-fixed frame to the lab frame must be done in two steps. In this case, θ becomes the instantaneous angle between the C-D bond and the symmetry axis for reorientation [56] and β is introduced as the angle between the motional symmetry axis and the magnetic field. The

splitting for a deuteron on a particular molecular segment then becomes [57]

$$\Delta\nu_Q(\theta,\beta) = \frac{3}{2}\frac{e^2qQ}{h}\left[\frac{3\cos^2\beta - 1}{2}\right]\left\langle\frac{3\cos^2\theta - 1}{2}\right\rangle. \tag{3.10}$$

The spectrum is again a superposition of doublets but now corresponding to a spherical distribution of the angle β as shown in Figure 3.2(a). The splitting of the Pake doublet is scaled by the last factor, in equation 3.10, which is defined as the orientational order parameter for a C-D bond,

$$S_{CD} = \left\langle\frac{3\cos^2\theta - 1}{2}\right\rangle. \tag{3.11}$$

The average is over the molecular reorientation. Molecular motions with correlation times shorter than the splitting timescale can contribute to motional averaging of the quadrupole interaction. Motions with longer correlation times (adiabatic motions) can only affect echo formation. Motions having correlation times that are shorter than the quadrupole splitting time scale $(\Delta\nu_Q)^{-1}$, will modulate the Euler angles. Accordingly, the splitting of a C-D bond on a chain of carbons (d) of the prominent edge features in the Pake powder pattern will be reduced by motional averaging. We assume that the segment motions modulate θ on a time scale that is short compared to the NMR time scale so that the average is over "fast" motions, and motional narrowing is due to reorientation about randomly oriented symmetry axes. The angle θ varies rapidly while β changes too slowly to contribute to averaging of the quadrupole interaction.

3.4 Segment reorientation and orientational order

The average orientational order of a molecule can be described in terms of an order tensor [52]. If a molecule has a 3-fold axis of symmetry, then the order tensor needed to describe the orientational order of a rigid molecule can be reduced to one parameter S_{zz}. The average

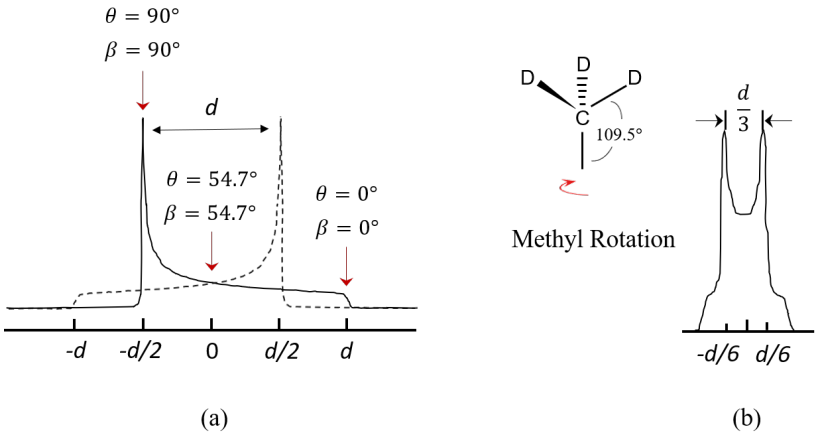

Figure 3.2: (a) Pake powder pattern: the total line shape is composed of two powder line shapes (solid and dashed) while one is the mirror image of another. Angle θ applies for static C-D bonds while β for axially symmetric reorientation. (b) C-D bond rotation about the methyl axis reduces the splitting of a C-D bond on a chain of carbons, d, by a factor of one third.

quadrupole splitting can be expressed as [52]

$$\langle \Delta\nu_Q \rangle = \frac{3}{4}\frac{e^2qQ}{h}S_{zz}. \tag{3.12}$$

Different parts of the molecules may move differently, with different mean orientations and degrees of reorientations depending on their positions in the molecule, and may have different orientational order parameters. The more free is the motion, the lower is the orientational order parameter. For a deuterated polymer, the free motion of the side chain deuterons causes line narrowing while more restricted motion of the deuterons at the backbone gives rise to broader components.

If the C-D bond forms part of a methyl group, rotation of that bond about the methyl axis causes the observed splitting for the C-D bond on a chain of carbons d, to collapse by a further factor of $\frac{1}{2}(3\cos^2\theta - 1)$, where θ is 109.5° in methyl group [28]. The spacing of the prominent edges is then $\frac{1}{3}d$ (see Figure 3.2 (b)).

3.5 Moments

The spectral moments of the spectrum are functions of the quadrupole splittings in the case where the asymmetry parameter is zero and the motions are axially symmetric. In principle, they can provide a complete description of the distribution of quadrupole splittings. The zeroth moment $M_0 = \int_0^\infty f(\omega)\ d\omega$, where $f(\omega)$ is the spectrum, represents half of the area under the deuterium NMR spectrum. The weighted mean splitting of the spectrum can be obtained by calculating the first spectral moment over half of the spectrum using [52]

$$M_1 = \frac{\int_0^\infty \omega\ f(\omega)\ d\omega}{\int_0^\infty f(\omega)\ d\omega}. \tag{3.13}$$

For a deuterated polymer, M_1 is proportional to the average over all deuterons on the chain and thus to the average order parameter S_{CD}. The n^{th} moment ($n \geq 1$) is given by [52]

$$M_n = \frac{\int_0^\infty \omega^n\ f(\omega)\ d\omega}{\int_0^\infty f(\omega)\ d\omega}. \tag{3.14}$$

The second moment M_2 is the mean square quadrupole splitting.

3.6 Quadrupole pulse sequence

The rf pulse flips the magnetization through an angle that depends on the time duration for the pulse application. The $\frac{\pi}{2}$ and π flip angles are the most commonly used [50]. The quadrupole echo pulse sequence consists of two $\frac{\pi}{2}$ radio frequency pulses differing in phase by $\frac{\pi}{2}$ and separated by time τ, see Figure 3.3. The quadrupole echo technique [58] must be used because of the "dead time" of the preamplifier. After we apply the very strong rf pulse through the transmitter, the amplifier needs time to recover and amplify the very small signal coming from the same coil as the receiver. We wait for a time τ first, which is much longer than the receiver dead (recovery) time. Then we apply the second pulse and wait for

another τ for the "echo refocusing".

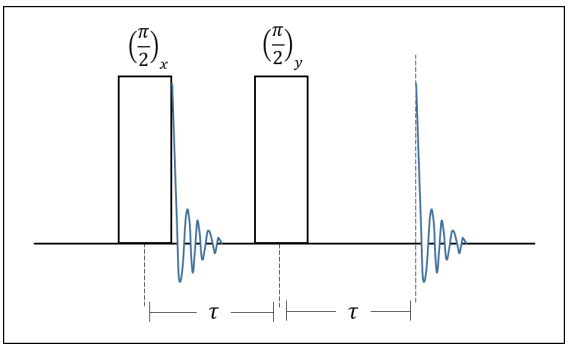

Figure 3.3: Quadrupole echo pulse sequence. In quadrupole echo decay experiment we vary the pulse separation τ.

The first $\frac{\pi}{2}$ pulse generates transverse magnetization by flipping the magnetization from the z axis to the xy plane. Just after the first pulse, spins will evolve under the influence of the quadrupole Hamiltonian. Different spins will accumulate phase differently depending on the average quadrupole interaction experienced by each deuteron [48] and will get out of phase. The second $\frac{\pi}{2}$ pulse is used to refocus the dephasing of the magnetization and form the echo at 2τ after the first pulse. The amplitude of the echo depends on the extent to which the quadrupole interactions for individual spins remain constant over the 2τ time interval.

3.7 Quadrupole echo decay time

Motions that change orientation of the average EFG with characteristic times in the range of the NMR experiment time scale ($\sim 10^{-5}$ s), reduce the amplitude of the quadrupole echo. Different orientations of the motional symmetry axis can give rise to different decay times, and so relax differently. As we increase the pulse separation time τ, the resulting quadrupole echo signal decays exponentially [59]. Motions that alter the quadrupole interaction during 2τ contribute to echo decay. The echo amplitude is the sum over populations with different

decay rates R_i and can be written as

$$S(2\tau) = \sum_i W_i exp(-2\tau R_i), \tag{3.15}$$

where W_i is a weighting factor that is proportional to the fraction of the deuterons having echo decay rate R_i.

The echo decay rate is the weighted average of the superposition of the contributions, R_i, from all motions i that modulate the quadrupole interaction and is defined as

$$\langle R \rangle = \sum_i W_i R_i. \tag{3.16}$$

The sum over i is over all the deuterons but a given C-D bond might be affected by more than one motion so R_i becomes a sum over motions labelled by j.

A given motion can be characterized by a correlation time τ_c and the second moment, ΔM_2, of the distribution of splittings sampled as a result of that motion. The extent to which this motion modulates the quadrupole Hamiltonian is thus characterized by ΔM_2. A motion can be classified as fast or slow based on comparison between τ_c and $(\Delta M_2)^{-\frac{1}{2}}$.

For fast motions like chain rotations and conformational fluctuations $\Delta M_2 \tau_c^2 << 1$ [60], while for slow motions like diffusion $\Delta M_2 \tau_c^2 >> 1$. The contribution to the echo decay rate R_i is proportional to $\Delta M_2 \tau_c$ in fast motion regime. On the other hand $R_i \propto \tau_c^{-1}$ in slow motion regime. Echo decay gives a way to distinguish how contributions to the NMR signal from fast and slow microgel component motions change with temperature and pressure. If a given deuteron is on a C-D bond subject to multiple motions, the echo decay rate for that deuteron is a sum of contributions from those motions.

Quadrupole echo decay is characterized by an averaged decay rate over all the deuterons. The initial decay time, T_{2e} for short τ, is inversely proportional to the average decay rate

$$T_{2e}^{-1} = \langle R \rangle \tag{3.17}$$

In order to measure the echo decay time we collect spectra with varying τ, and record the echo amplitudes $A(\tau)$. The negative inverse of the initial slope of $[\ln(A(\tau)/A(0))$ *vs* $2\tau]$ gives T_{2e}.

Slow motions with long correlation times have small echo decay rates ($R\ \alpha\ 1/\tau_c$) and long echo decay times. On the other hand, fast motions with short correlation times also have small echo decay rates ($R\ \alpha\ \tau_c$) and long echo decay times [48, 55]. Segment reorientation with an intermediate correlation time may give rise to a very short quadrupole echo decay time. Quadrupole echo decay time *versus* reorientational correlation time can thus display a minimum [61].

Chapter 4

Experimental Methods

4.1 Microgel synthesis

One goal of this study is to investigate the effect of the cross-linking density, C_d, on the microgel particle internal structure and properties. The microgel synthesis was carried out in our laboratories in order to enable control of parameters like C_d. Also, because the natural abundance of deuterium is vanishingly low, it is necessary to specifically label a polymer to observe its solid state deuterium NMR spectrum. For this it was necessary to have the option to choose what type of monomer to start with, i.e. deuterated or not deuterated. Poly N-isopropylacrylamide microgels deuterated (mostly) at the backbone and at the side chains (once) were used in this study. The chemical structures of the nipam monomers options that were used for the microgel syntheses in this study are shown in Figure 4.1 (a).

The monomer of d3 nipam has three deuterons at the backbone. Crosslinked poly N-isopropylacrylamide microgel colloid was synthesized by dispersion polymerization using deuterated monomer, N,N'-methylenebisacrylamide (BIS) as a crosslinker, potassium persulfate (KPS) as an initiator, and (SDS) sodium dodecyl sulfate as a surfactant. The crosslinking density C_d, defined here as the crosslinker to monomer ratio, was chosen to be 1.5, 7.5, 13.6, or 19.5 % wt/wt in the polymers that were synthesized for this project. One

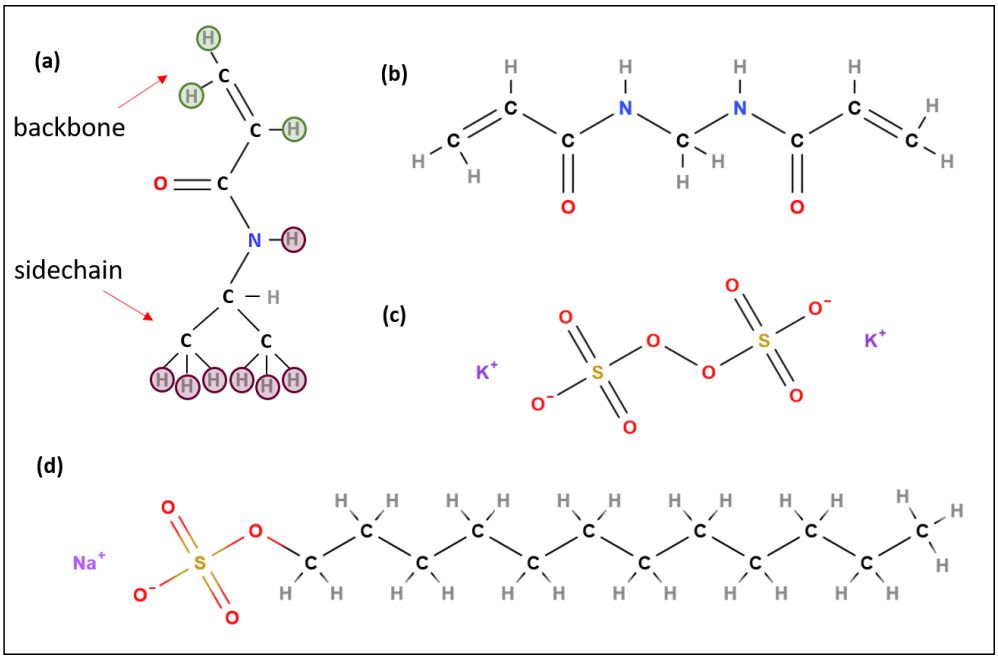

.

Figure 4.1: Structural formulae of: a) nipam monomer, ($C_6H_{11}NO$). The Hydrogen atoms at the backbone (circled with green) or at the side chains (circled with purple) can be replaced by deuterons forming d3 nipam or d7 nipam, respectively. b) N,N'-methylenebisacrylamide (BIS) crosslinker, ($C_7H_{10}N_2O_2$). c) potassium persulfate (KPS) initiator, ($K_2S_2O_8$). d) sodium dodecyl sulfate (SDS) surfactant, ($C_{12}H_{25}NaO_4S$) [62]

can estimate the average number of monomer molecules between two crosslinking molecules in the polymer chain by converting the weight ratio of the crosslink density to the molar ratio. For example, the microgel made at C_d=7.5 % wt/wt corresponds to 5.5 % mol/mol crosslinking density and thus has on average 1 molecule of crosslinker per 18 molecules of monomer. Also, non-deuterated monomers were used for making non-deuterated (h nipam) microgels, with the same C_d as the deuterated microgels, for rheology experiments. Microgel synthesis was done by using a recipe provided by Dr. Priti Mohanty (research collaborator, KIIT University, India).

The synthesis method was updated from one originally described by Senff and Richtering [4]. Some trials were done to learn about how to scale different batch sizes, partly because of the limited availability of deuterated monomer. After that, specific crosslink density batches

were synthesized using non-deuterated and deuterated monomers. Rheology experiments were done by using the h nipam and ^{2}H NMR experiments were done by using d3 nipam. We compare results from both methods at different crosslink densities. DLS was used to confirm consistency of swelling behaviour between the two syntheses for each crosslink density.

In order to practice the recipe provided, a synthesis with a given C_d value was first carried out using a non-deuterated monomer. After doing the DLS characterization for the synthesized h nipam polymer, the corresponding synthesis using the deuterated monomer was carried out. Additional trial syntheses were done at the beginning to learn how to scale batch size. In these trials, a given non-deuterated synthesis was done twice on successively smaller scales after which the corresponding deuterated synthesis was completed.

As a result, eight polymers were synthesized and then used in this work. Table 4.1 shows all the eight polymer syntheses parameters.

Table 4.1: The parameters for the eight syntheses used in this work: four non-deuterated, made from h nipam monomer, and four deuterated, made from d3 nipam monomer. The last column shows the syntheses crosslinker to monomer weight ratios, that is defined as the crosslink density "C_d", for the syntheses.

Synthesis	type	nipam monomer(g)	BIS (g)	KPS (g)	SDS (g)	water amount (ml)	C_d (wt%)
SSS02	h	0.9965	0.0751	0.0232	0.0363	100	7.5
SSS03	d3	0.997	0.0752	0.0235	0.035	100	7.5
SSS06	h	1.8867	0.2573	0.047	0.06	100	13.6
SSS08	d3	0.9434	0.1287	0.0235	0.035	50	13.6
SSS10	h	1.8867	0.3679	0.047	0.06	100	19.5
SSS12	d3	0.9311	0.1816	0.0233	0.0345	50	19.5
SSS13	h	1.8867	0.0283	0.047	0.06	100	1.5
SSS14	d3	0.9434	0.0142	0.0233	0.035	50	1.5

4.1.1 Synthesis strategy

Backbone deuterated monomer was obtained from Polymer Source Inc., Dorval, QC, Canada. Non-deuterated monomer, crosslinker, initiator, and surfactant were obtained from Sigma Aldrich Inc., Oakville, ON, Canada. The polymers of d3 nipam and h nipam were synthesized

locally in our laboratories.

As an example of the procedure used, a brief description of the SSS03 synthesis follows. First, 0.997 g of the d3 nipam monomer and 0.0752 g of crosslinker (BIS) were dissolved in 80 ml of distilled water. Separately, 0.0235 g of (SDS) surfactant was dissolved in 10 ml water. The uncertainty in measured masses was $\pm$ 0.0005 g. The mixtures were transferred into a 250 ml round-bottom flask. The mixtures were heated at 70°C and degassed under a gentle nitrogen stream with a stirring speed of 270 rpm for 45 min. Finally, the initiator, KPS (0.0363 g dissolved in 10 gm of water) was added slowly to initiate the polymerization. The reaction mixture was kept at 70°C under nitrogen gas gentle flow for 6 hours to complete the reaction with a heater stirring speed of 270 rpm. The reaction was stopped after 6 hours by switching off the heater. The stirring was maintained while the sample cooled back to room temperature, and then continued overnight to keep the particles from being trapped in the collapsed state after the high temperature synthesis. The intent of this stirring was to ensure that particles remained separate and in suspension and were thus able to return to the swollen state as the sample was cooled back to room temperature following polymerization. This synthesis procedure was originally introduced by Senff and Richtering [4]. A diagram for the synthesis apparatus and set up is shown in Figure 4.2.

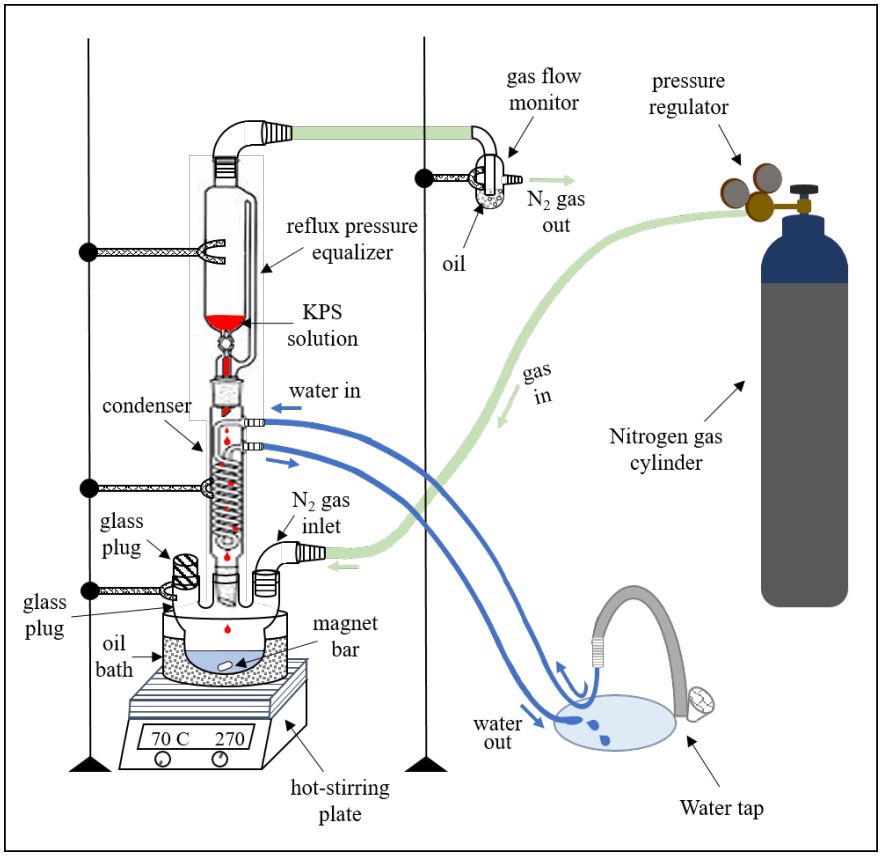

Figure 4.2: Diagram for synthesis apparatus and set up.

After synthesis, the microgel suspension was purified in order to remove un-reacted monomers and ionic impurities. This purification was carried out in steps. First the product of the synthesis was centrifuged using an ultracentrifuge at 40,000 - 50,000 rpm for 45 - 60 minutes to sediment the microgel particles. This centrifugation was carried out at 35°C to ensure that particles were in the higher density collapsed phase. After centrifugation, the top part of the suspension (the supernatant) was taken out and once again the bottom part of the microgel suspension was diluted with deionized water (conductivity less than 4 μS/cm) and redispersed by vortex and ultrasonication cycles. With the ultrasonic bath set at 30°C, the diluted suspension was ultrasonicated for about 2 hours in total with additional vortexing for 1-2 minute every 15 min. Following redispersion, the sample was centrifuged again. This part of the procedure was carried out 6 times in order to remove unreacted monomers. After this, the purified microgel suspensions were dialyzed against deionized water for one week.

Once the microgel suspension was purified, the swelling transition (i.e. temperature dependence of hydrodynamic radius) was characterized using dynamic light scattering at dilute concentration. Finally, the microgel suspensions were freeze dried and kept for future use. Centrifuge and freeze drying were carried out in the Biochemistry Department, at Memorial University, in the laboratory of Dr. Valerie Booth with the assistance of Donna Jackman, and Craig Skinner.

4.2 Dynamic light scattering

DLS results were obtained for dilute suspensions of the synthesized polymers in deionized water at a 0.04 wt% concentration. This concentration corresponds to a volume fraction that is much less than 1 as noted in the discussion of DLS theory in Chapter 2. Measurements were conducted over a temperature range of 5 to 45°C with 2-3 °C steps. Three measurements were recorded for every temperature to reduce the possible errors [24]. The DLS instrument, Zetasizer Nano ZS (Malvern Instruments, Montreal, QC, Canada) contains a He-Ne laser operating at a wavelength of 633 nm (see Figure 4.3) in a backscattering geometry setup with light detection at an angle of 173 °.

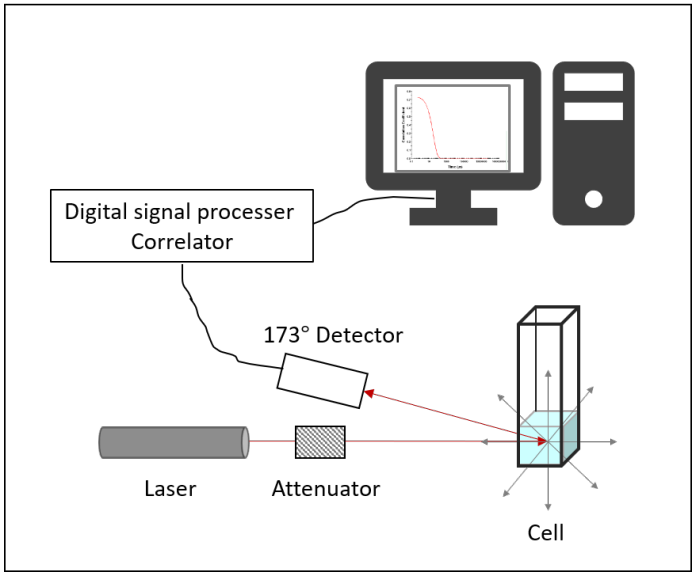

Figure 4.3: Schematic diagram of Zetasizer Nano series for dynamic light scattering measurements.

The hydrodynamic radius R_H of the microgel particle as a function of temperature was obtained from the DLS measurements. The swelling factor (S), defined as the ratio of the particle's volume in the swollen phase to that in the collapsed phase, i.e. the cubic ratio of the hydrodynamic radii in both phases, was then obtained for each C_d using

$$S = \left(\frac{R_H(5°\mathrm{C})}{R_H(45°\mathrm{C})} \right)^3 . \tag{4.1a}$$

In order to compare the collapse transition for different C_d on a scale that goes from 0 to 1 we calculated a normalized particle volume,

$$V_{norm}(T) = \left[\frac{1 - \left(\frac{R_H(T)}{R_H(45°\mathrm{C})} \right)^3}{1 - S} \right] , \tag{4.1b}$$

as a function of temperature for each C_d in order to find the transition temperature for each microgel synthesis. For the purpose of comparison, the transition temperature was identified as the temperature at which the particle's volume is reduced by 80% of its value at 5°C. This can be found at V_{norm}=20%, thus the transition temperature was determined as being $T\Big|_{V_{norm}=0.2}$.

4.3 Rheological measurements

Rheology experiments were carried out to investigate the elastic properties in our protonated (non-deuterated) synthesized microgels. Rheological characterizations for our synthesized microgels as a function of concentration, crosslinking density, volume fraction, or temperature would allow us to compare our studies on microgels with what has previously been reported in the literature. Measurements were carried out with an Physica MCR 301 (Anton Paar Inc., Montreal, QC, Canada) strain controlled rheometer, with the cone-plate configuration used to obtain the flow curves, i.e. the σ *versus* $\dot{\gamma}$ relations. A solvent shield was used in order to minimize solvent evaporation. From the flow curve the microgels viscosity behavior

was determined [13]. Mechanical properties (the storage and loss moduli) of these microgels were also characterized by doing oscillatory shear measurements using this rheometer. The cone-plate system used (CP50-1) has a 50 mm diameter and 1° angle.

4.3.1 Sample preparation for rheology measurements

Samples were prepared from the four differently crosslinked protonated microgel powders and distilled water. After adding water to powder, the mixture was stirred for 1-2 minutes then placed in an ultrasonic bath for about 2 hours. In order to estimate volume fractions, it was necessary to note that differently crosslinked microgels have different swelling ratios across the collapsed transition. For each crosslink density synthesized, suspensions were prepared at four different concentrations ranging over 1 - 12%. This resulted in a wide range of volume fractions being studied for each crosslink density prepared. Following the preparation described above, samples of ~ 600 μl size were loaded into the cone-plate rheometer. This was done after testing a water sample for rheometer calibration.

4.3.2 Rotational and oscillatory shear measurements

Using Rheoplus software, that was supplied by the rheometer manufacturer, the rheology experiment setting was controlled. Two tests were conducted: rotational steady shear to obtain "Shear stress *versus* strain rate" flow curves and oscillatory shear to obtain elastic and loss moduli. A room temperature flow curve was measured once in the beginning. Then temperature was decreased to 5°C and a flow curve measurement was taken. After that temperature was raised by 2°C - 3°C steps and measurements were taken, similar to the DLS measurements, to facilitate the calibration of volume fraction as a function of concentration. The room temperature flow curve was reproduced with increasing temperature and again was repeated after each measurement at higher temperatures. Measurements were terminated when the room temperature measurement gave inconsistent results, as an indication of sample evaporation.

In the flow curve test, the microgel suspension response to a linearly ramped shear rate $\dot{\gamma}$ was measured. Data were collected with a logarithmic $\dot{\gamma}$ profile at 10 points per decade over 0.01- 9000 s^{-1} at low temperatures and over smaller ranges at higher temperatures. This was done to eliminate the disturbance of the laminar flow at both high temperature and high shear rate. Collection time per point was varied from 10 seconds for minimum shear rates to 1 second for maximum shear rates.

Oscillatory shear measurements were conducted to measure the storage and loss moduli as a function of the shear strain oscillation frequency, for each sample in both swollen and collapsed phases. These measurements were taken in between the flow curve experiments, at only 2-3 temperatures for each sample. The amplitude of the shear strain was set at 2.5 % and the frequency was varied over the range 0.05-200 s^{-1}.

4.3.3 The power law region

As mentioned earlier in sections 2.3.1 and 2.3.2, Microgels are pseudo-plastic fluids that exhibit a combination of Newtonian and shear-thinning flow behavior. The Newtonian behavior is characterized by a linear flow curve (σ-$\dot{\gamma}$ relation) with a constant viscosity (slope) as the shear rate is increased while the shear-thinning fluid is characterized by a viscosity that is decreasing as the shear rate is increased. The measured viscosity as a function of the shear rate is actually the shear stress divided by the shear rate, that is given by $\eta(\dot{\gamma}) = \sigma/\dot{\gamma}$. One can divide equation (2.7) in Section 2.3.1 by $\dot{\gamma}$, and express the viscosity-shear-rate relation by the power law model as

$$\eta = K\dot{\gamma}^{-m},$$

where $(n-1)$ in equation (2.7) is renamed here to be $-m$. The parameter m satisfies the condition $|m| < 1$ for a shear-thinning fluid while $m = 0$ for a Newtonian fluid. Thus the consistency coefficient K here has the unit of (Pa·s^{1-m}). Taking the logarithm of the last

equation and differentiating with respect to $\log \dot{\gamma}$ one gets

$$\frac{d(\log \eta)}{d(\log \dot{\gamma})} = -m. \tag{4.2}$$

The slope of the $\log(\eta)$ *versus* $\log(\dot{\gamma})$ plot will thus give the negative of the exponent value m. For the Cross model, however, it is a bit more complicated. Using $\frac{d(\log \eta)}{d(\log \dot{\gamma})} = \frac{\dot{\gamma}}{\eta}\frac{d\eta}{d\dot{\gamma}}$, we find that

$$\frac{d(\log \eta)}{d(\log \dot{\gamma})} = \left[\frac{(\eta_0 - \eta_\infty)(\dot{\gamma}\tau)^m}{\left(\eta_\infty + \frac{\eta_0 - \eta_\infty}{1 + (\dot{\gamma}\tau)^m}\right)(1 + (\dot{\gamma}\tau)^m)^2}\right](-m),$$

where the term in the square bracket is equal to unity when $\eta_0 >> \eta_\infty(\dot{\gamma}\tau)^m$ and $\dot{\gamma}\tau >> 1$. When this condition is not satisfied the term in the square bracket is less than 1, and the measured value of $\frac{-d(\log \eta)}{d(\log \dot{\gamma})}$, which we denote as $(m_{apparent})$, will be less than the m. Thus, $m_{apparent}$ will be a lower bound for the Cross exponent m.

This measure of m was possible even in cases (at low temperatures) when it was not possible to observe a low-shear plateau, so that a full fit to the Cross equation was not possible (see Section 4.3.4, below). It turned out that plotting $m_{apparent}$ as a function of T was a reasonable way to identify microgel phase behavior.

For most polymers, the viscosity-shear rate relationship obeys a power law relation in the intermediate $\dot{\gamma}$ regime. The investigation of the exponent m value for the $\eta - \dot{\gamma}$ curve in the intermediate region, as suggested by Cross [39], is a measure of the extent to which is the material is shear-thinning. This region in the measured viscosity-shear rate curves was tested to find the exponent value and the shear-thinning strength for the microgels studied. This is described in Section 5.2.1.1 in the results chapter.

4.3.4 Determination of zero-shear viscosity

The measured shear viscosity η *versus* shear rate $\dot{\gamma}$ results from the steady shear experiments were used to find the zero shear viscosity η_0. The Cross model can be used to find η_0 for the case where there is a well defined low-shear plateau region at low $\dot{\gamma}$. This plateau was found in measurements where the microgel behaved more like a gel. In other cases, i.e. at higher temperatures or lower particle concentrations, where the microgel was in the colloidal regime, it was more appropriate to use the stress-shear rate relation, namely the "flow curve", to determine the zero shear viscosity by doing a linear fit for the low $\dot{\gamma}$ part of the curve. At the lowest temperatures, η_0 was not obtainable as the plateau shifted to shear rates lower than measurable by our system.

4.3.5 Dependence of relative viscosity on particle volume fraction and softness

The microgel particle in a water suspension is presumed to consist of the nipam polymer and water, as shown in Figure 4.4.

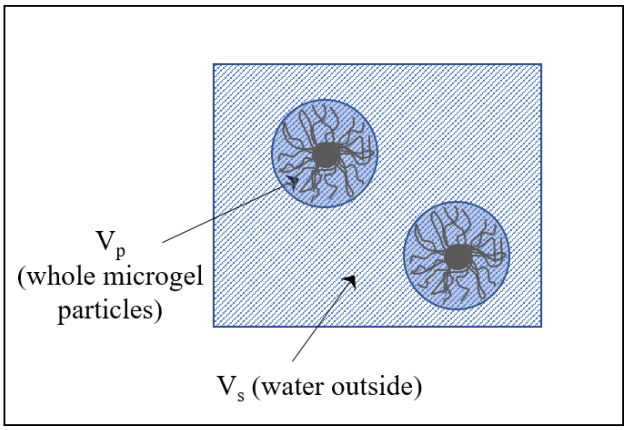

Figure 4.4: The model of a suspension of microgel particles.

The particle volume fraction can be defined as

$$\phi = \frac{V_p}{V_p + V_s} = \frac{1}{1 + \frac{V_s}{V_p}}, \tag{4.3}$$

where V_p is the total microgel particle volume, and V_s is the volume of the solvent (the water outside the particle). The total volume of water in the system (inside and outside the particle) is independent of temperature and given by

$$V_w = V_s + fV_p, \tag{4.4}$$

where f, the fraction of the particle volume accounted for by water, is temperature dependent. From this relation, one can say that the volume of the particle-bound water is $V_{waterinside} = fV_p$. The nipam volume per particle in the system is presumed to be independent of temperature, and can be defined as the factor k so that

$$V_{nipam} = (1 - f\ )V_p\ =\ Nk \tag{4.5}$$

where N is the total number of particles. This last identification is true even with particle overlap, because V_{nipam} refers to polymer volume. In equation (4.5), the particle volume and the particle-bound water fraction both depend on temperature. Dividing the total water volume in the system by the nipam volume in the system gives

$$\frac{V_w}{V_{nipam}} = \frac{\frac{V_s}{V_p} + f}{1 - f}.$$

The ratio of solvent volume to particle volume can the be written as

$$\frac{V_s}{V_p} = \left[\frac{V_w}{V_{nipam}}(1-f)\right] - f. \tag{4.6}$$

The concentration by weight of the sample, C, is a known quantity, measured while preparing the sample, and is defined by

$$C = \frac{m_{nipam}}{m_{nipam} + m_w},$$

where m_{nipam} and m_w are the experimentally measured masses of nipam powder and water. The densities of nipam and water are known and they have the values $\rho_{nipam} = 1.1$ g/cm^3 and $\rho_w = 1$ g/cm^3. By converting masses to density-volume products in the previous equation and rearranging, the $\frac{V_w}{V_{nipam}}$ ratio is found to be

$$\frac{V_w}{V_{nipam}} = \left(\frac{1}{C} - 1\right)\frac{\rho_{nipam}}{\rho_w}. \tag{4.7}$$

The particle volume fraction now can be expressed in terms of f, C, ρ_{nipam}, and ρ_w by substituting equation (4.7) into (4.6), and then into (4.3). The equation for the particle volume fraction becomes

$$\phi = \frac{1}{(1-f)\left[1 + (\frac{1}{C} - 1)\frac{\rho_{nipam}}{\rho_w}\right]}.$$

The $(1-f)$ term can be replaced by the ratio of $\frac{k}{v_p}$, using equation (4.5), and defining a single particle volume

$$v_p = \frac{V_p}{N}. \tag{4.8}$$

This single-particle volume only equals $\frac{4}{3}\pi R_H^3$ (obtained from DLS) in the absence of overlap. Using these definitions, the microgel particle volume fraction can be expressed as

$$\phi = \frac{v_p}{k\left[1 + (\frac{1}{C} - 1)\frac{\rho_{nipam}}{\rho_w}\right]}. \tag{4.9}$$

The Krieger-Dougherty formula, equation (2.18), in Chapter 2, can be re-arranged to express the volume fraction as a function of the relative viscosity, so that we also have

$$\phi = \phi_{max}[1 - \eta_{rel}^{1/(-2.5\phi_{max})}]. \tag{4.10}$$

Assuming that the viscosity of the microgel suspension behaves like a hard sphere suspension in the collapsed phase, the relative viscosity in this phase can be fit to the Krieger-Dougherty formula, [equation(2.18)], to obtain an estimate of the volume fraction in this temperature range. By equating the two equations, (4.9) and (4.10), the k factor, which represents the total nipam volume per particle can then be estimated as

$$k = \frac{v_p}{\phi_{max}[1 - \eta_{rel}^{1/(-2.5\phi_{max})}](1 + (\frac{1}{C} - 1)\frac{\rho_{nipam}}{\rho_w})}. \tag{4.11}$$

4.4 ^{2}H NMR spectroscopy

^{2}H NMR spectra were collected using two different locally assembled spectrometers. Ambient pressure spectra were acquired at different temperatures using a high field, 9.4 T, spectrometer that operates at the deuteron Larmor frequency 61 MHz. Variable pressure spectra were acquired using a lower field, 3.5 T, spectrometer that operates at the deuteron Larmor frequency 23 MHz, and has a variable-pressure probe. Samples for NMR experiments were made from the deuterated microgels with different crosslink densities and deuterium-depleted water. They were prepared by mechanical mixing until the resulting suspensions were homogeneous. Most of the deuterated microgel suspensions for NMR experiments were made at a concentration of 20 wt% with respect to water.

4.4.1 ^{2}H NMR spectrometer setup

The two solid state ^{2}H NMR spectrometers used for this work were used previously [63,64]. They utilize two superconducting magnets with different field strengths and accordingly have different ^{2}H resonance, frequencies. Both spectrometers operate as heterodyne systems [65] with phase shifting being done at 10 MHz. A brief description of the general spectrometer operation follows. A block diagram of the NMR spectrometer is shown in Figure 4.5.

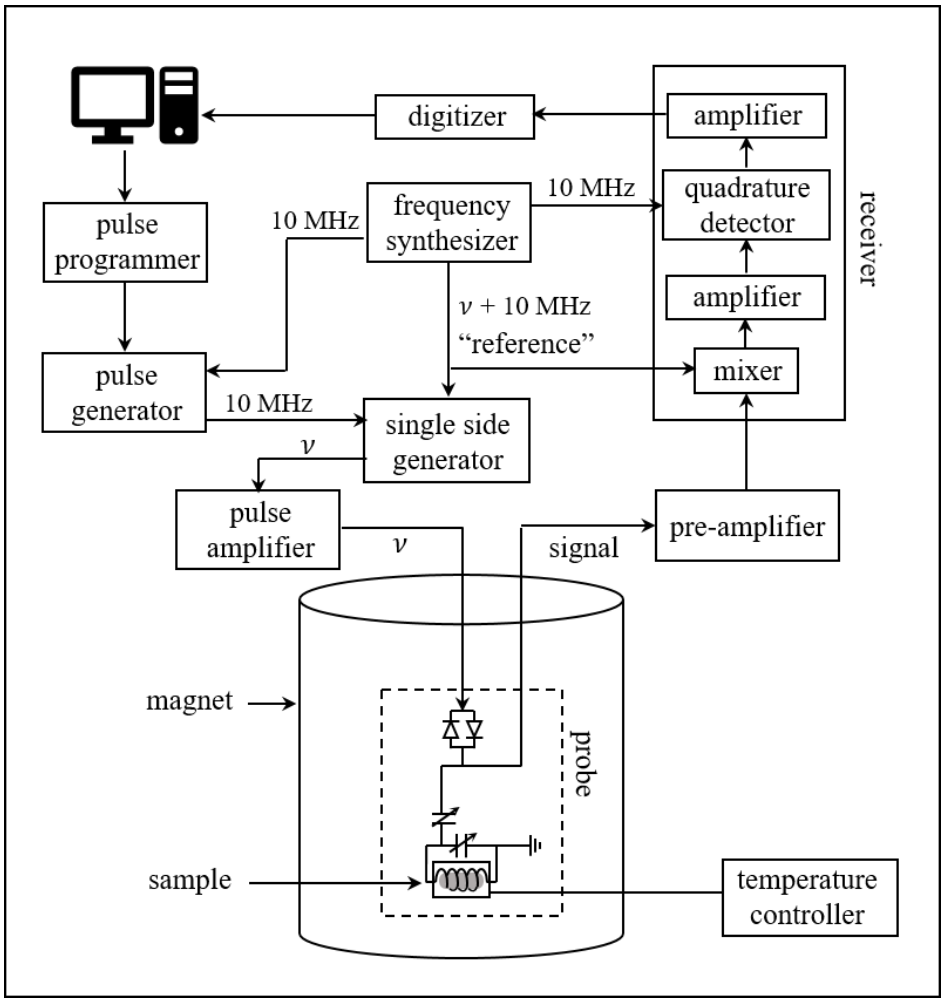

Figure 4.5: Block diagram of NMR spectrometer.

The main NMR spectrometer components are a frequency synthesizer, a single-side-band generator, a pulse amplifier, a probe, a pre-amplifier, a receiver, and a computer for pulse parameter control, data collection, and analysis. The frequency synthesizer provides two

signals, one at 10 MHz and the other at ν+10 MHz, where ν is the operating frequency of the spectrometer. The 10 MHz signal is sent to a quadrature detector in the receiver and to a phase-shifting pulse generator. The ν+10 MHz signal is sent to a mixer in the receiver and to mixers in the single-side-band generator [57].

The 10 MHz signal in the pulse generator is converted into pulses with four set phases of 0°, 90°, 180° and 270°. The pulse length and separation are controlled by a pulse programmer. The resulting 10 MHz pulses are fed into the single-side-band generator, where they are mixed with the ν+10 MHz signal to produce pulses at frequency ν, the ^{2}H magnetic resonance frequency. This signal is then amplified by the pulse amplifier and transmitted to the sample through the resonant probe circuit. The probe circuit contains an inductor (sample rf coil) and two variable capacitors which are used to match the frequency of the probe circuit to the deuteron resonance frequency ν and to match the impedance to 50 Ω. The sample produces a weak signal, at this frequency, that is detected by the same rf coil and amplified by the pre-amplifier. The NMR signal is then fed to the receiver and mixed with the ν+10 MHz reference from the frequency synthesizer resulting in a 10 MHz signal modulated by the NMR signal (FID). This signal is amplified and sent to the quadrature detector which splits the 10 MHz signal coming from the frequency synthesizer to 0° and 90° phases, and produces the real and imaginary parts of the NMR signal by comparing it to the split phases. After that, the NMR signal is amplified, digitized, and sent to the computer for analysis. The quadrature detector also uses a 10 MHz reference to mix the signal down to the modulation frequencies left after the removal of the Larmor frequency.

4.4.2 Ambient pressure high field spectrometer

The ambient-pressure high field spectrometer consists of a superconducting magnet (Magnex Scientific Inc., Abingdon, UK) at a magnetic field of 9.4 T which corresponds to a 61 MHz ^{2}H resonance frequency. For the experiments described here, a small NMR tube of $\sim$ 400 μl size containing the microgel sample, $\sim$ 200 μl size, was positioned in a small coil mounted on

the probe. Free induction decays (FID) were collected using a digitizer with fixed dwell time (dt) of 1 μs and a length (size) of 8192 points. Spectra were derived from FIDs obtained by averaging 1000 - 120,000 transients accumulated using a quadrupole echo sequence [48] with two $\frac{\pi}{2}$ pulses of 3-4 μs pulse length and 30 μs pulse separation. Oversampling, contracting or both [52, 57], by a factor of 2 or 4 was used to give effective dwell times of 2 or 4 μs. All NMR spectra from this magnet were acquired at 20 - 60 °C and ambient pressure.

4.4.3 Variable-pressure low field spectrometer

All the variable pressure experiments spectra were collected using a 3.5 T superconducting magnet (Nicolet Cryogenics, Martinez, CA, US) which corresponds to a 23 MHz ^{2}H resonance frequency, in conjunction with a locally constructed solid state spectrometer, and a locally constructed variable-pressure probe with a beryllium copper cell [64]. Microgel samples of $\sim$ 350 μl size were enclosed in soft capsules formed from polyethylene food wrap sealer using a dental floss tie. Microgel-filled capsules were placed in a coil mounted in a cylindrical Teflon holder that was then inserted into the variable-pressure probe. The probe cell could be pressurized with hydraulic oil using a hand pump. Variable pressure spectra from this magnet were acquired at 20 - 55 °C and pressures of 0.1 (ambient pressure), 30, 60, 90 MPa. The digitizer used in this spectrometer (Nalorac 2090A digital oscilloscope), has a variable dwell time. FIDs were collected with a dt of 2 μs and 2048 points size.

4.4.4 ^{2}H NMR data analysis

In our NMR experiments, the measured time-domain signal, known as the FID, was digitized into a set of data points evenly spaced in time [52]. After some processing of the digital signal to insure that the first point of the FID is at the echo peak [52] and that points are appropriately spaced to give the desired spectral width, it can be Fourier Transformed to generate the frequency-domain spectrum. A typical swollen phase microgel spectrum was found to have a characteristic narrow peak at the center with a width of a few kilohertz in

frequency. A narrow peak in the spectrum corresponds to a slowly decaying FID signal. In order to obtain the narrow peak without too much distortion, each FID was sampled for at least 8 ms following the echo peak to avoid cutting off the FID acquisition before the signal from the narrow peak had decayed away. The digitization process involves sampling the signal at constant intervals short enough to ensure a good approximation to the smoothly varying signal for the largest splittings anticipated.

Oversampling and contraction

The quadrupole echo technique treats the top of the echo as the beginning of the free precession signal and requires that it occurs at the start of the time domain signal. If the first digitized point is not exactly at the top of the echo there will be a distortion of the spectrum obtained after it has been Fourier transformed [52]. Analysis of a distorted spectrum will lead to systematic errors in quantities such as spectral moments.

Depending on the digitizer being used, the transients are acquired using the digitizer dwell time (dt) μs and a points size (sz). Commands in the spectrometer data acquisition and analysis program used for this work allow the point-time representation in the FID to be adjusted so as to place a point at the top of the echo before Fourier transforming it. The commands "contract" (cn) and "oversampling" (os) were used to collapse N interleaved sets of points into a sequence of single points separated by a dwell time of N μs (for a 1 μ digitizer dwell time). After adding these processed parts together and cutting off the points before the top of echo, the routine returns an FID with a dwell time of N μs that can then be Fourier transformed [66]. Both commands do the same thing except that in "cn", each of the "sub-FIDS" is shifted by a fraction of a dwell time in order to place a point onto the top of the echo before adding the "sub-FIDS" together and the points to the left of the peak are removed. The "os" command does the same thing without these last two steps. The Fourier transformation is done and the spectra are saved with a 4096 points size files.

In cases where the spectrum is very narrow and the echo peak is very flat, the FID can

have a local maximum earlier than the actual echo peak, and "cn" will return large Δt values. This means that contraction failed to find the right maximum. In this case, it was necessary to remove a number of points at the beginning so that the first pronounced peak in the FID was the echo maximum. When properly applied both methods, either the oversampling or the contraction, should give the same spectral shape.

Chapter 5

Results: Microgel Characterization by DLS and Rheology

5.1 DLS Results

Dynamic light scattering was used to obtain the intensity of the scattered light, measured as a function of temperature for all the syntheses used for this project. Above 35°C, the scattered light intensity increases as a result of the increase in the refractive index of the polynipam molecules as they undergo a transition from random coil polymer to condensed globule structure [1]. From the measured fluctuations in the scattered intensity as a function of time, the diffusion coefficient D of particles in the dilute suspensions was obtained at each temperature and converted to the hydrodynamic radius R_H of the particles by using the Stokes-Einstein relation (see Section 2.2). The temperature dependence of R_H, for both the non-deuterated (h) and deuterated (d3) synthesized microgels each with four different crosslink densities (C_d=1.5 wt%, 7.5 wt%, 13.6 wt%, 19.5 wt%), are presented in the following Section.

5.1.1 Temperature dependence of hydrodynamic radius and the crosslink density effect on the swelling factor

Figure 5.1 shows the particle's hydrodynamic radius R_H as a function of temperature for both the h nipam (a), and the d3 nipam (b) polymers, for all crosslink densities C_d. The particle's hydrodynamic radius decreases as temperature increases. For all curves the reduction in the particle's volume, presumably the reduction in R_H, occurred roughly in the temperature range from 32°C to 38°C. The inset figures show the ratio of the particle's volume at any temperature T to its volume at T=45°C, that is the swelling factor as a function of temperature $S(T)$, see Section 4.2. As can be seen clearly in the inset figures, the biggest change in the microgel particle volume happens at the lowest crosslink density, C_d=1.5 wt%, in both microgel types. This is reasonable because the higher the crosslink density the less the capacity of the particle to either swell or collapse. For a quantitative measure of the crosslink density effect on the swelling capacity in the studied microgels, the swelling factor defined as $[R_H(\text{at } 5°\text{C})/R_H(\text{at } 45°\text{C})]^3$ was calculated for all the syntheses and reported in Table 5.1.

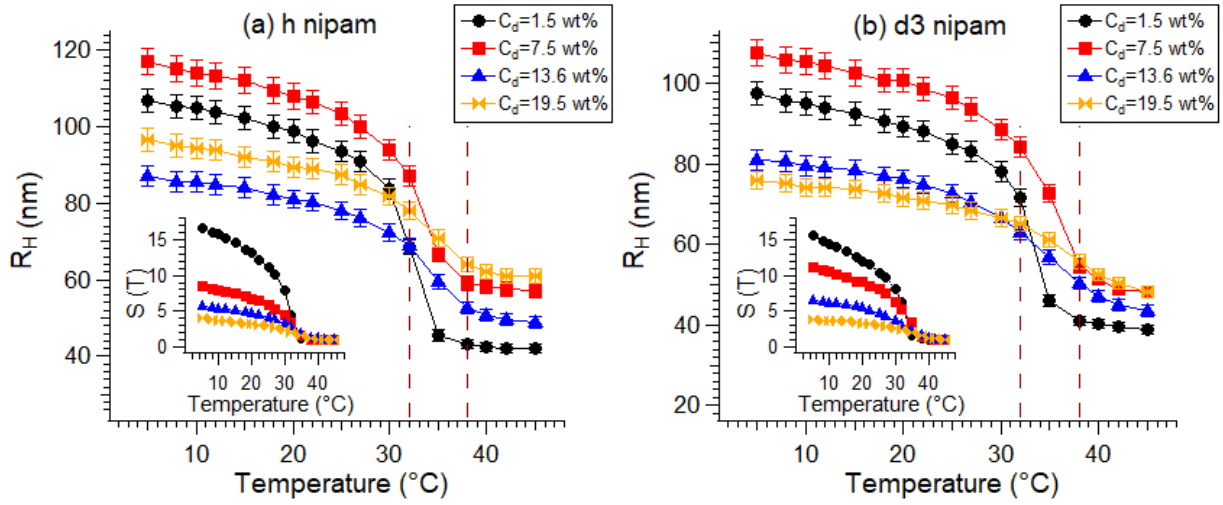

Figure 5.1: The hydrodynamic radius R_H as a function of temperature for both (a) the h nipam and (b) the d3 nipam syntheses obtained from DLS measurements. The insets show the swelling factor as a function of temperature for both microgel types.

The normalized particle's volume as a function of temperature with respect to the particle's volume at T=45°C, V_{norm}, (see Section 4.2) was calculated for each microgel syntheses using equation (4.1b) in order to obtain the transition temperature. Figure 5.2 shows the temperature dependence of V_{norm} for both the h nipam (a), and the d3 nipam (b) polymers, for all crosslink densities C_d.

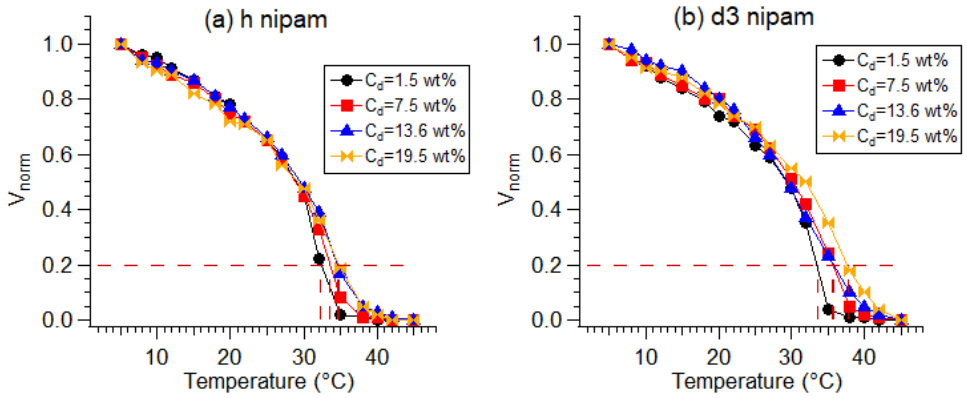

Figure 5.2: V_{norm} as a function of temperature for both (a) the h nipam and (b) the d3 nipam syntheses obtained from DLS measurements. The dashed horizontal line at V_{norm}=0.2 was used to find the transition temperature.

The V_{norm} *versus* T curves spread out over the V_{norm} range of 0 - 0.4 for different C_d. For the purpose of comparison, the temperatures corresponding to the midpoint of this range, V_{norm} = 0.2, were identified as the transition temperatures corresponding to each synthesis. The transition temperatures for each synthesis were obtained as being $T\Big|_{V_{norm}=0.2}$ (see Section 4.2). That was done by reading the intersection points of the horizontal line at V_{norm} (45°C)=0.2 with the curves. The obtained transition temperatures for both the h nipam and d3 nipam syntheses are also listed in Table 5.1 below along with the swelling factors. As shown in the table, the transition temperature for all the syntheses was roughly around 35°C and is weakly dependent on the crosslink density C_d.

The main finding here is that the biggest change in the microgel particle volume happens at the lowest crosslink density, C_d=1.5 wt%, the crosslink density for which the swelling factor S is the largest for both microgel types.

Table 5.1: The swelling factors S , $(R_5/R_{45})^3$, and the transition temperatures, $T\Big|_{V_{norm}=0.2}$, as function of C_d for both non-deuterated (h) and deuterated (d3) microgels. There is a systematic variability of 0.5°C in the reported transition temperature values upon varying the threshold.

	h nipam syntheses		d3 nipam syntheses	
C_d (wt%)	S	T (°C)	S	T (°C)
1.5	17 (1)	32.3 (1)	16 (1)	33.5 (1)
7.5	8.5 (8)	33.6 (1)	11 (1)	35.6 (1)
13.6	5.7 (5)	34.6 (1)	6.4 (6)	35.7 (1)
19.5	4.0 (4)	34.8 (1)	3.9 (4)	37.7 (1)

5.2 Experimental results of rheology

5.2.1 Steady shear flow measurements

Flow curve measurements as a function of temperature were obtained for four microgel crosslink densities and different sample concentrations. These experiments were conducted over a range of temperatures. Temperature was increased and data were collected before the samples started experiencing evaporation and drying. The check for evaporation was done by repeating measurements at room temperature at the beginning of an experiment and then on the way back up from 5°C. Whenever the the room temperature measurement gave a different result from the measurement at the beginning, the data acquisition was terminated.

5.2.1.1 The power law exponent "$m_{apparent}$"

Figure 5.3 shows an example of the raw η-$\dot{\gamma}$ data measured at all temperatures, for the microgel sample of C_d=13.6 BIS/mon wt% and at concentration C=8 wt%. These are plotted on a logarithmic scale. Three regions, low $\dot{\gamma}$ plateau η_0, the high $\dot{\gamma}$ plateau η_∞, and the power law shear-thinning region (see Section 2.3.2) can be seen on curves for temperatures higher than 20°C. At low temperatures, the low-shear-rate viscosity plateau was not detected. It can

be seen that the steepness of the curves in the intermediate region decreases with increasing temperature. On a logarithmic scale, the maximum value of $\frac{-d(\log \eta)}{d(\log \dot{\gamma})}$ represents a lower bound of the exponent value m of the power law (see equation (4.2)). This was identified as $m_{apparent}$.

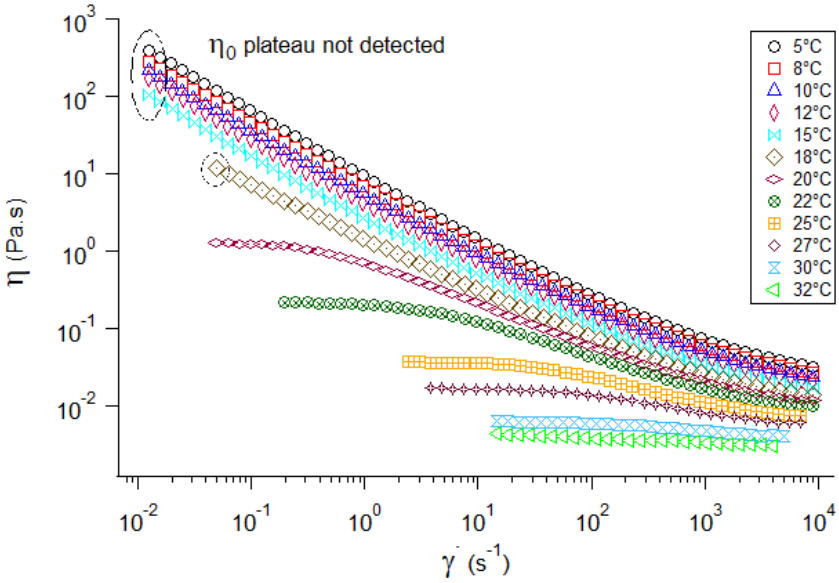

Figure 5.3: The viscosity *versus* shear rate data measurements at all temperatures for the microgel sample of C_d=13.6 wt% and C=8 wt%.

For all of the measurements, the log (η) *vs* log ($\dot{\gamma}$) relations were used to determine the maximum value of the slope, $\frac{d(\log \eta)}{d(\log \dot{\gamma})}$. This was done by finding the slope of successive windows of data points from the starting point of the curve to the last point. The procedure was repeated four times for each individual curve by varying the window width (number of data points) as 5, 10, 15, 20 points. Figure 5.4 shows an example of the slope test results, at window width of 10 points, at all temperatures measured for the microgel sample of C_d=13.6 wt% and C=8 wt%. The maximum slope and the uncertainty in the maximum slope were determined from the average value of the maximum slopes obtained from the four tests (with the different four window widths) and from the difference between the highest and lowest values, respectively. This procedure was performed by a macro written on the Igor Pro platform.

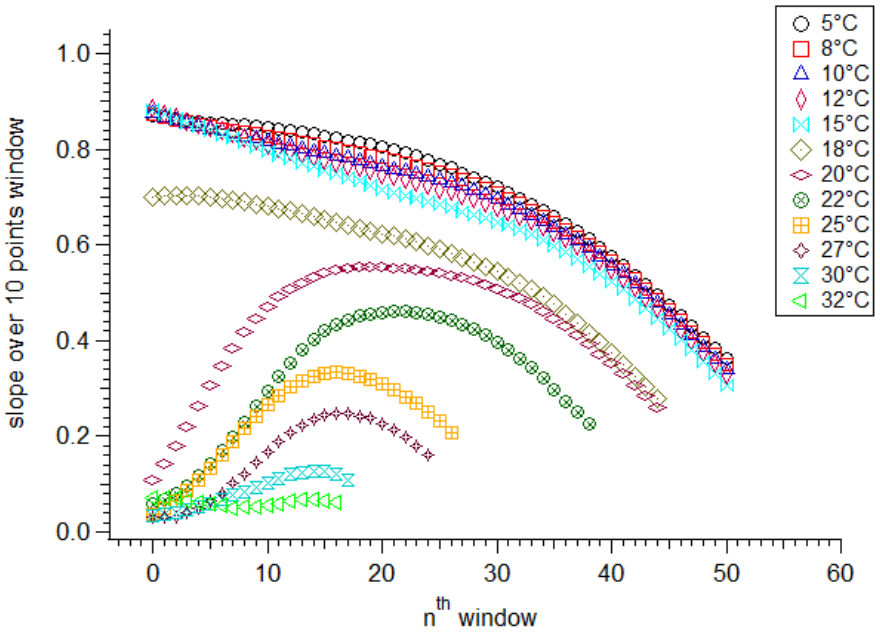

Figure 5.4: The slope test results with the 10 points window width, for all temperatures. This is done for the microgel sample of C_d=13.6 wt% and C=8 wt% steady flow data.

As shown in Figure 5.4, the slope decreases as the window is moved to the right, i.e. higher $\dot{\gamma}$, at low temperatures. At higher temperatures, where the low-shear-plateau was detected, the slope reaches a maximum and then decreases again. The maximum slope value was thus at the lowest measured shear rate for the low temperatures while it was nicely located at the middle of the measured shear rate range at higher temperatures.

Figure 5.5 shows the temperature dependence of the obtained maximum slope values, that are the exponent values for the power law region in the viscosity-shear-rate curve. The power law region of the viscosity-shear-rate had a high exponent value $m_{apparent} = 0.885 \pm 0.004$ at low T, then the exponent value decreases continuously until it reaches a lower value $m_{apparent} \sim 0.1$ with increasing T.

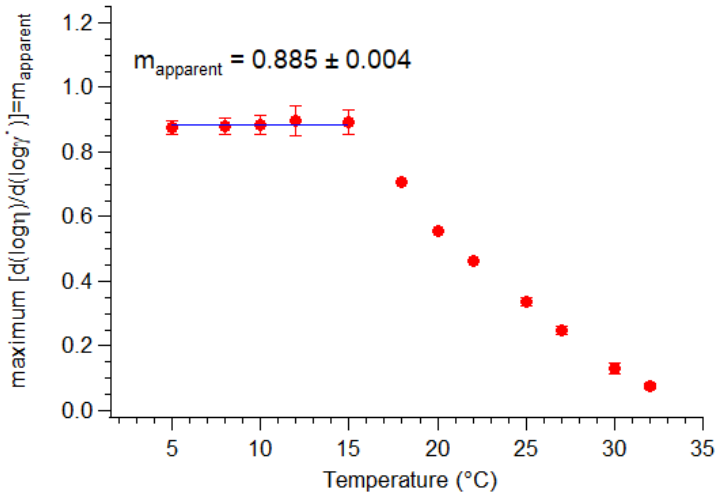

Figure 5.5: The power law exponent (slope) test results for the microgel sample of C_d=13.6 wt% and C=8 wt%, as a function of temperature. The constant fit at low temperature range, is consistent with power law exponent $m = 0.9$ at least at the lowest temperatures.

By correlating the exponent $m_{apparent}$ behavior with temperature and the viscosity curves' shapes in Figure 5.3 to the Cross picture, one can see that the microgel viscosity as a function of temperature shows two behaviors. The first regime, corresponding to the low temperatures (less than 18°C) in Figure 5.3, is one where the viscosity-shear-rate relation shows a strong shear-thinning behavior with a high value of the exponent $m_{apparent} \sim 0.9$: here, the low-shear-plateau η_0 presumably occurs at $\dot{\gamma}$ lower than those probed in our experiments. In the second regime, corresponding to higher temperatures ($T > 15$°C) in Figure 5.3, the microgel exhibited a weaker shear-thinning and thus a lower exponent value of the intermediate power law region with ($0.2 < m_{apparent} < 0.9$). At high temperatures (from 27°C to 32°C in Figure 5.3) there is very weak shear-thinning behavior with the low value of the exponent ($m_{apparent} \lesssim 0.2$) corresponding to the power law region. A possible behavior is that the gel character of the microgel suspensions is unchanging below 15°C but is in fact temperature dependent above 15°C.

5.2.1.2 Zero-shear viscosity determination

The Cross equation (see Section 2.3.2, equation 2.9) was used to fit the results and determine η_0 (which can also be read off, approximately, from the first plateau), η_∞ (which can also be read off, approximately, from the second plateau), and the relaxation constant τ. The global fit procedure in Igor Pro was utilized to find these three coefficients. The Cross fitting method was employed to obtain the η_0 for the temperatures at which the microgel was in a cross-over region from the strong shear-thinning behavior to the very weak shear-thinning behavior (the intermediate power law region where: $0.9 > m_{apparent} > 0.2$).

Figure 5.6 shows the Cross fits for the three curves at 20°C, 25°C, and 27°C for the microgel suspension of C_d=13.6 wt% and C=8 wt%, that were performed in two ways: (a) by linking the exponent m in the fit equation for all the fitted curves, (b) by letting m as a fourth coefficient to be found by the fitting procedure for each individual curve. It can be seen from the figure that the results obtained by holding all power laws to one fitted value ("linking m") are not distinguishably different (within errors) from the results of the fit where m runs free. In particular, the value we care most about, η_0, is barely affected, within errors. Table 5.2 shows the obtained parameters, η_0, η_∞, and τ. The obtained η_0 values from both fitting methods had relative uncertainties less than 4% and varied slightly. In order to reduce the number of fitting coefficients to be found by the procedure and take advantage of the fitted curves being in the same region with an intermediate exponent value $m_{apparent}$, the Cross fit was always done while linking m to be one value in the fit for each sample, similar to what is done in Figure 5.6 (a).

The absolute uncertainties obtained from the fitting procedures were always less than 5% relative to the values obtained. Thus a relative uncertainty of 5% was used to weight the fitting in the Cross procedure.

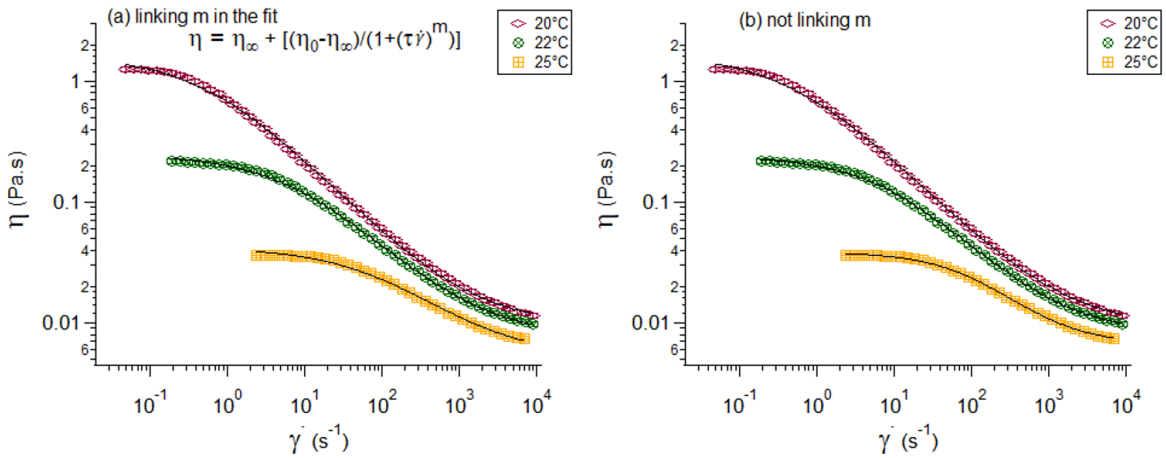

Figure 5.6: Examples for fits to the Cross equation, equation (2.9) a) linking the power law m and b) not linking m, for the three viscosity-shear-rate measurements at 20, 22, and 25°C, for the microgel sample of C_d=13.6 wt% and C=8 wt%. The Cross equation is shown above the fitted curves in (a).

Table 5.2: Comparison of fits with and without a linked power law m for the microgel sample of C_d=13.6 wt% and C=8 wt%. For all fits the obtained coefficients of (η_0, η_∞, τ, and m) lay within the uncertainties in the brackets.

	linked m [obtained as: 0.68 (1)]			unlinked m			
T (°C)	η_0 (mPa·s)	η_∞ (mPa·s)	τ (s)	η_0 (mPa·s)	η_∞ (mPa·s)	τ (s)	m
20	1617 (48)	9.6 (3)	1.6 (1)	1668 (55)	9.2 (4)	1.8 (2)	0.67 (1)
22	246 (5)	7.7 (3)	0.126 (8)	239 (6)	8.2 (4)	0.11 (1)	0.71 (2)
25	42 (1)	5.3 (3)	0.011 (1)	38 (1)	6.6 (4)	0.009 (1)	0.87 (6)

At higher temperatures (27°C, 30°C, and 32°C), in the region of weak shear-thinning, η_0 could also be estimated from the slope of the linear fit of the stress *versus* shear rate ($\sigma - \dot{\gamma}$) relation over low shear range (see Section 2.3.1). In order to test the consistency of the η_0 obtained by the Cross fit at low temperatures with the η_0 obtained by the linear fit of the stress at low $\dot{\gamma}$, η_0 values were re-obtained at lower temperatures by the linear fit method. Figure 5.7 shows these linear fits for low shear rates for all the temperatures to find the η_0 for the same sample of 13.6 BIS/mon wt% and at 8 wt%. The fit equation is shown on the top of the figure. The y-intercept, which represents the yield stress (σ_0), had a very small

value for this sample at all temperatures. These linear fits are progressively poorer at lower temperatures, and should thus be considered as lower bounds on η_0 in this regime. The fitted value for σ_0 value was 0.018 ± 0.008 Pa. The obtained η_0 values with their uncertainties are listed in Table 5.3 below. All the η_0 values had relative uncertainties less than 2%.

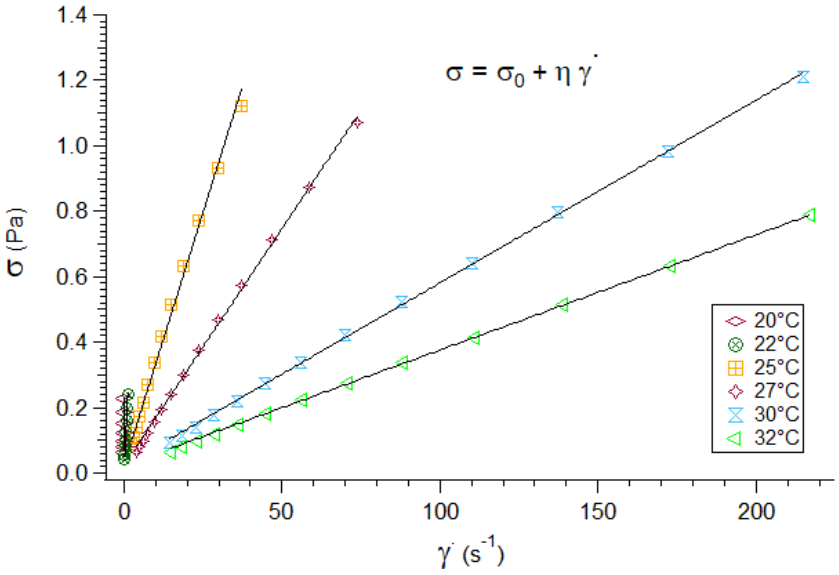

Figure 5.7: The linear fits of the stress *versus* shear rate over the low shear rate region to determine η_0 values at the colloidal regime temperatures 25, 27, 30 and 32°C for the microgel sample of of C_d=13.6 wt% and C=8 wt%.

Table 5.3: η_0 obtained from linear fits of σ *vs* $\dot{\gamma}$, in the limit of low $\dot{\gamma}$, for the microgel sample of C_d=13.6 wt% and C=8 wt%. The η_0 obtained by Cross fits, at low T, are also presented for comparison.

	Linear	Cross
T (°C)	η_0 (mPa·s)	η_0 (mPa·s)
20	1117 (14)	1617
22	195 (2)	246
25	30.9 (3)	42
27	14.5 (1)	-
30	5.58 (5)	-
32	3.52 (5)	-

Figure 5.8 shows a comparison of the obtained values of η_0 using both methods for this

sample as a function of temperature. At temperatures where both methods were used to determine η_0, they gave consistent results within the same order of magnitude but with the values from the linear fits being systematically lower, as expected. Thus the Cross fit results at these temperatures were taken. From the figure, it can be seen that the zero shear viscosity decreases as temperature increased.

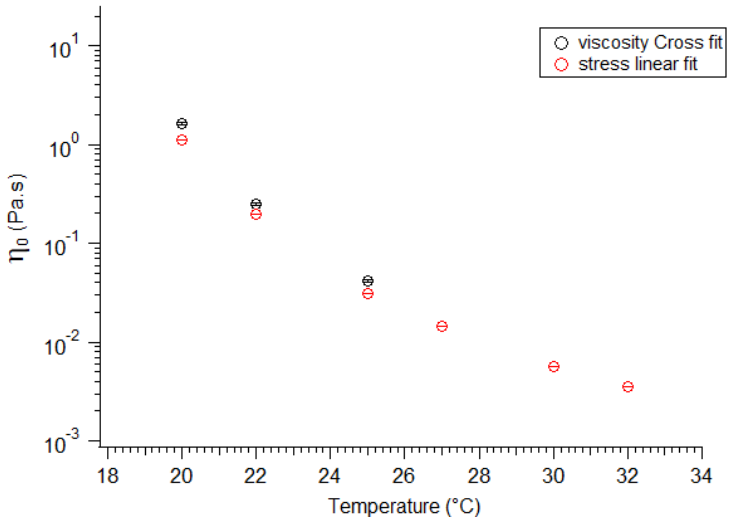

Figure 5.8: The determined η_0 values *versus* temperature for the microgel sample of C_d=13.6 wt% and C=8 wt%, using the Cross fit to the viscosity at low T and the linear fit to the stress, *versus* the strain rate, at all temperatures. As can be seen, at the temperatures where both methods are used the results are consistent, with the linear being systematically lower.

Sixteen steady flow experiments, in total, each at numerous temperatures, were done to measure the flow curves of the four crosslinked microgels at four different concentrations for each C_d. Similar analyses were carried out to find the temperature dependences of $m_{apparent}$ and η_0 for each sample. Eight samples out of sixteen exhibited three distinct regions as a function of strain rate $\dot{\gamma}$: a low $\dot{\gamma}$, η_0, a high $\dot{\gamma}$ plateau, η_∞, and a shear-thinning (power law) region in between. Thus the Cross fit of η *vs* $\dot{\gamma}$ was the tool for the determination of η_0 for these cases. Linear fits of σ *vs* $\dot{\gamma}$ were carried out for all samples that exhibited a low $\dot{\gamma}$ plateau in viscosity. For the cases where both fitting methods (Cross fit and linear fit) were used to determine η_0, both methods gave consistent results. Figure 5.9 shows the

comparisons between η_0 found in both ways for the eight samples, including the example sample above. All the obtained η_0 as a function of temperature for the sixteen samples with different C_d and C are listed in Table 5.4. For the Cross fits, shown in Table 5.4 highlighted in green, the obtained power law exponent m is also listed in the right-most column. The solvent (water) viscosity η_s as a function of temperature was reported in the table as well, to allow us to determine the relative viscosities $\eta_{rel}(T) = \eta_0(T)/\eta_s(T)$.

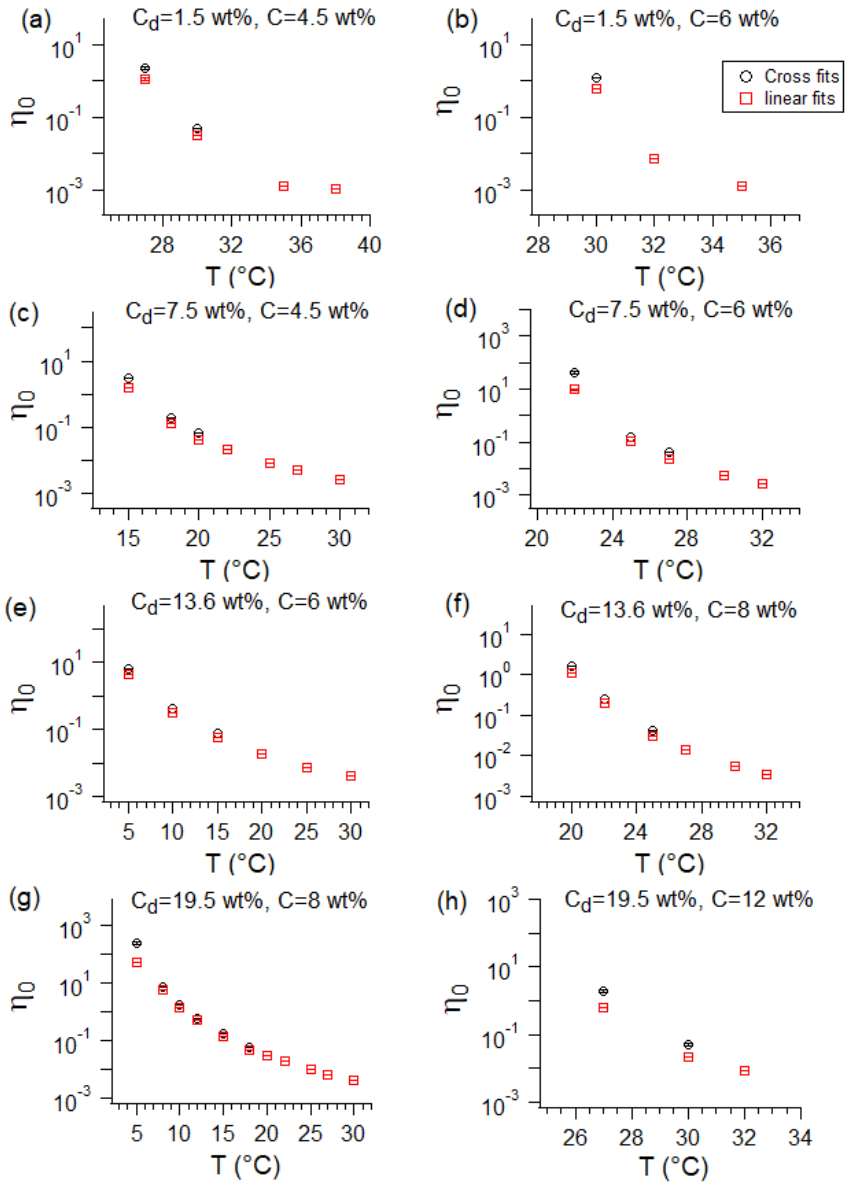

Figure 5.9: The zero-shear viscosity, η_0 obtained by both Cross and linear fits, *versus* temperature for the eight samples of microgels a) C_d=1.5 wt%, C=4.5 wt% b) C_d=1.5 wt%, 6 wt% c) C_d=7.5 wt%, C=4.5 wt% d) C_d=7.5 wt%, 6 wt% e) C_d=13.6 wt%, C=6 wt% f) C_d=13.6 wt%, 8 wt% g) C_d=19.5 wt%, C=8 wt% h) C_d=19.5 wt%, 12 wt%. The results from Cross fits and linear fits are plotted in black circles, and red squares, respectively.

Table 5.4: The obtained η_0 values, along with the type of fit that was used to determine them ("L" for linear fit, and "C" for Cross fit) for all the 16 samples at different C_d, C, and T. The η_s values as a function of temperature are listed as well, in the first Section to the left. For the samples were Cross fits had been used, highlighted in green, the m values as obtained by the Cross fits are listed.

Water		C_d=1.5 BIS wt%				C_d=7.5 BIS wt%				C_d=13.6 BIS wt%				C_d=19.5 BIS wt%			
T (°C)	η_s (mPa.s)	C (wt%)	T (°C)	η_0 (mPa.s)	fit	C (wt%)	T (°C)	η_0 (mPa.s)	fit	C (wt%)	T (°C)	η_0 (mPa.s)	fit	C (wt%)	T (°C)	η_0 (mPa.s)	fit
5	1.55 (8)	1.5	5	16 (1)	L	1.5	5	4.4 (2)	L	1.5	5	2.7 (1)	L	1.5	5	2.6 (1)	L
8	1.43 (7)		8	12 (1)	L		8	4.0 (2)	L		10	2.1 (1)	L		8	2.3 (1)	L
10	1.36 (7)		10	11 (1)	L		10	3.4 (2)	L		15	1.9 (1)	L		10	2.1 (1)	L
12	1.28 (6)		12	9.2 (5)	L		12	3.3 (2)	L		20	1.5 (1)	L		12	1.9 (1)	L
15	1.18 (6)		15	7.2 (4)	L		15	2.7 (1)	L		25	1.3 (1)	L		15	1.7 (1)	L
18	1.09 (5)		18	5.5 (3)	L		18	2.4 (1)	L		30	1.1 (1)	L		18	1.6 (1)	L
20	1.03 (5)		20	4.7 (2)	L		20	2.1 (1)	L	4.5	5	19 (1)	L		20	1.4 (1)	L
22	0.97 (5)		22	4.0 (2)	L		22	1.9 (1)	L		8	14 (1)	L		22	1.3 (1)	L
25	0.90 (4)		25	3.1 (2)	L		25	1.7 (1)	L		10	11 (1)	L		25	1.2 (1)	L
27	0.85 (4)		27	2.5 (1)	L		30	1.4 (1)	L		12	9.4 (5)	L		27	1.1 (1)	L
30	0.78 (4)		30	2.1 (1)	L	4.5	15	30 (2) E2	C 0.64 (1)		15	7.2 (4)	L		30	1.1 (1)	L
32	0.74 (4)	4.5	27	23 (1) E2	C 0.62 (1)		18	19 (1) E1	C		18	5.6 (3)	L	4.5	5	8.1 (4)	L
35	0.68 (3)		30	49 (2)	C		20	66 (3)	C		20	4.8 (2)	L		8	6.6 (3)	L
38	0.63 (3)		35	1.3 (1)	L		22	21 (1)	L		22	4.1 (2)	L		10	6.0 (3)	L
			38	1.1 (1)	L		25	7.8 (4)	L		25	3.1 (2)	L		12	5.3 (3)	L
		6	30	12 (1) E2	C/0.60(1)		27	4.9 (2)	L		27	2.7 (1)	L		15	4.4 (2)	L
			32	7.1 (4)	L		30	2.6 (1)	L		30	2.2 (1)	L		18	3.6 (2)	L
			35	1.3 (1)	L	6	22	40 (2) E3	C 0.66 (0)		32	1.8 (1)	L		20	3.2 (2)	L
		8	32	31 (2)	L		25	16 (1) E1	C	6	5	67 (3) E2	C 0.67 (1)		22	2.9 (1)	L
			35	1.5 (1)	L		27	43 (2)	C		10	41 (2) E1	C		25	2.4 (1)	L
							30	5.2 (3)	L		15	80 (4)	C		27	2.2 (1)	L
							32	2.7 (1)	L		20	19 (1)	L		30	2.0 (1)	L
						8	30	4.6 (2)	L		25	7.3 (4)	L	8	5	25 (1) E4	C 0.69 (0)
							32	1.7 (1)	L		30	4.3 (2)	L		8	75 (4) E2	C
										8	20	16 (1) E2	C 0.68 (1)		10	18 (1) E2	C
											22	25 (1) E1	C		12	60 (3) E1	C
											25	42 (2)	C		15	17 (1) E1	C
											27	15 (1)	L		18	59 (3)	C
											30	5.6 (3)	L		20	30 (2)	L
											32	3.5 (2)	L		22	20 (1)	L
															25	9.9 (5)	L
															27	6.6 (3)	L
															30	4.4 (2)	L
														12	27	20 (1) E2	C 0.65 (1)
															30	50 (2)	C
															32	8.8 (4)	L

In all samples, we see in Figure 5.9 that η_0 decreases sharply with increasing temperature T. At a fixed T, η_0 increases with concentration C. This is true for all crosslink densities C_d.

5.2.2 Relative viscosity as a function of temperature

One can get information on colloidal structure by an investigation of the relative viscosity $\eta_{rel} = \eta_0/\eta_s$, as a function of T, C_d, and C, of the studied microgel samples. These relative viscosities may be calculated from the η_0 and η_s values listed in Table 5.4.

Figure 5.10, below, correlates the power law $m_{apparent}$ with the obtained relative viscosity η_{rel}, for all the studied samples. Figure 5.10 (a, c, e, g) shows $m_{apparent}$ as a function of T and C for crosslink densities C_d=1.5, 7.5, 13.6, and 19.5 wt%, respectively. Figure 5.10 (b, d, f, h) shows η_{rel} as a function of the same parameters.

At the lowest crosslink density C_d=1.5 wt%, in Figure 5.10 (a), the lowest concentrated microgel sample of C=1.5 wt% had $m_{apparent} \sim 0.2$ at all temperatures, from 5°C to 30°C. The corresponding η_{rel}, is less than 10 and decreases with temperature as shown in Figure 5.10 (b).

On the other hand, for higher concentrations, C=4.5 wt% and above, $m_{apparent}$ ~0.9 at low T and decrease sharply above 25°C. Similar behavior was seen at higher crosslink densities (Figure 5.10 (c-h)).

All the $m_{apparent}$ plots, at different C_d, exhibit some common features. First, there is a plateau at $m_{apparent}$ ~0.9 at low T (but higher C). In this plateau region, η_{rel} is in fact not measurable, but certainly much higher than 10^4. By this we identify with the gel-like regime. Second, at the lowest concentrations, one observes a low $m_{apparent}$ ~0.2 for all C_d. This correlates with an η_{rel} in the range 1 - 10 that exhibits a weak decrease with temperature. Third, there is a crossover in $m_{apparent}$, which occurs at different temperatures for different values of C_d and C. In this crossover regime, η_{rel} is measurable and large (10^3 - 10^4) at low T, but decreases sharply with temperature.

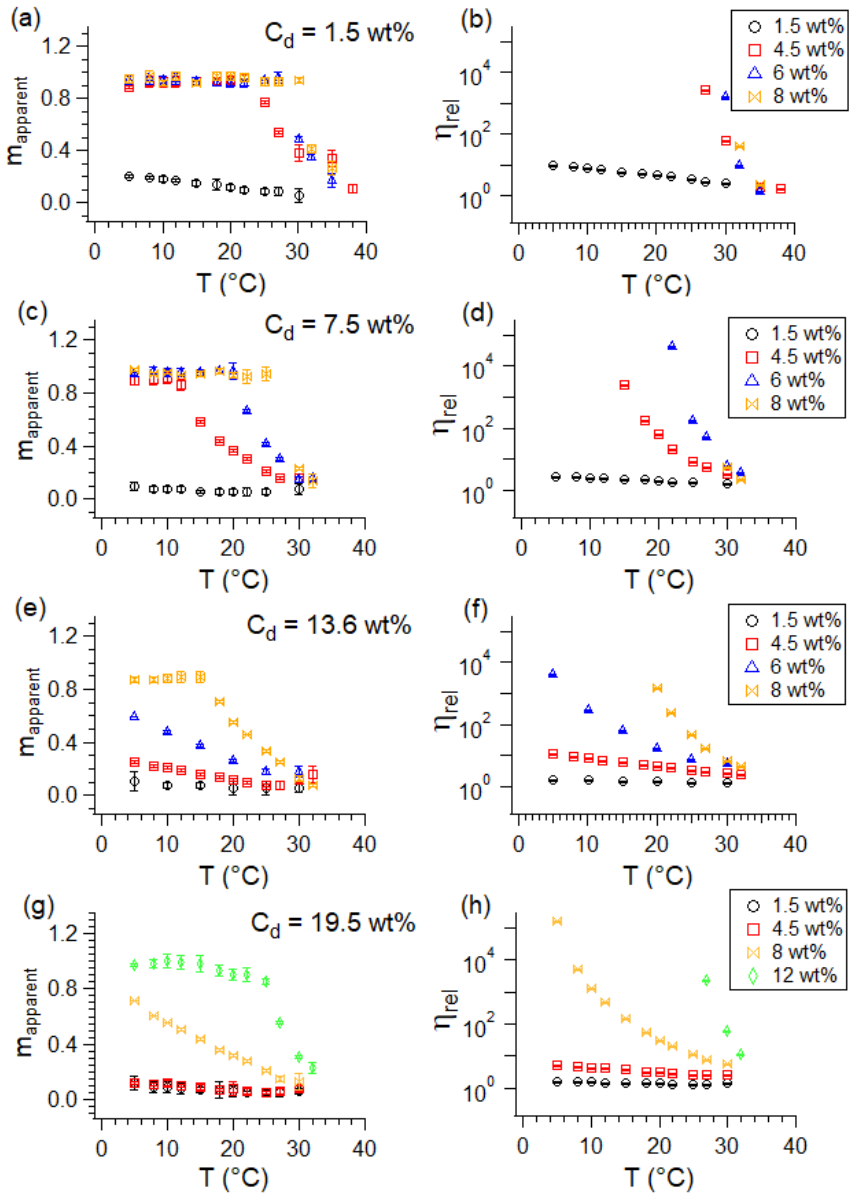

Figure 5.10: The power law exponent $m_{apparent}$ (a, c, e, g) and the relative viscosity η_{rel} (b, d, f, h) dependence of temperature for the samples made at different concentrations from the microgels with C_d=1.5, 7.5, 13.6 and 19.5 wt%, respectively.

5.2.3 Summary of small-amplitude oscillatory shear (SAOS) results

For selected temperatures, SAOS tests were carried out to obtain the storage modulus G' and the loss modulus G'' as a function of angular frequency ω. In the low ω limit, the loss tangent $\tan\delta = G''/G'$ (equation (2.15)), may be compared with the results from steady

shear.

Figure 5.11 (a, b, c, d) shows the obtained G''/G' ratios, i.e. the loss tangents, from all the SAOS experiments as a function of T, at different C, for C_d= 1.5 wt%, 7.5 wt%, 13.6 wt%, and 19.5 wt%, respectively.

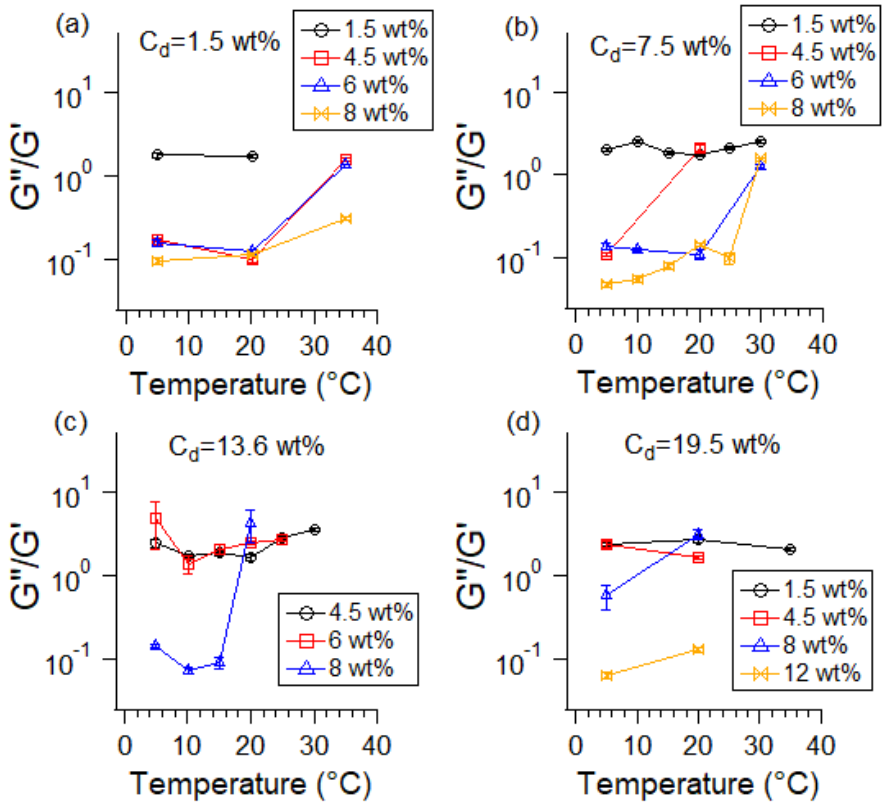

Figure 5.11: The loss to storage moduli ratio "loss tangent" *versus* T for all the studied samples at different C for a) C_d=1.5 wt% b) C_d=7.5 wt% c) C_d=13.6 wt%, and d) C_d=19.5 wt%.

Figure 5.11 shows that for all the crosslink densities, G''/G' is larger than 1 at low C and high T while less than 1 for higher C and lower T. This is an indication that the sample is more elastic at higher concentration and lower temperature. This is consistent with what was indicated from the steady shear determinations of $m_{apparent}$ and η_{rel}, showing that the microgel behaves like soft spheres at these conditions. As an example for C_d=1.5 wt%, only the lowest concentration, C=1.5 wt%, has a low $m_{apparent}$ (Figure 5.10 (a)) for $T < 20$°C. Correspondingly, the loss tangent is only high (order 1) for this sample (Figure 5.11 (a)).

The raw storage and loss moduli *versus* the angular frequency at comparable temperatures and concentrations are presented in the Appendix (see figures A.1 - A.4). For the SAOS study, one can conclude that the softest microgel particles, with the larger elastic moduli, are those corresponding to the highest concentrations. Also, the increase of the crosslink density in microgels leads to stronger colloidal behavior at low C but stronger elastic behavior at high C.

5.2.4 Calculation of microgel particle volume fractions

One possibility is that the decrease of η_{rel} with T could arise from the decrease in particle volume with increasing T. The relative viscosities, in the collapsed phase, at high temperatures and different concentrations, were therefore used to calculate the k factor, that is the nipam volume per particle(see Section 4.3.5).

For each crosslink density, equation (4.11) was used to calculate k values for a range of concentrations at selected temperatures in the collapsed phase. For a given crosslink density and temperature, the particle volume v_p was taken from the DLS measurements. The nipam density used was ρ_{nipam}=1.1 g/cm^3 and the maximum packing fraction for hard spheres in random close packing was ϕ_{max}=0.63. For each crosslink density, the k values obtained at different sample concentrations for a selected temperature in the collapsed phase were averaged to obtain the collapsed-phase value of k for that crosslink density. Figure 5.12 (a) shows a plot of the average k against the corresponding particle volumes v_p at 45°C for each crosslink density. k_{avg} is found to be proportional to v_p(45°C). Figure 5.12 (b) shows that the ratio $k/v_p(45)$ is independent of crosslink density. Using the information in equation (4.5) that $\frac{k}{v_p} = 1 - f$ is the nipam fraction of the particle volume, one can conclude that this fraction is 0.4±0.04 for all crosslink densities, in the collapsed phase.

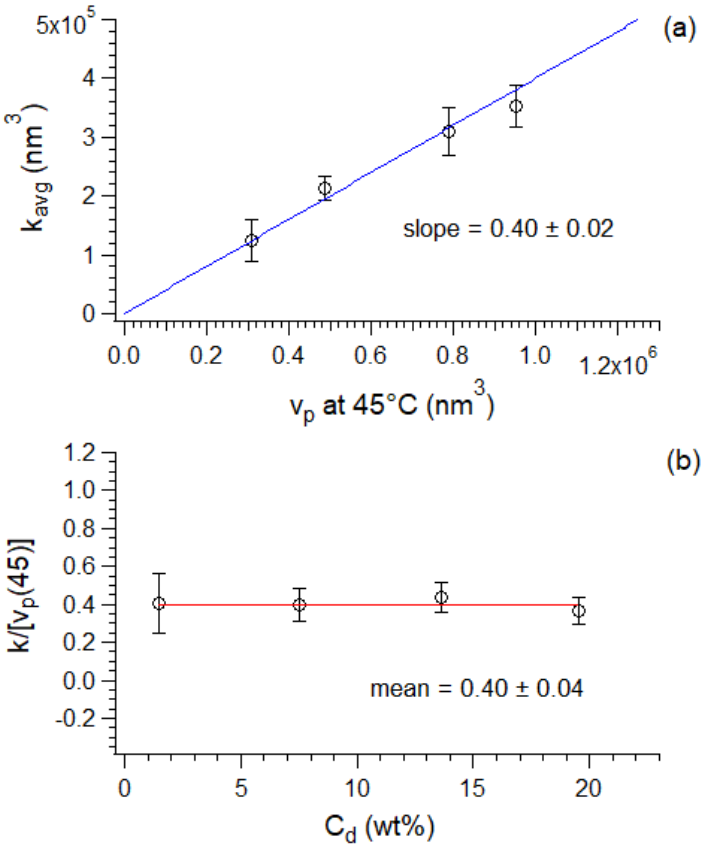

Figure 5.12: (a) Average calculated k factor for different C_d *versus* the particle volume at 45°C at the 4 crosslink densities: the highest v_p corresponds to the lowest C_d. (b) The $(k/v_p(45))$ ratio is independent of C_d.

Using equation (4.9), i.e. $\phi = \dfrac{v_p}{k[1+(\dfrac{1}{C}-1)\dfrac{\rho_{nipam}}{\rho_w}]}$, the particle volume fraction ϕ as a function of T at each concentration C was obtained by substituting the k_{avg} for the corresponding C_d. Because this equation is only strictly valid in the absence of particle overlap or compression, we refer to this as the effective volume fraction (ϕ_{eff}). In the presence of particle overlap, the effective $v_p \equiv \dfrac{V_p}{N}$ will be smaller than the volume inferred from DLS.

The calculated ϕ_{eff} as a function of temperature are shown below, in Figure 5.13 (a), (b), (c), and (d) for the microgel samples with C_d= 1.5, 7.5, 13.6, and 19.5 wt%, respectively. At low temperatures, where the microgel particle was in the swollen phase, the particle volume fraction ϕ_{eff} is the largest while as temperature increased the particles collapsed and thus

the ϕ_{eff} decreases. Within the same C_d, as the concentration of the sample increases the ϕ_{eff} increases.

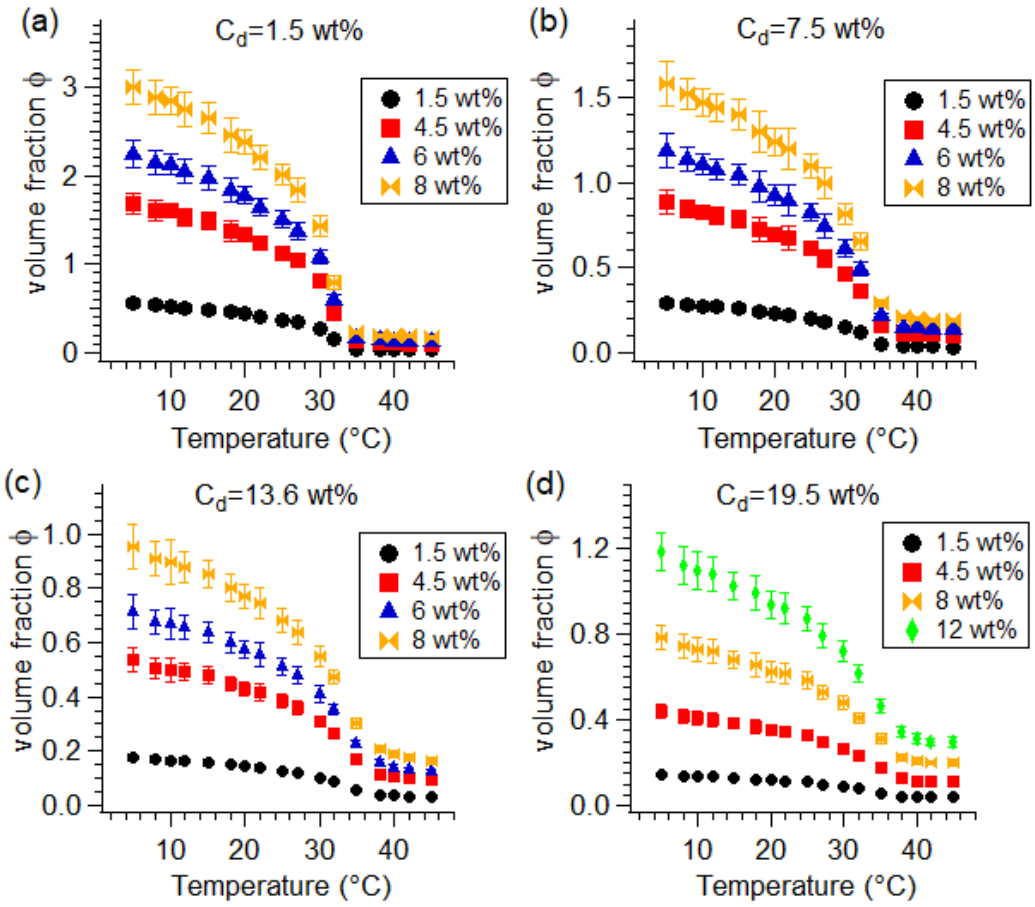

Figure 5.13: The dependence of volume fraction ϕ_{eff}, calculated from particle volume obtained from DLS carried out at low concentration C, on temperature T for the studied microgel samples at different concentrations corresponding to C_d= (a) 1.5 wt%, (b) 7.5 wt%, (c) 13.6 wt%, and (d) 19.5 wt%.

The highest volume fraction ϕ_{eff} ~3, was achieved by the lowest crosslink density microgel C_d=1.5 wt% and at the highest concentration 8 wt%. When particles have $\phi_{eff} > 1$ that can be the result of particles overlap or squeeze due to their high elasticity. At the same concentration, say C=8 wt%, and different C_d one can notice that the volume fraction decreased from 3 to 0.8 as the C_d increased. This is because of the decrease of the swelling factor as the crosslink density increased. In order to achieve higher volume fractions at high

C_d, higher concentration samples need to be prepared.

5.2.5 Water fraction in the particle

As explained above, the mean value of k was found for each C_d. From this, the nipam fraction in the particle as a function of T was calculated by finding the k/v_p ratio using the particle volumes at different T. The water volume fraction f as a function of temperature was then simply obtained using f=1 - k/v_p. Figure 5.14 below shows f values as a function of T for all crosslink densities, C_d. The water fraction in the particle decreases from a swollen phase value ranging from 0.91 - 0.98, depending on C_d, to a value ranging from 0.56 - 0.68 in the collapsed phase. It is notable that, even in the collapsed phase, water accounts for at least 50% of the particle volume.

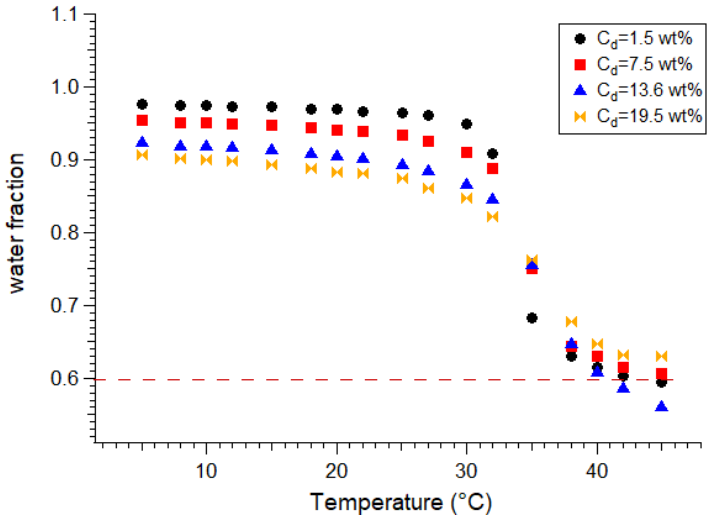

Figure 5.14: Water fractions in the microgel particle as a function of T for the 4 crosslink densities.

5.2.6 Relative viscosity-volume fraction behavior

The relative viscosities as a function of the calculated volume fractions ϕ_{eff} are plotted in Figure 5.15. The Krieger-Dougherty function was also plotted in the figure for the comparison to colloidal hard sphere behavior. The microgel relative viscosities, η_{rel}, were consistent with the Krieger-Dougherty (KD) line at low volume fractions up to $\sim$ 0.3. It is not surprising

that this corresponds to results at high temperatures, in the collapsed phase, because the k factor to calculate ϕ_{eff} was determined using the KD model. For higher volume fractions the data deviated from the KD line since the particles are softer in the swollen phase. The purpose of this plot was to examine the possibility of collapsing all datasets (4 concentrations, 4 crosslink densities, several temperatures) onto a universal curve. Such a collapse is in fact only achieved for $\phi_{eff} < 0.6$. If there was collapse onto a universal curve, it would suggest that particles properties and interactions are independent of the multiple control parameters (T, C, C_d) and just dependent on ϕ_{eff}. What we have found is that this is not the case.

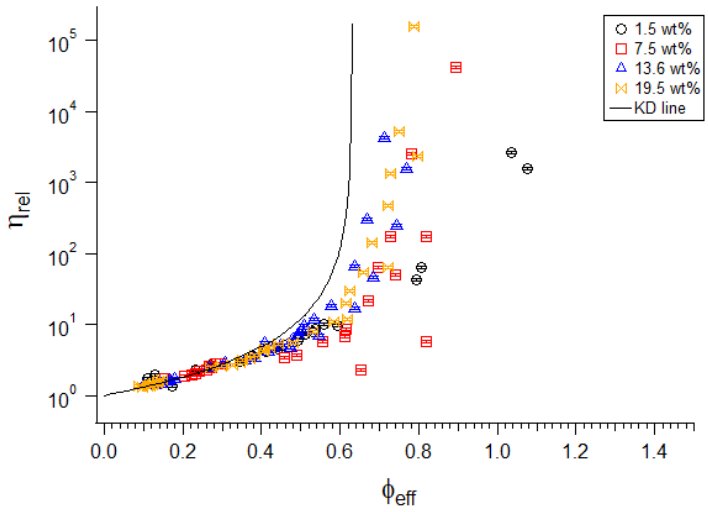

Figure 5.15: Summary figure for all relative viscosity data *versus* the effective volume fraction, for all the microgels samples at different C, T and C_d. The Krieger-Dougherty (KD) line was plotted for the comparison to the colloidal suspension hard sphere behavior.

Given the absence of data collapse for $\phi_{eff} > 0.6$, the dependence of $m_{apparent}$ and η_{rel} as a function of ϕ_{eff} was examined for the 4 crosslink densities. Figure 5.16 (a, c, e, g) and Figure 5.16 (b, d, f, h) show $m_{apparent}$ and η_{rel} as a function of ϕ_{eff} for microgels at C_d= 1.5, 7.5, 13.6, and 19.5 wt%, respectively. The KD line was plotted on each $\eta_{rel} - \phi_{eff}$ sub-figure for comparison to the colloidal hard sphere behavior. The onset of the plateau in $m_{apparent}$ occurs in the range 0.8< ϕ_{eff} <1.2. As temperature increases, in the direction indicated by the dark red arrow at the top of the figures, $m_{apparent}$ and η_{rel} decrease sharply

and the gel-like behavior becomes weaker. The volume fraction corresponding to $\eta_{rel} = 10^3$, is approximately ϕ_{eff}=1.05 for C_d=1.5 wt%, ϕ_{eff}=0.8 for C_d=7.5 wt%, and ϕ_{eff} ~0.7 - 0.75 for the two higher crosslink densities. For comparison, the KD hard sphere curve yields $\eta_{rel} = 10^3$ at ϕ_{eff}=0.62, so it is apparent that the behavior is becoming more hard-sphere-like at higher C_d.

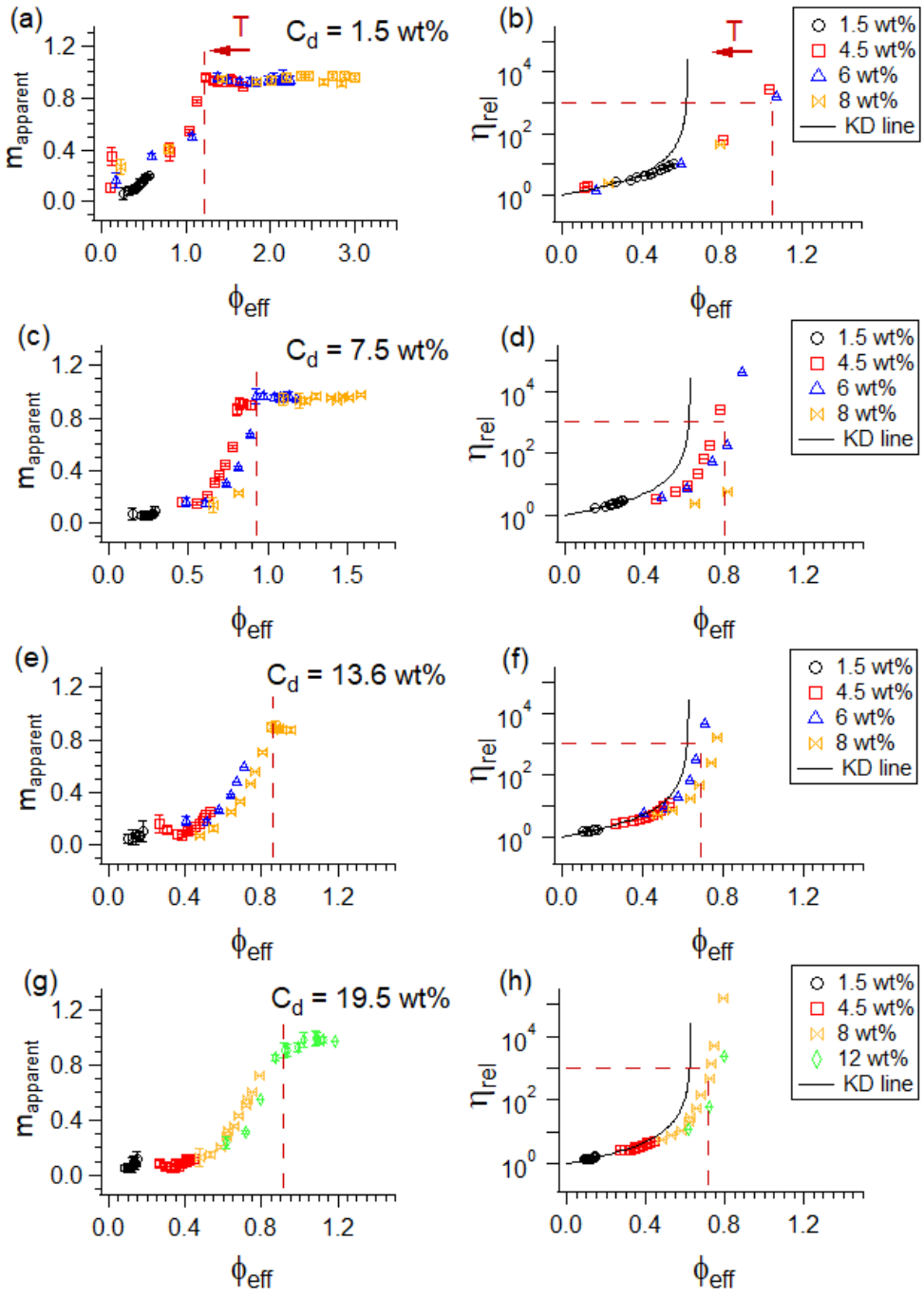

Figure 5.16: The power law exponent $m_{apparent}$ (a, c, e, g) and the relative viscosity η_{rel} (b, d, f, h) dependence of the effective volume fraction ϕ_{eff}, for the samples made at different concentrations from the microgels with C_d=1.5, 7.5, 13.6 and 19.5, respectively. The dark red arrow at the top of (a and b) shows the direction of temperature increase for all data sets.

5.3 Insights from DLS and rheology results

The DLS results indicated that the highest swelling capacity is seen for the lowest crosslinked microgel. The transition temperature was found to be about 35°C for all of the studied microgels. The transition temperature was found to increase slightly with increasing C_d. This is consistent with previous studies [18, 21].

The investigation of the apparent power law exponent behavior with temperature helped in identifying the gel-like and colloid-like regimes in the microgel. The viscosity behaviour measured from the steady shear flow experiments showed a gel-like regime of the microgel at low temperature and high concentrations and a colloid-like regime at high temperatures and low concentrations. This can be seen quantitatively in Table 5.5; the low zero-shear-viscosity values, on the order of 10 mPa·s, correspond to the colloid-like regime while the high zero-shear-viscosity values, on the order of 10^2-10^5 mPa·s, correspond to the gel-like regime. Cross-over from the gel-like regime to the colloid-like regime was apparent for a range of concentrations, temperatures and crosslink densities. The Cross equation was used to find the zero-shear viscosity from the viscosity-shear-rate relation, for the low temperatures in the cross-over regime, and led to η_0 values consistent with the values found by the linear fits of the stress-shear-rate relations. This consistency between the obtained η_0 values, from both methods, can be seen in Figure 5.9. From the plotted $m_{apparent}$ in Figure 5.10 along with the relative viscosities, for all studied samples, one can see clearly the three regimes of the microgel as a function of temperature, concentration, and crosslink density.

The small amplitude oscillatory shear measurements were consistent with the steady shear flow measurements, and showed clearly the change of the microgel from elastic behaviour in the gel-like regime to viscous behavior in the colloid-like regime. Similar observations were reported by Senff and Richtering [18].

Volume fraction calculations showed that the highest effective volume fractions were achieved at the lowest crosslink density. Also, they revealed that, in the collapsed phase, a

considerable fraction of the particle's volume, $\sim$60%, is accounted for by water.

The relative viscosity as a function of the effective volume fraction, in Figure 5.16, showed that the largest deviation from hard-sphere behaviour, happened at the lowest crosslink density. The microgel was mostly soft at the lowest crosslink density, as can be seen from the $\sim$0.9 values for the $m_{apparent}$, in the same figure.

Chapter 6

^{2}H NMR Experimental Results

The energy of a deuteron bonded to a carbon is perturbed by the orientation-dependent quadrupole interaction. The deuterium NMR spectrum of a deuterated molecular segment reflects the extent to which the average quadrupole interaction is reduced by bond and molecular reorientations that are fast on the timescale of the NMR experiment. Deuterium NMR thus gives a way to distinguish populations of molecule segments undergoing large or small amplitude reorientation with correlation times that are short or long on the deuterium NMR time scale.

The quadrupole interaction is sensitive to polymer segment reorientation and from the observed superpositions of the spectral components it is possible to get information about the sizes of polymer segment populations in environments where they experience different degrees of motional freedom.

In this work the structure and dynamics of deuterated nipam microgel particles were studied, using deuterium NMR spectroscopy, as a function of temperature, pressure, and crosslink density. The goal of applying deuterium NMR to microgel colloids in this work was to try to gain some insight into how the collapse transition for microgel particles affects the fractions of polymer undergoing large or small amplitude reorientations for samples with different crosslink densities.

For these experiments, microgels were synthesized from the deuterated monomer with the four different C_d values: 1.5, 7.5, 13.6, 19.5 wt% BIS to monomer. Dry NMR samples were made from deuterated crosslinked polymer in dry powder form while the suspensions were made by mixing the dry powder with deuterium depleted water. All microgel suspensions used for NMR were prepared at 20 wt% concentration. Using the spectrometer based on a 9.4 T magnet, a series of ambient pressure spectra at different temperatures was collected for each crosslink density. Series of spectra spanning ranges of pressure and temperature were then collected for each crosslink density using a variable-pressure NMR probe in a spectrometer based on a wide-bore 3.5 T.

No previous studies of polynipam systems using solid-state deuterium NMR have been reported so the first step was to determine if it is possible to obtain a spectrum from a deuterated polynipam suspension and whether the collapse transition and polymer motions were better characterized by spectra obtained using sidechain or backbone deuteration.

In this work, deuterium NMR spectra were first obtained from polynipam that was deuterated on the methyl groups and nitrogen of the mobile side chains. These spectra, collected over a range of temperatures, were sensitive to the collapse transition but in order to simplify the spectral interpretation, by reducing the number of motional degrees of freedom, it was decided to synthesize polynipam, at different crosslink densities, using monomers that resulted in the deuterons being restricted to the polymer backbone. These experiments were carried out at 9.4 T in an ambient pressure probe that allowed for a relatively larger sample size.

A variable-pressure probe in a spectrometer operating at 3.5 T was also used to investigate the effect of hydrostatic pressure on colloid properties including the collapse transition. Compared to the ambient pressure experiments, the NMR in signals available in the variable pressure experiments were limited by both the relative smaller magnetic field and by the small volume accessible in the variable-pressure probe.

6.1 d7 nipam suspensions

The first deuterated microgel material was kindly provided by a collaborator, Dr. Priti Mohanty (KIIT University, India), who used sidechain-deuterated nipam monomer to synthesize a microgel polymer with a crosslink density 7.5 wt%. The d7 monomer has 6 deuterons on side chain methyl groups and one amide deuteron. Figure 6.1 shows where the monomer side chain is deuterated.

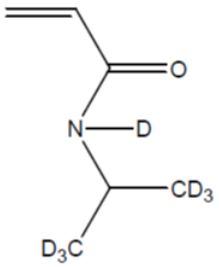

Figure 6.1: The chemical structure of d7 nipam.

Suspensions of d7 nipam were prepared from this polymer powder and deuterium depleted (d-d) water. It was necessary to use d-d water for the nipam suspensions to avoid the HOD signal that is at a slightly different chemical shift compared to the C-D signal and thus can interfere with tuning to the narrow nipam spectrum if normal water is used. Microgel suspensions at room temperature were very sticky and difficult to manipulate. Microgel suspensions were prepared at high concentrations in order to limit the possibility of whole particle tumbling in the swollen phase. For NMR experiments, d7 nipam suspensions, were prepared with volumes of $\sim$300 μL. Each sample was transferred to a $\sim$400 μL NMR tube which was closed with a Teflon plug, wrapped with Teflon tape, and then inserted into the coil of the 9.4 T magnet probe. NMR experiments were carried out on d7 nipam suspensions prepared at concentrations of 5 wt% and 20 wt%. FIDs on the 9.4 T magnet were collected using a digitizer with a fixed dwell time at (1μs/pt) and then contracted to give longer effective dwell times appropriate to the spectral width required for a given spectrum.

Figure 6.2 (a) shows deuterium NMR spectra for a series of temperatures obtained from

the 5 wt% d7 nipam suspension. For all temperatures studied, the spectra consist of a narrow peak characteristic of nearly isotropic reorientation for most of the deuterated segments. The wings of the narrow line likely reflect the presence of a small number of more constrained segments with a broad, nearly continuous distribution of doublet splittings. Before Fourier transformation, the FIDs were either contracted or oversampled by a factor of $n = 16$ (see NMR theory chapter) to give an effective dwell time of 16 microseconds which resulted in smaller spectral widths of $\pm$ 31.25 kHz. That was done to spread out the spectra in order to make it possible to see the temperature dependence of the peak width. The width of the peak was found to increase above the collapse transition suggesting that the distribution of the quadrupole splittings becomes broader as the motions of some segments, possibly near crosslink points, become more constrained, in the collapsed phase.

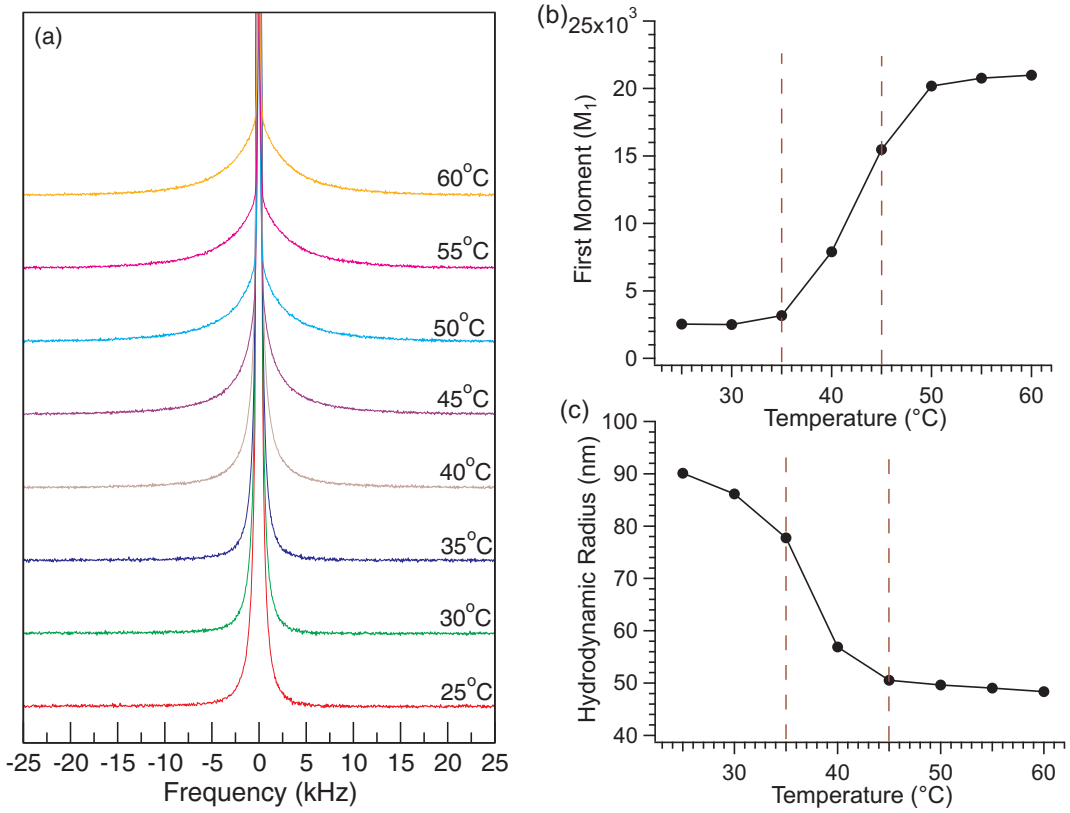

Figure 6.2: a) NMR spectra for the d7 nipam suspension at 5 wt% concentration, as a function of T. The spectra were all collected with the same number of scans, and plotted with their actual absolute spectral areas (no vertical scaling). The central peak widens as temperature increases. b) The first spectral moment as a function of temperature for the spectra in panel a. c) Hydrodynamic radius, as determined by dynamic light scattering (DLS), as a function of temperature for d7 nipam.

In order to get a more quantitative measure of the effect of temperature on spectral width, first spectral moments were calculated. The first moment M_1 (Section 3.5) is the mean half splitting (note that the integral is from zero to infinity) and is proportional to the orientational order parameter S_{CD}, averaged over all the deuterons [52]. Figure 6.2 (b), shows the temperature dependence of the first moment for the d7 nipam suspension at 5 wt%. The increase of M_1 at 35-50°C indicates an increase in segment motional constraint corresponding to the transition from swollen to collapsed phase. This is consistent with the DLS observation for the transition in d7 nipam, shown in Figure 6.2 (c). The DLS observations show that the hydrodynamic radii of the d7 nipam particles decrease with

increasing temperature with the largest change happening in the range of 35-45°C, that is the lower critical solution temperature (LCST) for the polynipam microgel.

It was noted that the NMR signal amplitude per deuteron decreased at the collapse transition. In order to quantify this effect, the total spectral areas for these spectra were found after scaling each spectrum so that all spectra are referenced to the same number of scans. The areas found are shown in Figure 6.3. Spectral area was found to decrease with increasing temperature. This likely reflects the sensitivity of quadrupole echo amplitude for a given segment to the correlation time for its reorientation. Quadrupole echo decay time is typically longer for deuterated segments undergoing very fast reorientation and short for segments undergoing reorientation with correlation times that are comparable to the microsecond timescale characteristic of the deuterium NMR experiments (i.e. intermediate correlation time motions).

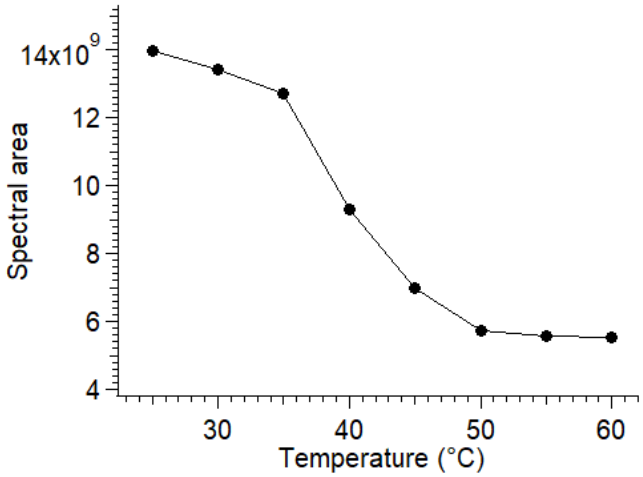

Figure 6.3: Total spectral area, scaled to account for number of scans, *versus* temperature for d7-nipam suspension at 5 wt% concentration.

In order to determine how echo decay rate changed at the collapse transition, quadrupole echo decay measurements were done for the 5 wt% d7 nipam suspension sample at different temperatures. The echo amplitude A was measured at the smallest possible pulse separation, τ=30 μs, and recorded as (A_0), and then measured at higher τ values. The pulse separation

was varied from 30 μs to 1400 μs below the transition, and from 30 μs to 700 μs above the transition. Figures 6.4 (a) and (b) show the echo decay results plotted as $\ln(A/A_0)$ *versus* 2τ at $T = 25°$C and $T = 55°$C, respectively. For spectra that are superpositions of spectral components from segments with different quadrupole splittings, initial echo decay is an average over all deuterated segments while long time decay is dominated by segments with long echo decay time. For populations of deuterated segments with very different motions, the full echo decay can be non-exponential [60].

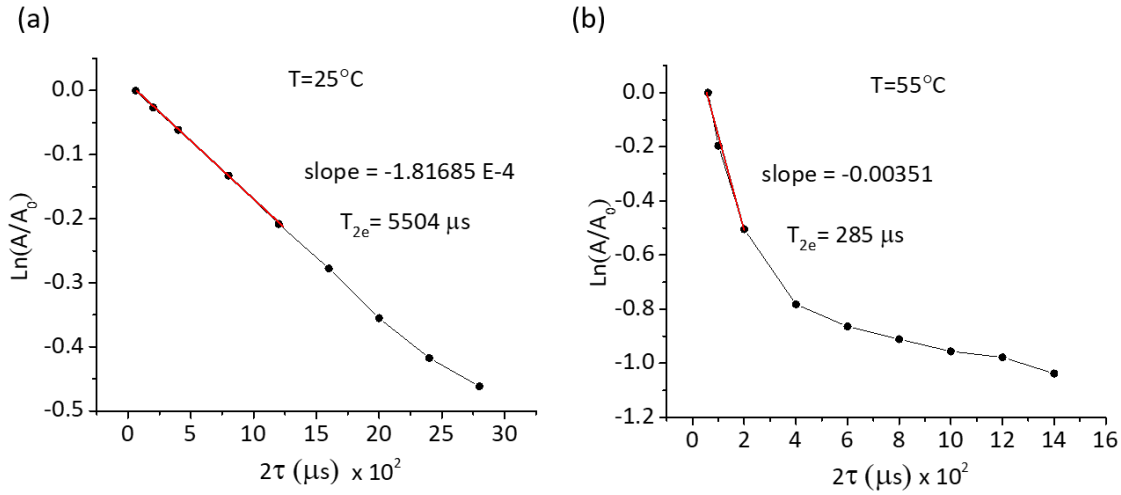

Figure 6.4: Echo decay measurements for the 5 wt% d7 suspension of d7 nipam a) below the transition, at 25°C, and b) above the transition, at 55°C.

In Figure 6.4, the initial echo decays (2τ <400μs) reflect averages of the decay rate over all deuterons. T_{2e} is the inverse of the initial ln (A/A_0) *vs* 2τ slope. Figure 6.5 shows the quadrupole echo decay times T_{2e} as a function of temperature. T_{2e} is much lower above the LCST than below the LCST, presumably due to the slowing of the chain motions that are faster in the swollen phase.

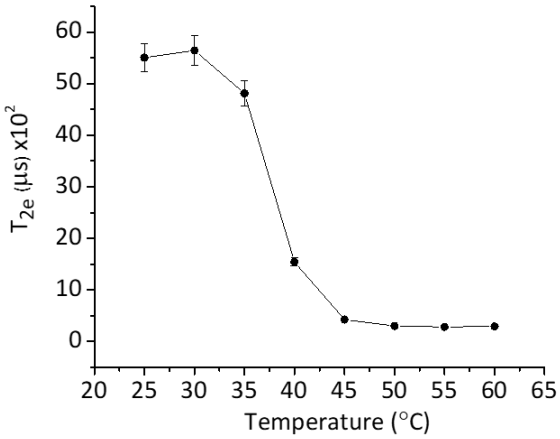

Figure 6.5: Echo decay time as a function of temperature for the 5 wt% suspension of d7 nipam.

This 5 wt% d7 nipam sample did actually demonstrate that it is possible to observe the nipam microgel collapse transition with deuterium NMR and to distinguish the swollen and collapsed phases by line width and echo decay time. The interpretation of the spectrum is complicated by the fact that deuterated segment motions are superposition of backbone motion, sidechain motion, and reorientation about methyl group (for 6 of 7 deuterons). So, the next step was to synthesize material with the backbone deuterated.

6.2 Comparison of dry sample spectra for d7 and d3 polynipam

While the width of the d7 nipam suspension was found to be sensitive to the collapse transition, the motions of the deuterated segments in d7 nipam are superpositions of polymer backbone reorientation, sidechain reorientation, and, for 6 of the d7 deuterons, methyl group rotation. In order to simplify the interpretation of the deuterium NMR observations, polynipam was synthesized using d3 nipam, with 3 deuterons on the segment that is incorporated into the polymer backbone. Figure 6.6 shows the structure of the d3 nipam monomer.

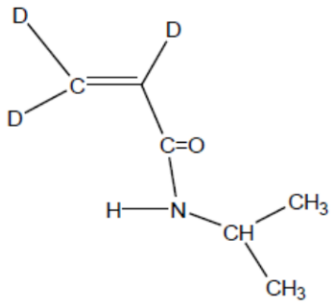

Figure 6.6: The chemical structure of the d3 nipam monomer.

The crosslink density (C_d) for the first polymer synthesized from this d3 nipam monomer was 7.5 wt%. This choice was made in order to compare d7 nipam and d3 nipam polymers when they both have the same C_d. NMR samples were prepared from the dry powders of the d7 and d3 nipam syntheses, respectively. Deuterium NMR spectra were acquired at 25°C for the d7 and d3 dry powder samples by averaging 2000 and 8000 scans, respectively. Both samples contained the same amount, about 9 mg, of the deuterated powders. A higher number of scans were acquired for d3 nipam to enhance the signal to noise ratio, since it has fewer deuterons. In order to obtain the spectral width required to cover the large quadrupole splittings in these spectra, FIDs acquired with a 1μs digitizer dwell time were contracted to obtain an effective dwell time of 4μs. Figure 6.7 shows these two spectra scaled to the number of scans and number of deuterons.

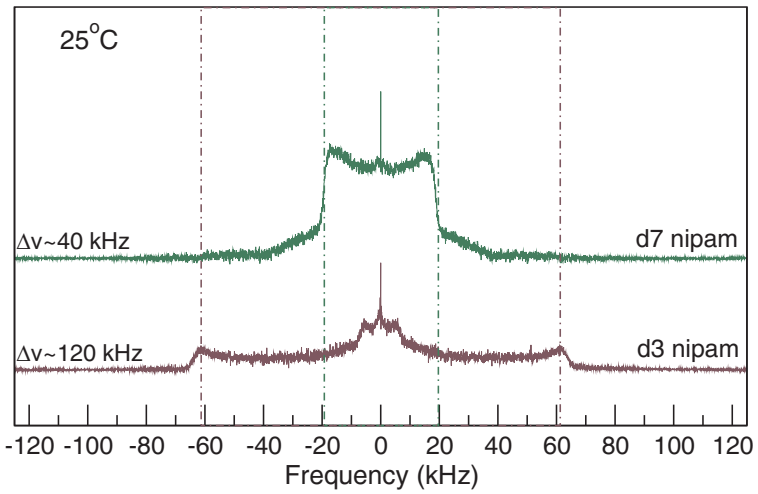

Figure 6.7: The ^{2}H NMR spectra for dry d7 and d3 nipam powders at 25°C. The purple and green dashed lines correspond to the 90° edges for d3 and d7 respectively. The corresponding quadrupolar splitting for the d3 nipam dry sample spectrum was about 120 kHz. This can be interpreted as indicating that the C-D bonds on the back-bone are not free to move. Rotation of methyl groups about the methyl axes in the d7 nipam powder reduces the splitting by about 1/3 relative to d3 nipam, that is to 40 kHz from 120 kHz.

Both the d7 and d3 nipam spectra, shown in Figure 6.7, are Pake powder patterns characteristic of an ensemble of randomly oriented C-D bonds with the prominent edge features arising from segments for which the C-D bond electric field gradient symmetry axes are oriented perpendicular to the magnetic field. As mentioned in Section 3.3, the quadrupolar splitting is measured between the prominent spectral edges corresponding to θ=90° (the angle between the C-D bond and the magnetic field). For randomly oriented static C-D bonds, the maximum quadrupole splitting is ∼125 kHz, which corresponds to edges at ± 62.5 kHz.

The comparison confirms that the deuterons on each sample are on the expected segments. C-D bonds in the d3 sample are completely immobile, except for a small population of more mobile segments that may reflect the presence of small pockets of residual water left after the drying stage of the polymer synthesis. The splitting for the the d3 sample is what is expected for immobile C-D bonds. The spectrum has prominent edges at ±63 kHz, the maximum possible splitting for a Pake doublet arising from C-D bonds. For completely

immobilized segments, the symmetry axes are the C-D bonds themselves. The splitting in d7 is as expected for methyl group rotation about an immobilized methyl group axis. The broad wings in d7 spectrum are part of the Pake doublet. They may be less apparent in the rigid lattice d3 spectrum because they are closer to the spectral width limits. Even though the inner feature in the d3 spectrum, presumed to arise from small wet pockets in the powder, appears to be a non-negligible fraction of the sample, the more mobile material contributing to it may have a longer echo decay time than the methyl deuterons responsible for the bulk of the signal, in d7 nipam.

It is useful to compare the signal (area) per deuteron, per scan for the two samples. During acquisition of the two spectra, 8000 scans were collected for the d3 and 2000 scans were collected for the d7 sample. The number of deuterons per mg was higher (by 7/3) in d7 than in d3, since sample masses were about the same. Taking these factors into account, the total spectral area, scaled to the number of deuterons and scans, was only 40% higher for the d7 than for the d3 sample. This indicates that the signal from a deuteron on the immobile segment on the backbone is not much smaller than that of a deuteron on a reorienting methyl group in the side chains. This suggests that deuterons on immobile polymer backbone segments are not very much less "spectroscopically visible" than those on methyl groups reorienting freely about fixed methyl axes.

6.3 Comparison of spectra for d3 and d7 polynipam suspensions

Suspensions of d3 and d7 nipam polymers, both with the same crosslink density (C_d = 7.5 wt%), were prepared at 20 wt% concentration. Using a higher concentration provided a way to confirm that whole particle rotation was not contributing to narrowing of the observed spectra. Two NMR samples of $\sim$300 μL were made from the d3 and d7 suspensions, respectively.

Figure 6.8 (a) shows NMR spectra for the 20 wt% d3 suspension. These were acquired with 8000 scans and oversampling by 4 at temperatures of 25°C, and 30°C, and with 48000 scans and contraction by 2 at temperatures of 35°C, 40°C, 45°C, 50°C, 55°C, and 60°C. The spectra show significant changes around 35°C, which is consistent with the phase transition inferred from DLS measurements for the d3 nipam sample at 7.5 wt% crosslink density (see Section 5.1.1). The spectra at 35°C and below are narrow peaks indicative of nearly isotropic segment reorientation. That likely reflects nearly free motions of the back-bone in the swollen phase of the hydrated microgel. Above the phase transition, very different behavior was seen. Edges split by about 120 kHz correspond to a strongly split powder pattern component with almost no motional averaging and indicate a fraction of material with nearly immobilized backbone chains. These observations suggest that a fraction of the microgel chains are effectively dehydrated above the transition. The apparent co-existence of rigid and mobile fractions in this sample is consistent with the core-shell model of microgel particles mentioned in Section 1.4. These observations make it possible to estimate the mobile nipam backbone fraction at the studied temperatures. This is discussed below in Section 6.3.2.

Figure 6.8 (b) shows NMR spectra for the 20 wt% d7 suspension. These were acquired with 1000 scans and oversampling by 4 at temperatures of 25°C, 30°C, 35°C, 40°C, 45°C, 50°C, 55°C, and 60°C. The swollen microgel particles give rise to a narrow peak characteristic of isotropic C-D bond reorientation below 35°C. When comparing line widths, it should be noted that the plotted frequency range for Figure 6.8 (a) is 2.5 times wider than for Figure 6.8 (b). Above 35°C, the collapsed microgel particles probably experience more constrained internal conformational motions causing a broadening of the spectral line. The phase transition inferred from the NMR spectra was consistent with the volume phase transition temperature (VPTT) measured by DLS results, that were shown in Figure 6.2 (c).

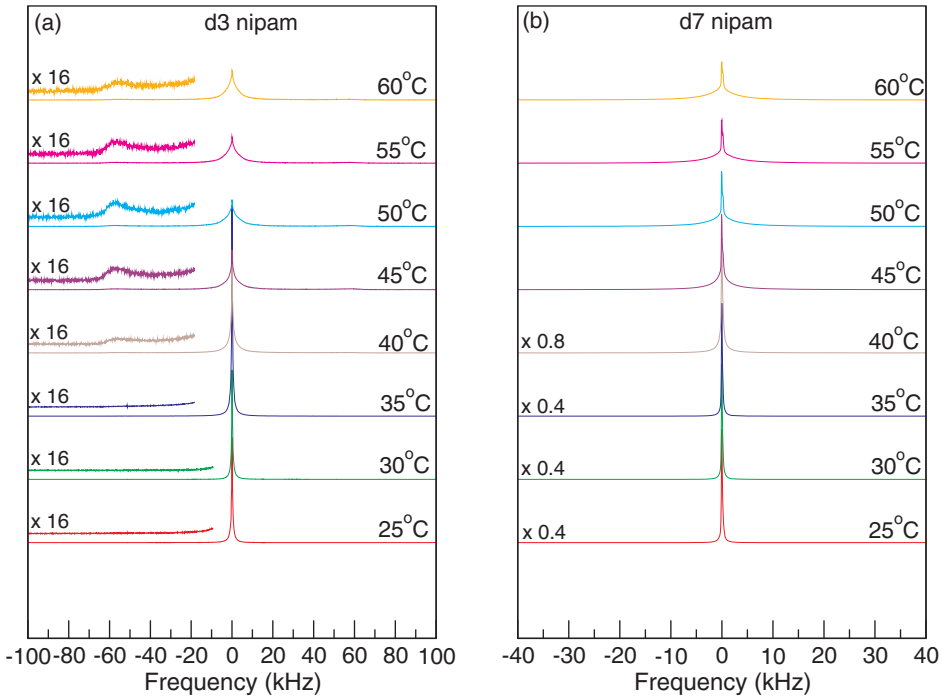

Figure 6.8: Deuterium NMR spectra of (a) the 20 wt% d3 nipam suspension and (b) the 20 wt% d7 nipam suspension, both prepared with a crosslink density of 7.5 wt%. Above the LCST, the d3 sample spectra indicate the existence of a dry fraction of the sample in the collapsed phase. All the spectra in both panels have been normalized so that each integrates to a common spectral area. Enlargements of the left side of the d3 sample spectra are plotted above the wings of each spectrum with a factor of 16 to show the presence of the edges at high temperatures. Above T=35°C, the central peaks are wider, while the spectra are narrow below that of the d7 sample spectra are lower and wider than those at lower temperatures. Unlike the d3 spectra, the d7 spectra do not display any spectral features with larger splitting and can thus be plotted on a smaller frequency range to better display changes in the width of the central feature. Also, the d7 spectra at low temperatures have been scaled down vertically by the factors shown on the spectra.

Both 20 wt% suspensions having a crosslink density of C_d=7.5 wt% show the same transition but the d3 sample also shows, directly, a small spectral component arising from immobile segments. Extra motions in the sidechain and methyl group of d7 sample make it impossible to see any rigid component directly in its spectra even when data acquisition parameters are optimized using experience from the d3 sample. Figures 6.9 (a) and (b) compare spectra of the two samples at 25°C (swollen phase) and 55°C (collapsed phase), respectively.

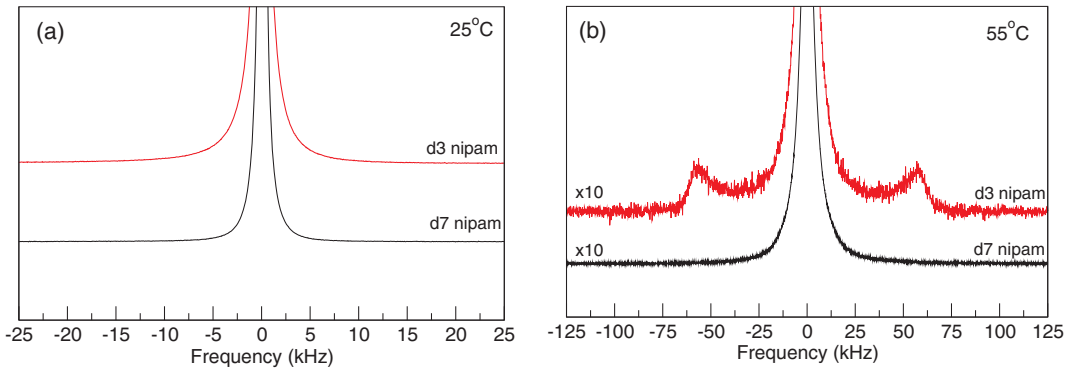

Figure 6.9: Spectra for 20 wt% suspensions of d3 nipam and d7 nipam, both with crosslink densities of 7.5 wt% (a) at 25°C and (b) at 55°C. Spectra have been normalized to the same area after which the spectra at 55°C have been scaled vertically by a factor of 10 relative to the spectra in panel (a), to show the presence and absence, in the d3 and d7 samples respectively, of a spectral component corresponding to immobile segments.

Figure 6.10 shows the first moment as a function of temperature for the spectra of d3 nipam and d7 nipam suspensions shown in Figure 6.8. The temperature dependence of M_1 reflects the phase transition at $\sim$ 35°C in both samples. The decrease in M_1 above 50°C may reflect an increase in the thermal motion at higher temperature. That effect is more apparent in the d3 nipam.

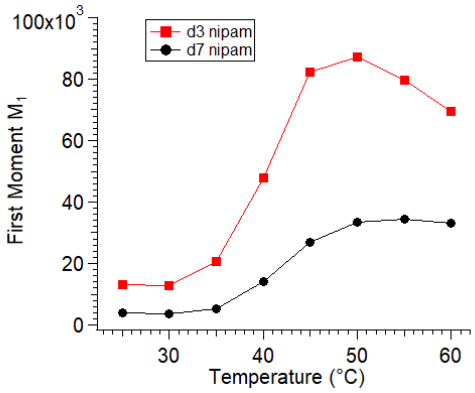

Figure 6.10: First spectral moments as a function of T for the spectra of the 20 wt% d3 and d7 samples with C_d=7.5 wt%.

6.3.1 Quadrupole echo decay measurements for d3 nipam suspension

Quadrupole echo decay measurements were done for the 20 wt% d3 nipam suspension having crosslink density C_d=7.5 wt% below the collapse transition, at 25°C, and above the transition, at 55°C. The initial echo amplitude A_0 was measured for pulse separation τ=30 μs, and then measured for a series of larger τ values. The echo decays, plotted as ln (A/A_0) *versus* 2τ are shown in Figure 6.11 (a) and (b), for temperatures 25°C and 55°C, respectively.

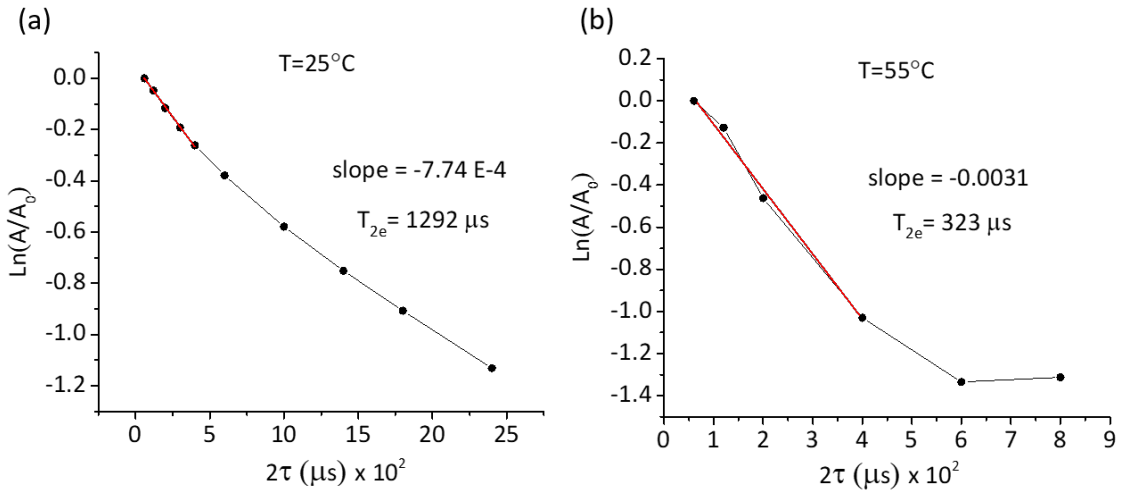

Figure 6.11: Echo decay measurements for the 20 wt% suspension of d3 nipam, having C_d=7.5 wt% a) below the transition, at 25°C and b) above the transition, at 55°C. The slope of ln (A/A_0) *vs* 2τ, with intercept held to zero, represents -1/T_{2e}.

The initial echo decay (2τ <400μs) reflects an average of the decay rate over all deuterons. T_{2e} is the inverse of the initial slope of ln (A/A_0) *vs* 2τ. The echo decay times at the two temperatures are noted in the figure. T_{2e} is much lower at 55°C (above the LCST) than at 25°C (below the LCST), presumably due to the slowing of the chain motions that are faster in the swollen phase.

6.3.2 Spectral area calculations and mobile fraction estimation for d3 nipam suspension

The temperature dependence of the average echo decay time for the d3 suspension indicates a significant change in polymer backbone dynamics at the transition. Segments for which the reorientational correlation time becomes comparable to the spectroscopic timescale could become "spectroscopically invisible" above the transition. In order to test for this possibility, the total spectral areas of the C_d=7.5 wt% d3 nipam suspension spectra were found and scaled to account for differences in number of scans and the oversampling/contraction factors. Figure 6.12 (a) shows these areas as a function of temperature. The signal size is found to decrease with temperature. The drop of the signal coincides with the transition in the d3 nipam suspension.

At 25°C, the integrated intensity of the narrow spectral feature is proportional to the number of deuterons in the sample. Above the LCST, the narrow feature comes from a small population of segments that remain mobile in the collapsed phase. The Pake doublet component with a splitting of about 120 kHz comes from immobilized polymer segments, possibly in the core of the collapsed microgel particles. It is likely that T_{2e} for the small, highly mobile chain fractions remain longer than the pulse separation for all temperatures.

As mentioned in Section 3.7, deuterated segments undergoing slow motions with long correlation times have small echo decay rates ($R\ \alpha\ 1/\tau_c$) and long echo decay times. On the other hand, segments undergoing fast motions with short correlation times also have small echo decay rates ($R\ \alpha\ \tau_c$) and long echo decay times [48, 55].

As long as the narrow spectral components have relatively long echo decay times in both phases, it is possible to estimate the fraction of polymer that remains highly mobile at a given temperature by comparing the integrated intensities of the narrow spectral components at that temperature and at 25°C where effectively all of the chain is highly mobile. In order to carry out such comparisons, integrated intensities must be scaled to account for the numbers

of scans and the spectral width.

To do this, the first step was to find the area (A_{25}) under the 25°C spectrum, which was a narrow peak characteristic of nearly isotropic reorientation. It was assumed that this area represented all of the deuterons in the sample and that they were all on mobile chain segments at this temperature.

The fractions of mobile material in the sample at higher temperatures were then estimated by finding the areas of the central isotropic peaks of the higher temperature spectra (A_T). Taking into account the number of scans and the contraction or oversampling factors for each spectrum, the mobile chain fraction at temperature T were calculated using

$$f_{mobile}(T) = \frac{A_T}{A_{25}}. \tag{6.1}$$

The resulting values of the mobile fractions are shown in Figure 6.12 (b). The mobile fraction decreases with temperature and drops sharply at the collapse transition.

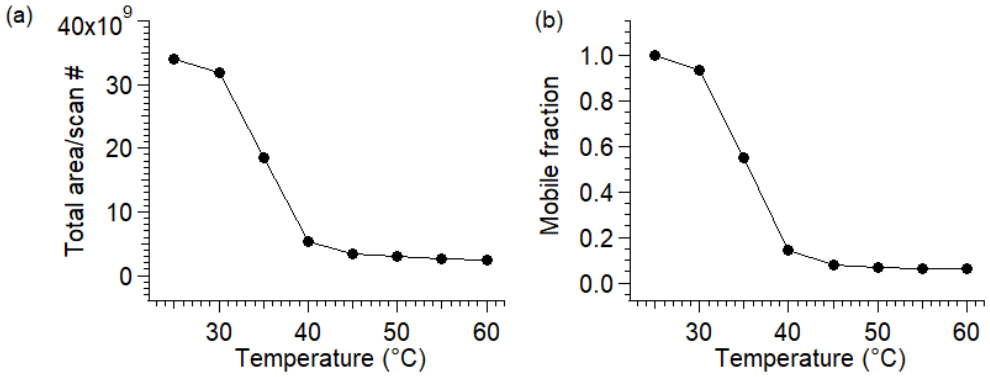

Figure 6.12: a) The total spectral area as a function of temperature for the 20 wt% d3 nipam suspension. b) Dependence of the estimated nipam mobile fraction on temperature.

Figure 6.12 shows that, above the transition, about 5% of the segments that were mobile in the swollen phase are still highly mobile in the collapsed phase. The rest must be undergoing more restricted motion.

In a later experiment on another sample, it was shown that increasing the recovery time between repetitions of the quadrupole echo pulse sequence had no effect on signal amplitude

in the collapsed phase. This confirmed that the loss of the signal in the collapsed phase did not result from the spin-lattice relaxation time (T_1) becoming very long.

Andersson and Maunu [21], using ^{1}H solution NMR, also found that there was a loss of proton NMR signal on going from the swollen to the collapsed phase. For proton NMR, this loss of signal was presumably due to broadening of the solution NMR lines. In the current work, it is segments reorienting with intermediate correlation times that are believed to be lost from the solid-state ^{2}H NMR. This distinction between immobilized segments and segments undergoing intermediate rate reorientation presumably would not be observable by solution NMR.

6.4 Effect of crosslink density

As mentioned at the beginning of this chapter, crosslink density is expected to have an important effect on the properties and the microstructure of microgels. The effect of crosslink density on microgel properties has been studied here by ^{2}H NMR on a series of 20 wt% d3 nipam suspensions synthesized with different crosslink densities. These were selected after practising syntheses with varying crosslinker to monomer ratios and characterizing the resulting polymers by DLS. Among the questions we asked during this work were how does the average core size vary with crosslink density and how does crosslink density affect the collapse transition?

Microgels polymers were synthesized from the d3 nipam monomer with four different C_d values: 1.5; 7.5; 13.6; and 19.5 wt% BIS to monomer. Figure 5.1 (in Section 5.1.1) shows DLS measurements of the particle size as a function of temperature. It is found that the transition temperatures for these microgels are all close to 35°C and are only weakly dependent on the crosslink density C_d. The biggest change of particle size at the transition is found for the smallest C_d. The swelling factor, defined as the ratio of microgel particle volume below the collapse transition to that above the transition, was thus the largest

for the smallest crosslink density studied. Suspensions were prepared from these polymer powders and deuterium-depleted water, all at 20 wt% concentration. Samples made from these suspensions were used to obtain deuterium NMR spectra for a series of temperatures, at ambient pressure, using the 9.4 T NMR spectrometer. The spectra for the sample with a crosslink density of 7.5 wt% are those already presented in the previous Section. The collected NMR spectra at selected temperatures for the four differently crosslinked microgel suspensions are shown in Figure 6.13. Vertically scaled enlargements of the spectral edges on the left side of the spectra are plotted above the left side of each spectrum. The spectra in Figure 6.13 are normalized so that each integrates to a common spectral area.

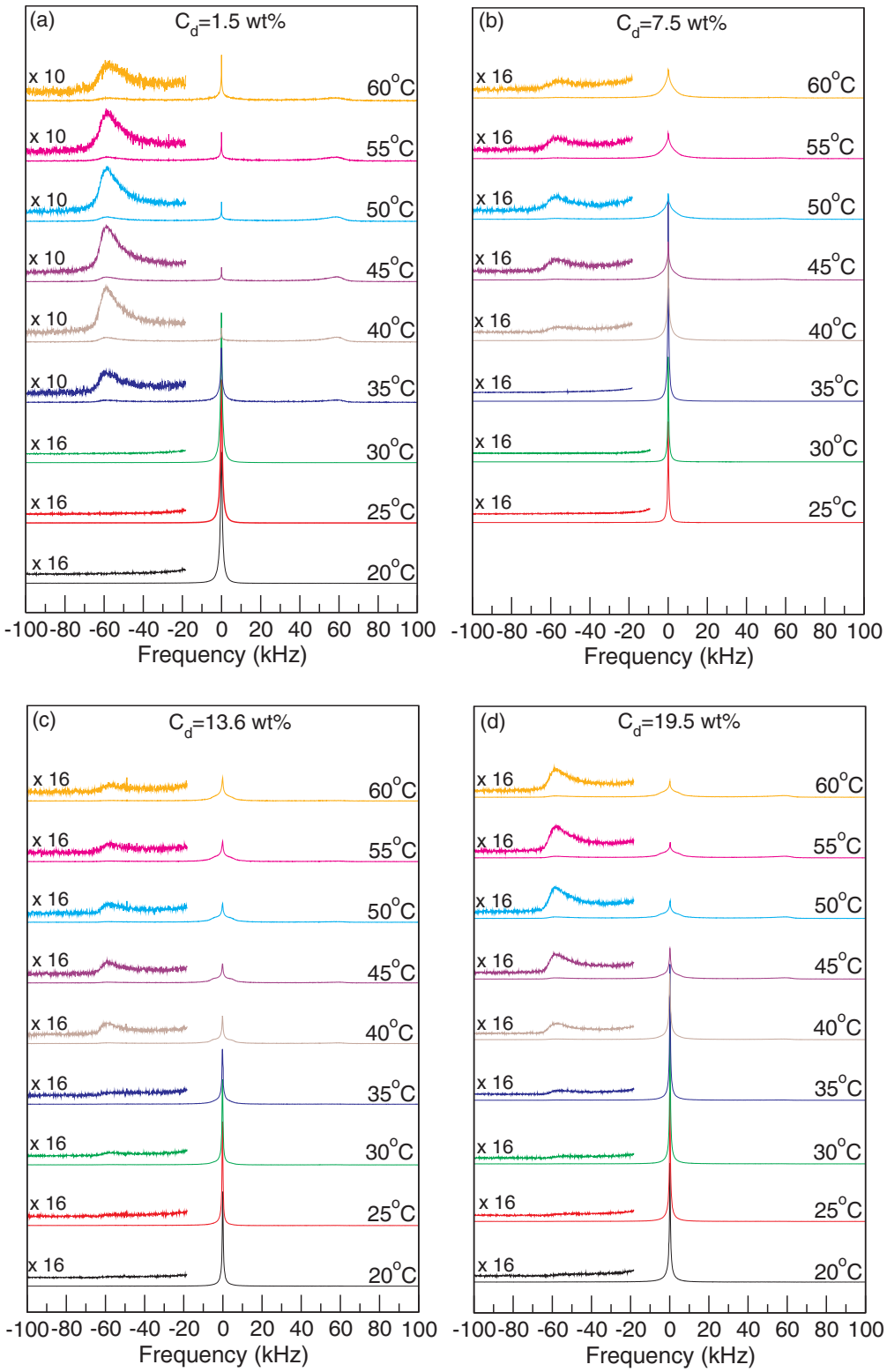

Figure 6.13: Deuterium NMR spectra for 20 wt% suspensions of d3 nipam prepared with crosslink densities (BIS/monomer) of (a) C_d=1.5 wt%, (b) C_d=7.5 wt%, (c) C_d=13.6 wt%, and (d) C_d=19.5 wt% BIS/monomer. Spectral areas are normalized.

Inspection of Figure 6.13 (a) shows that for the d3 nipam microgel sample with the lowest crosslink density, C_d=1.5 wt%, the spectrum at low temperature is an intense, narrow, central peak. The observation of a single narrow line indicates fast nearly isotropic reorientation of all of the C-D bonds in the sample and is consistent with effectively free reorientation of most of the polymer chains in the swollen sample phases. At 35°C the volume phase transition (VPT) occurs and the microgel particle undergoes a transition from the swollen phase to the collapsed phase in which water is squeezed out and the hydrophobic groups collapse on themselves forming a more compact particle in which chain reorientation is more constrained. The doublet with a quadrupole splitting of ∼120 kHz indicates that a fraction of the segments form a dense core with a more rigid structure. The completely immobile C-D bonds in the core give an NMR spectrum that is a Pake doublet with the maximum splitting of ∼120 kHz. The small central peak, with lower intensity than in the swollen phase, indicates that a small fraction of the segments in particle are still freely moving in the collapsed phase. As will be discussed below, a significant fraction of segments in the collapsed phase particle may be reorienting at intermediate rates that, in effect, make them spectroscopically invisible. From 35°C to 50°C, the intensity of the central peak component decreases while the intensity of the rigid component increases indicating that the fraction of the microgel particle in the immobile core is increasing. Above 50°C, the intensity of the central peak component recovers slightly while the intensity of the rigid segment spectral component decreases. This is interpreted as being the result of competition, between thermal energy and the hydrophobic interaction, that results in increased amplitude of segment reorientation in the collapsed phase at high temperature.

Figure 6.13 (b) shows spectra of the 20 wt% suspension of d3 nipam microgel with a crosslink density C_d=7.5 wt%. From 25°C to 35°C, the spectrum is again a narrow peak. At 40°C the central peak widens and the large splitting doublet component appears. The central peak continues to get wider and lower and the immobilized segment spectral component becomes more prominent until 50°C. Above 50°C, thermal energy increases the amplitude

of motion in the rigid fractions of the microgel particles and the intensity in the doublet feature decreases slightly.

Spectra for the 20 wt% d3 nipam microgel suspension with C_d=13.6 wt%, are shown in Figure 6.13 (c). The rigid segment spectral component exists even in the swollen phase indicating that a small fraction of the microgel segments are forming a rigid core even in the swollen phase. At the transition, the core grows and the central peak corresponding to nearly isotropic reorientation broadens and decreases in amplitude.

Spectra for the 20 wt% suspension of d3 nipam microgel with a crosslink density of 19.5 wt%, are shown in Figure 6.13 d. These spectra show same behavior as the 13.6 wt% BIS sample but with a higher fraction of the polymer immobilized in the cores of the microgel particles.

In order to focus on the effect of crosslink density above and below the transition, normalized spectra for the four crosslink densities were plotted together for T=25°C (below the transition), T=40°C (just above the transition), and at T=55°C (well above the transition). These comparisons are shown in Figure 6.14.

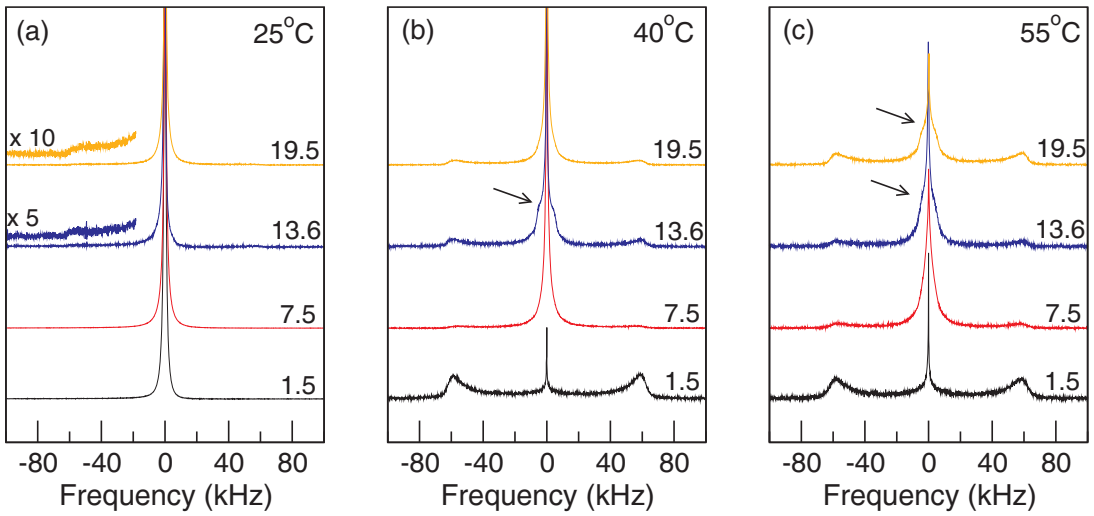

Figure 6.14: The effect of the crosslink density of the microgel suspensions on the spectral shape (a) below the transition at T=25°C, (b) just above the transition at T=40°C, and (c) way above the transition at T=55°C. The crosslink density as the crosslinker/monomer (wt%) ratio is noted at the right above each Spectrum. Spectral areas are normalized. Vertically scaled enlargements of the spectral edges on the left side of the spectra are plotted above the left side of selected spectra.

Comparison of the spectra in Figure 6.14 (a) shows that below the transition, the spectrum is dominated by a narrow line characteristic of fast, nearly isotropic reorientation for all four crosslink densities. As has been noted, though, the spectra for the two highest crosslink densities also have a small doublet component with the maximum possible quadrupole splitting for a C-D bond. This indicates that at higher crosslink densities, a small fraction of the segments are immobilized, presumably in the particle core.

Comparison of Figure 6.14 (a) with Figure 6.14 (b) shows that from 25°C to 40°C, which is just above the transition midpoint, the spectrum for the lowest crosslink density, C_d=1.5 wt%, changes dramatically. The narrow spectral component nearly disappears and the spectrum is dominated by the doublet corresponding to effectively immobilized segments. It should be noted that spectra in Figure 6.14 are normalized to a constant area and that the actual signal per deuteron for the C_d=1.5 wt% spectrum decreases significantly from 25°C to 40°C. The signals for the higher crosslink density samples also decrease form 25°C to 40°C but the change in spectral shape is more gradual. For the two highest crosslink densities, the size of the immobilized segment spectral component, relative to the narrow component, increases. For C_d=7.5 wt%, an immobilized segment spectral component appears. For C_d=13.6 wt%, the narrow spectral component also develops shoulders suggestive of a Pake doublet with a quadrupole splitting of 8-10 kHz. This may indicate that the reorientation of some of the more mobile segments is becoming slightly less isotropic on the deuterium NMR timescale ($\sim 10^{-5}$ s).

Figure 6.14 (c) shows spectra for the four crosslink densities at 55°C, well above the transition. From 40°C to 55°C, the spectrum for a given crosslink density changes only slightly. For all four crosslink densities, the spectral component corresponding to an immobilized fraction is significant. For the two highest crosslink densities, the development of shoulders on the narrow spectral component is more apparent. As will be discussed in more detail below, however, the most significant change with temperature is the loss of signal as each sample is warmed through the transition.

For all of the crosslink densities studied, the spectrum below the transition is dominated by a central line. Even though there is no detectable splitting, the width of this line at half maximum is a few kHz, and thus non-negligible, even in the swollen phase. As the sample is warmed into the collapsed phase, the width of the central line increases as its area decreases. This raises some important questions about the segment motions corresponding to the central line. One question is whether the absence of an apparent splitting reflects isotropic reorientation by all of the mobile segments or whether the central line is a superposition of narrow doublet components corresponding to a continuous distribution of large amplitude but slightly anisotropic reorientation about local symmetry axes. One argument against the suggestion of a single, homogeneous central line is that points where chains are linked by crosslinkers are presumably less mobile than polymer segments that are not close to a crosslinker. The idea that there are points along a given chain that are more motionally constrained due to crosslink interactions may also provide a way to think about the symmetry axes for segment reorientation in the swollen phase. A length of polymer chain between two crosslink points may be longer than the direct distance between the two crosslinks. The segments on that length of chain may be able to reorient with a large amplitude but the effective tethering of that length of chain at either end will impose some anisotropy on the reorientation. The segments closest to the crosslinks will be the most constrained and thus the most orientationally ordered. The result will be a distribution of segment orientational orders ranging continuously from non-zero order, for the segments closest to the crosslink points, to nearly zero orientational order for segments midway between the crosslink points. It was found that narrow lines like those observed in the collapsed phase could be approximated by superpositions of Pake doublets with splittings distributed continuously from zero to larger widths if the distribution was weighted toward smaller splittings. An example figure showing simulated spectra obtained using a superposition of Pake doublets with a distribution of order parameters is shown in Appendix B.

All the spectra in Figure 6.13 were normalized to a fixed spectral area. In order to relate

the observed spectra to the morphology of the microgel particles, particularly in the collapsed phase, it is important to know if a fraction of the polymer segments are reorienting at intermediate rates for which the quadrupole echo decay time is very short. In spectra obtained using the quadrupole echo sequence, segments in this population may be underestimated or even unobservable. Figure 6.15 shows unnormalized (actual intensity) versions of spectra initially shown in Figure 6.13 (a), that were obtained from the suspension of d3 nipam microgel with C_d=1.5 wt% at all temperatures. These spectra have first been scaled so that their amplitudes are what they would have been if all spectra had been collected with the same number of scans. After the spectra at temperatures above the collapse transition have been magnified vertically by the factors shown near the spectral centres, the left portions of each spectrum have been further magnified, by the scaling factors shown to the left, to make any immobile fraction spectral components visible. For example, after scaling to account for differences in the number of scans used to acquire it, the whole spectrum at 60°C has been scaled by a factor of 50 and the left portion of the spectrum has been scaled by a further factor of 10 (for a total factor of 500) to make lineshape features visible. From comparing the spectra in Figure 6.15, it is apparent that the total spectral area decreases significantly at the collapse transition of this sample.

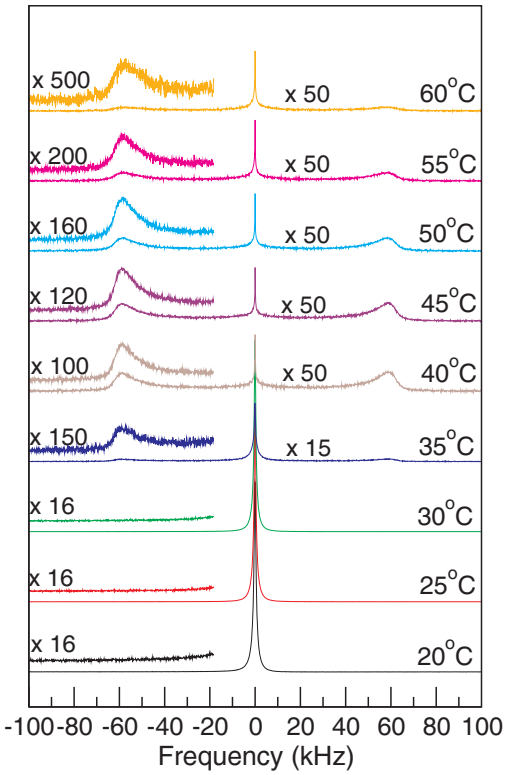

Figure 6.15: Unnormalized spectra for the 20 wt% suspension of d3 nipam microgel with crosslink density C_d=1.5 wt%. Spectra have first been scaled so the amplitudes correspond to the same number of scans. Spectra for 35°C to 60°C and the left portions of each spectrum have been further magnified vertically by the factors shown in the figure.

6.5 Spectral areas and particle structure

As mentioned in Chapter 3, slow motions with long correlation times have small echo decay rates ($R \; \alpha \; 1/\tau_c$) and long echo decay times. On the other hand, fast motions with short correlation times also have small echo decay rates ($R \; \alpha \; \tau_c$) and long echo decay times [48,55]. Intermediate motions with characteristic times in the range of the NMR experiment time scale can change the orientation of the average electric field gradient and thus the quadrupole interaction before the dephasing magnetization can be refocused by the second pulse. Segment reorientation with such intermediate correlation times may give rise to a very short quadrupole echo decay time. Quadrupole echo decay time *versus* reorientational correlation time can thus display a minimum [61]. It has been shown above that the quadrupole echo

decay time for the narrow spectral component in the swollen phase is long relative to the pulse separations used here. The echo decay time of the Pake doublet component arising from immobilized segments is shorter but still long enough that the amount of microgel in a rigid segment environment is likely not underestimated by more than a factor of two. The substantial decrease in signal intensity at the collapse transition may thus reflect the onset of intermediate rate reorientation for a significant fraction of the microgel chains.

The integrated intensities of all the spectra collected at ambient pressure, for the 20 wt% suspensions of microgel synthesized with the four crosslink densities, were calculated and scaled to account for the difference in the monomer absolute mass in the sample, and for differences in the number of scans. This was done to eliminate any factors that affect the absolute ratio of the NMR signal to the number of C-D bonds that exist in each sample. Figure 6.16 shows the resulting plot of area per scan per unit sample amount *versus* temperature for the four d3 microgel suspensions. The highest signal detected corresponds to the lowest temperature and the lowest crosslink density. The signal decreases with increasing crosslink density and with increasing temperature. A significant fraction of the signal disappears when a given microgel suspension goes from the swollen to the collapsed phase with increasing temperature. This transition happens at $\sim$35°C for all four samples. This is consistent with the DLS observations for the particle VPT transition for these four differently crosslinked microgels.

The immobile fraction segments at high T in the microgel suspension are more mobile than those in the dry samples. However, the near absence of signal intensity at high T for the microgel suspensions is an indication that a large fraction of C-D bonds are reorienting at an intermediate rate. This is an indication that a large fraction of segments in the collapsed phase retain some mobility which suggests that particles in this phase contain a significant amount of water for all of the crosslink densities studied. This finding from NMR is consistent with our rheological characterization from which the water volume fraction in the microgel particle in the collapsed phase was found to be $\sim$60% for all the four studied

crosslink densities, see Section 5.2.4.

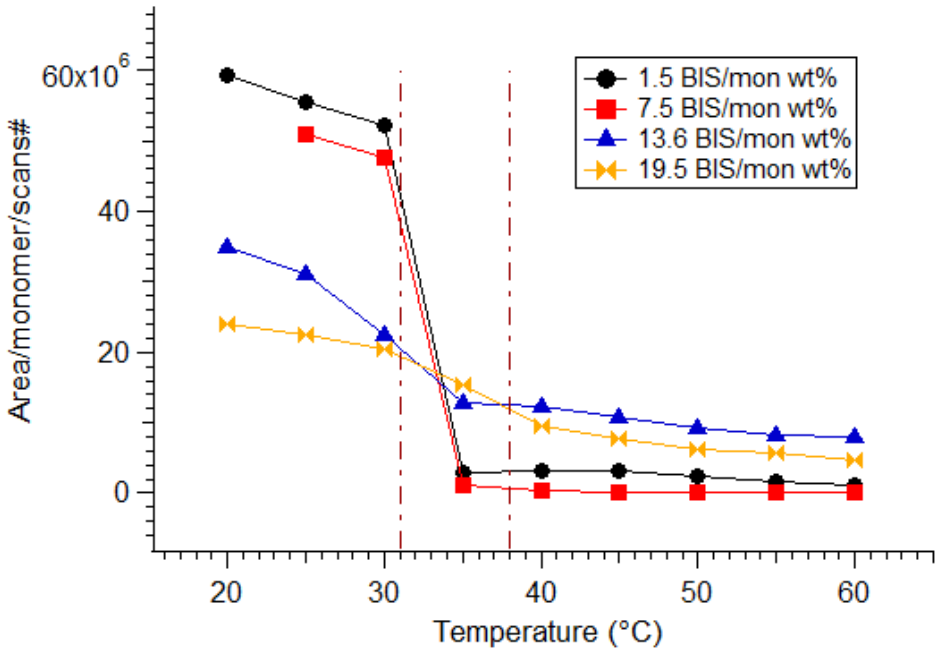

Figure 6.16: Temperature dependence of spectral area, scaled to account for differences in sample size (monomer absolute mass) and number of scans, for 20 wt% suspensions of d3 nipam microgel with crosslink densities of (circle) C_d=1.5 wt% BIS/monomer, (square) C_d=7.5 wt% BIS/monomer, (triangle) C_d=13.6 wt% BIS/monomer, and (bowtie) C_d=19.5 wt% BIS/monomer.

One of the most important findings here is that the change in spectral area at the transition is larger and sharper for small crosslink densities than for larger crosslink densities. This finding from NMR is consistent with our DLS characterization from which the biggest change in the microgel particle volume was found to be happening at the lowest crosslink density, C_d=1.5 wt% here (see Section 5.1.1). This suggests that increasing crosslink density results in slightly more compact microgel particles in the swollen phase but also interferes with complete collapse above the transition. Also, the smaller change in signal intensity at the transition for the highest two crosslink densities suggests that more of the segments are spectroscopically visible in the collapsed phase of the more highly crosslinked samples. Thus segments in the more highly crosslinked microgels, in the collapsed phase, are either undergoing fast free reorientation (narrow central peak), or fast constrained "axially sym-

metric" reorientation (∼20 kHz doublet), or are immobile forming the small dense core. The spectroscopically invisible fraction of the intermediate rate motion is not a large fraction for a highly crosslinked microgel.

6.6 Variable pressure ^{2}H NMR study of microgels and $P-T$ diagram mapping

For soft materials that undergo transitions involving volume changes, pressure can be an interesting variable. Pressure has been used as a variable in studies for other soft materials like phospholipids [64]. Deuterium NMR studies on phospholipid bilayer systems, a well-studied soft matter system, have shown that applying high pressure reduces area per lipid, so chains become more orientationally ordered. This increases quadrupolar splitting for a given temperature, compared to ambient pressure [64, 67]. Pressure also raises the main transition temperature of phospholipid bilayers and can induce transitions to ordered phases that are not accessible at ambient pressure [59].

The pressure-temperature ($P-T$) diagram for polynipam microgels was studied by Kunugi *et al.* [32] by measuring the cloud point in aqueous solutions using DLS at elevated pressures and subzero temperatures. The $P-T$ diagram showed that near or at atmospheric pressure, the transition temperature increased with increasing pressure but decreased with increasing pressure at pressures higher than 150 MPa. They also showed that the $P-T$ diagram can be fitted to a part of an ellipsoid curve in the temperature range from ~0°C to 40°C, and in the pressure range from 0.1 MPa to 300 MPa. They found two apparent regions on the transition line at which $\Delta P/\Delta T > 0$ and thus $\Delta S > 0$ (see Clausius-Clapeyron equation (1.3)). An increase in entropy at these two points, corresponded to two cases of phase transitions from the collapsed phase to the swollen phase: either a transition by increasing pressure up to ~50 MPa and around 35°C, or a transition by increasing temperature near 0°C and at elevated pressures.

Lietor-Santos *et al.* showed that increasing the external hydrostatic pressure to ~350 MPa near room temperature induces a volume phase transition in polynipam microgels from a coil (mixed) or swollen phase to a globule (unmixed) or collapsed phase [5]. They attributed this result to the increase in the Flory mixing parameter (see equations (1.1) and (1.2)) of

the polynipam microgel with the solvent, causing a swollen to collapsed phase transition.

Understanding how pressure affects the microgel swelling behavior could be relevant to technological applications, as mentioned in Chapter 1. We are aiming to answer questions that are not answered yet like whether the microgel internal structure in the collapsed phase after a pressure induced phase transition is the same as that after a temperature induced phase transition? The same question applies to the swollen phase at different pressures.

To investigate the phase behavior and microgel properties at higher pressures, variable pressure deuterium NMR was used to examine the effect of applying pressure to 20 wt% suspensions of d3 nipam microgel synthesized with the same crosslink densities as the samples used for ambient pressure experiments. It must be noted that, as mentioned earlier in this chapter, the variable-pressure probe operates at a lower magnetic field in the 3.5 T spectrometer and has a smaller sample size than the ambient pressure probe used at 9.4 T. Both factors reduce available signal. The variable pressure NMR system is described in Section 4.3.5.

Variable pressure NMR was first used to study the effect of pressure on the phase behavior for d3 nipam microgel with crosslink density C_d=7.5 wt%. This sample was prepared as a 20 wt% suspension in deuterium-depleted water. In making a sample for the variable-pressure probe in the 3.5 T spectrometer, an effort was made to contain the largest possible amount of material that can fit into the limited space of the variable-pressure probe in a container sufficiently flexible to be able to transmit high pressure to the sample without rupturing. For the initial variable pressure studies, $\sim$150 μL of suspension was heat-sealed into a polyethylene capsule similar to ones used for previous variable pressure studies with this probe [67].

For the 3.5 T NMR spectrometer, FIDs were collected with a digitizer dwell time of 2 μs and an FID file length of 2048 points. ^{2}H NMR spectra for the C_d=7.5% microgel suspension were first acquired at ambient pressure for a series of temperatures in order to compare them with the spectra collected for the similar sample on the 9.4 T system. Because of the smaller

sample size (less deuterons) and the lower field, signal to noise ratio (s/n) was much lower. At temperatures above the transition, large numbers of scans (about 200,000 scans) were needed to get a signal from the C_d=7.5 wt% sample using the variable-pressure NMR probe. Even with the large number of scans in the collapsed phase, the large splitting doublet spectral component characteristic of immobile segments in the sample was not detected above a background signal that was presumed to arise from materials used in constructing the variable-pressure probe.

Some steps were taken to optimize sensitivity to a broad weak spectral component. To minimize loss of signal due to echo decay, the pulse separation was set to the lowest possible length, which is 30 μs. The recovery time between scans was increased from 0.9 s to 4.0 s to determine whether the weak signal from the rigid segment fraction might be due to that spectral component having a long T_1 (spin-lattice relaxation time) which would result in a long time being needed for the magnetization to relax back to equilibrium. That experiment resulted in the same signal as was seen for the shorter recovery time. This was an indication that no signal was lost due to spin-lattice relaxation effects. In later experiments, the approach taken to increase signal was to design a thinner walled capsule capable of holding a slightly larger sample.

In the variable-pressure probe, spectra for the C_d=7.5 wt% d3 nipam microgel suspension in the original polyethylene capsule displayed high intensity narrow peaks in the swollen phase, and almost no central peak in the collapsed phase. Spectra for this sample were collected for a series of temperatures from 25°C to 60°C at ambient pressure and at higher pressures in order to map the pressure-temperature phase diagram and the phase transition line. For a given series of spectra, the transition was identified by an abrupt change in signal intensity or in signal/noise ratio. The spectral areas of the central peak, scaled to the number of scans, span a wide range. For the purpose of mapping out a pressure-temperature phase diagram, spectral area was used to classify spectra as corresponding to the microgel being completely swollen (black circles), semi-swollen (blue squares), semi-collapsed (orange

triangles), and completely collapsed (red diamond). The resulting pressure-temperature phase diagram for the 20 wt% suspension of d3 nipam microgel with C_d=7.5 wt% is shown in Figure 6.17. Examples of spectra in the swollen and in the collapsed phases are plotted to the left and right of the $P-T$ diagram, respectively. These two spectra are plotted on the same vertical scale but the spectrum from the collapsed phase has been scaled by a factor of 0.2 to account for the fact that it was acquired using five times as many scans as the spectrum in the swollen phase. Comparison of the two spectra in Figure 6.17 thus shows the large change in spectral intensity from the swollen to the collapsed phase.

The transition line in the phase diagram of Figure 6.17 is drawn through pressure temperature points corresponding to spectra in which the intensity is decreasing toward the small value identified with the collapsed phase. The slope of the transition line increases with increasing temperature and appears to be approaching a maximum temperature with increasing pressure.

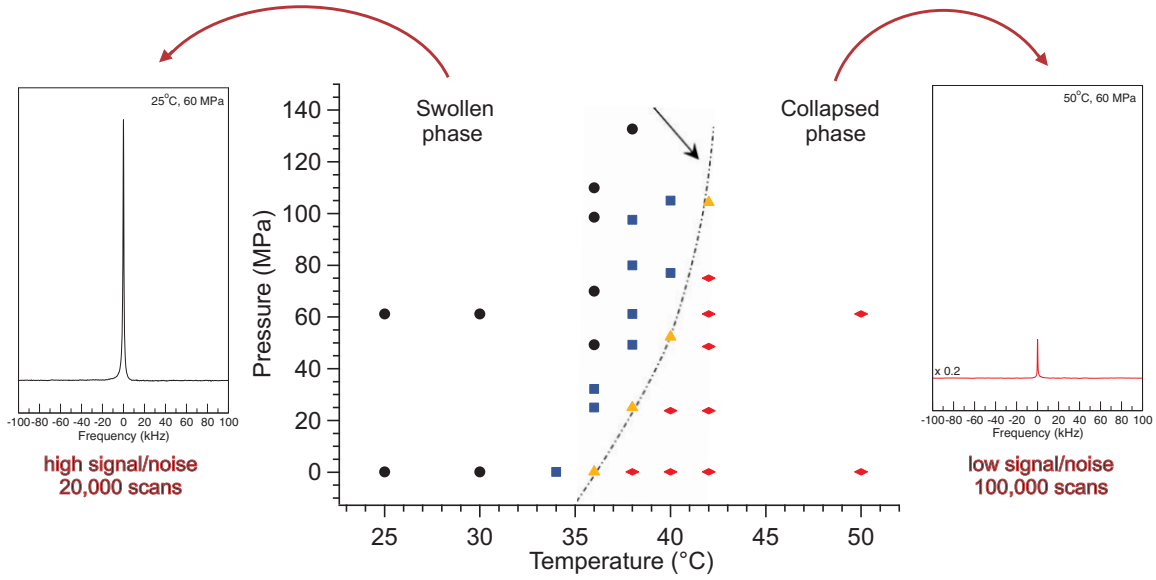

Figure 6.17: Centre panel: The pressure-temperature phase diagram for the 20 wt% suspension of d3 nipam microgel with crosslink density C_d=7.5 wt%, based on spectral area measurements. Four regions are identified based on areas: completely swollen (black circles), semi-swollen (blue squares), semi-collapsed (orange triangles), and completely collapsed (red diamond). The transition line (dark purple), is drawn through the points identified as semi-collapsed. Examples of spectra in the swollen and collapsed phases are shown to the left and right of the diagram, respectively. The spectra are plotted on the same scale. The spectrum corresponding to the collapsed phase has been scaled by a factor of 0.2 to account for its having been acquired using five times the number of scans used for the swollen phase spectrum.

Additional experiments were carried out using sample containers made by using pouches made of Saran Wrap polyethylene film (Glad) sealed by dental floss ties. The first sample prepared in this way was again a 20 wt% suspension of d3 nipam microgel synthesized with a crosslink density C_d=7.5 wt% BIS/monomer. The amount of material in this sample was twice that for previously-described experiment (done using a heat-sealed capsule) and the signal-to-noise ratio was improved. The pressure-temperature behaviors for the two C_d=7.5 wt% samples prepared using the two encapsulation methods were consistent. Because of the improved signal-to-noise ratio, Saran Wrap pouches were used to contain samples for all subsequent experiments involving the variable-pressure NMR probe. These were variable pressure studies for 20 wt% suspensions of the d3 nipam microgels prepared with crosslink

densities C_d=1.5 wt%, C_d=13.6 wt%, and C_d=19.5 wt%.

For suspensions of microgel with each of the crosslink densities, two sets of experiments were carried out using the variable-pressure probe in the 3.5 T spectrometer system. The first set consisted of fixed pressure (isobaric) temperature series at ambient pressure and at 8,800 psi (∼60 MPa). That was done to see the effect of pressure on the temperature of the collapse transition. The second set of experiments was used to fill in points around the transition in the pressure-temperature phase diagram curve, by collecting spectra at 4-5 temperatures around the transition temperature for each microgel at two pressures: 4,400 psi (∼30 MPa) and 13,100 psi (∼90 MPa). For all of the four crosslink densities studied, the transition temperature increased with increasing pressure. The smallest increase in the transition temperature with increasing pressure was seen for the sample with the lowest crosslink density, $C_d = 1.5$ wt%. Examples of the variable pressure spectra that were collected for the $C_d = 1.5$ wt% sample are shown in Figure 6.18. The ambient pressure, 30 MPa, 60 MPa, and 90 MPa sets of spectra are plotted for series of temperatures in four panels (a, b, c, d), respectively. These spectra were scaled to account for differences in the number of scans and then plotted on the same scale, without further normalization so that one can clearly see the difference in the spectral shape and intensity through the transition. The sudden drop of the central peak height reflects the phase transition. The transition temperature increases by about 5 degrees from ambient pressure to 90 MPa.

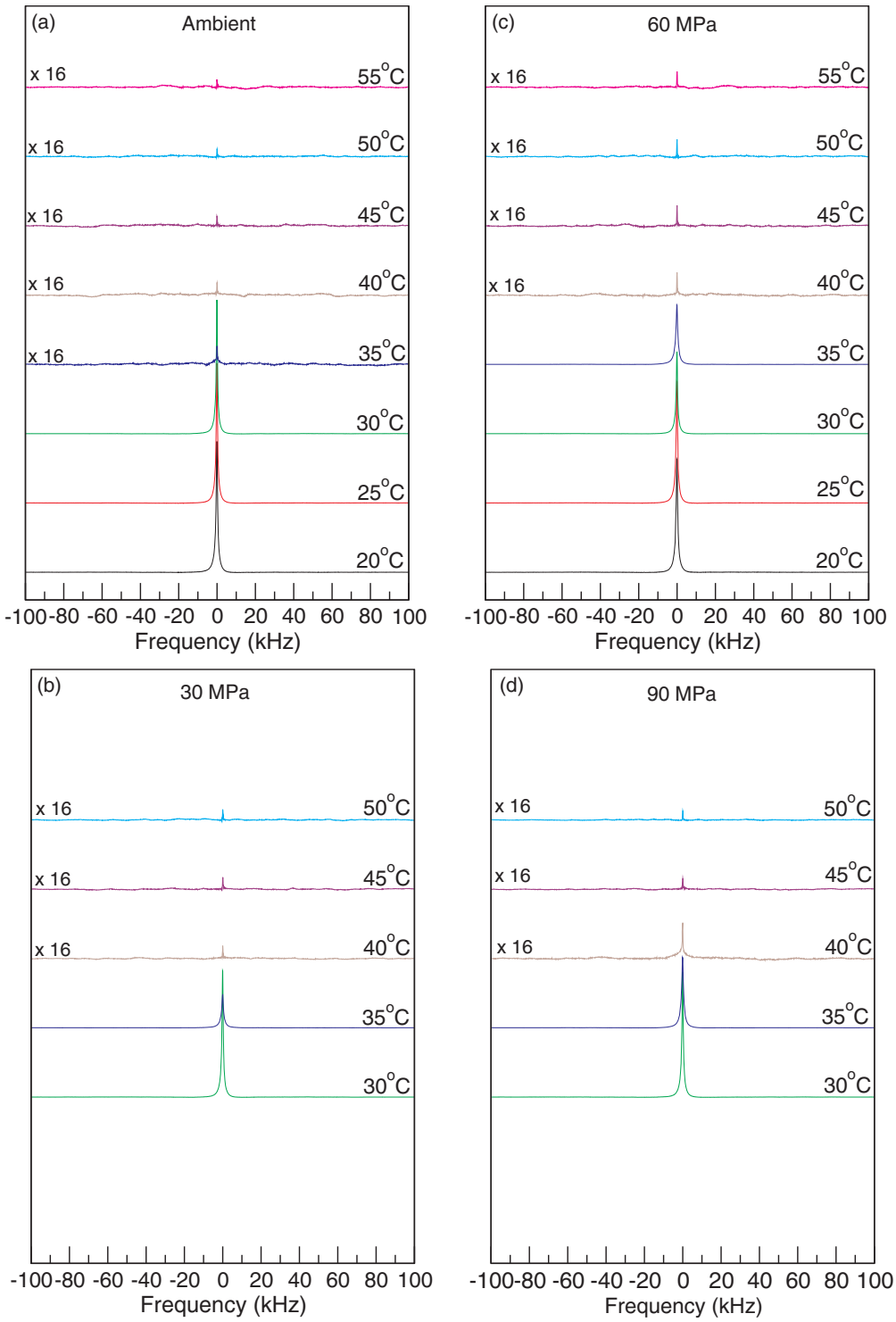

Figure 6.18: Deuterium NMR spectra, collected over a series of temperatures, for a 20 wt% suspension of d3 nipam microgel with a crosslink density C_d=1.5 wt% BIS/monomer at (a) ambient pressure, (b) 30 MPa, (c) 60 MPa, and (d) 90 MPa. Unnormalized spectra were scaled to account for differences in the numbers of scans acquired and then plotted on the same vertical scale.

For the C_d=1.5 wt% sample, the total spectral areas of the unnormalized spectra in Figure 6.18 were measured and scaled to account for differences in the numbers of scans. Figure 6.19 shows the resulting plot of spectral areas as a function of temperature at different pressures. This plot shows that the transition happens at 35°C for ambient pressure and at higher temperatures for higher pressures.

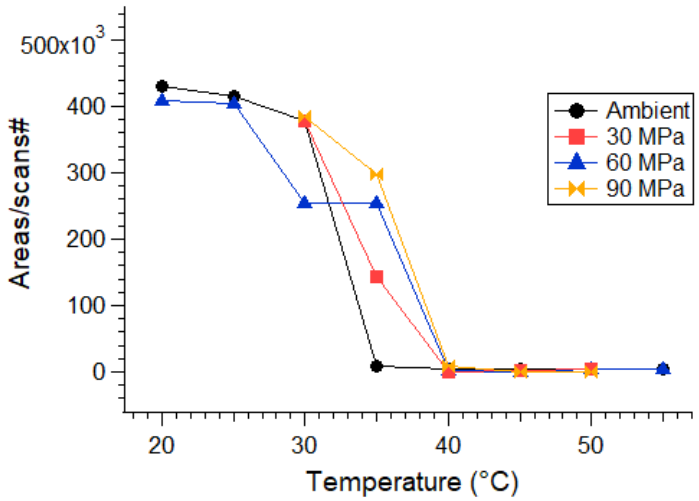

Figure 6.19: Spectral area, scaled to account for differences in the number of scans, *versus* temperature at (circle) ambient pressure, (square) 30 MPa, (triangle) 60 MPa, and (bowtie) 90 MPa for a 20 wt% suspension of d3 nipam microgel with a crosslink density C_d=1.5 wt%.

In addition to the sets of spectra shown in Figure 6.18 for the lowest C_d, sets of spectra at different pressures and temperatures were collected for each of the three remaining crosslink densities as mentioned above. Based on the spectral shape and intensity, the spectrum for each pressure-temperature point was classified as corresponding to a swollen, semi-swollen, or collapsed microgel state. The pressure-temperature phase diagrams for the microgels with C_d= 1.5 wt%, C_d=7.5 wt%, C_d=13.6 wt%, and C_d=19.5 wt% are plotted in Figure 6.20 (a, b, c, d), respectively.

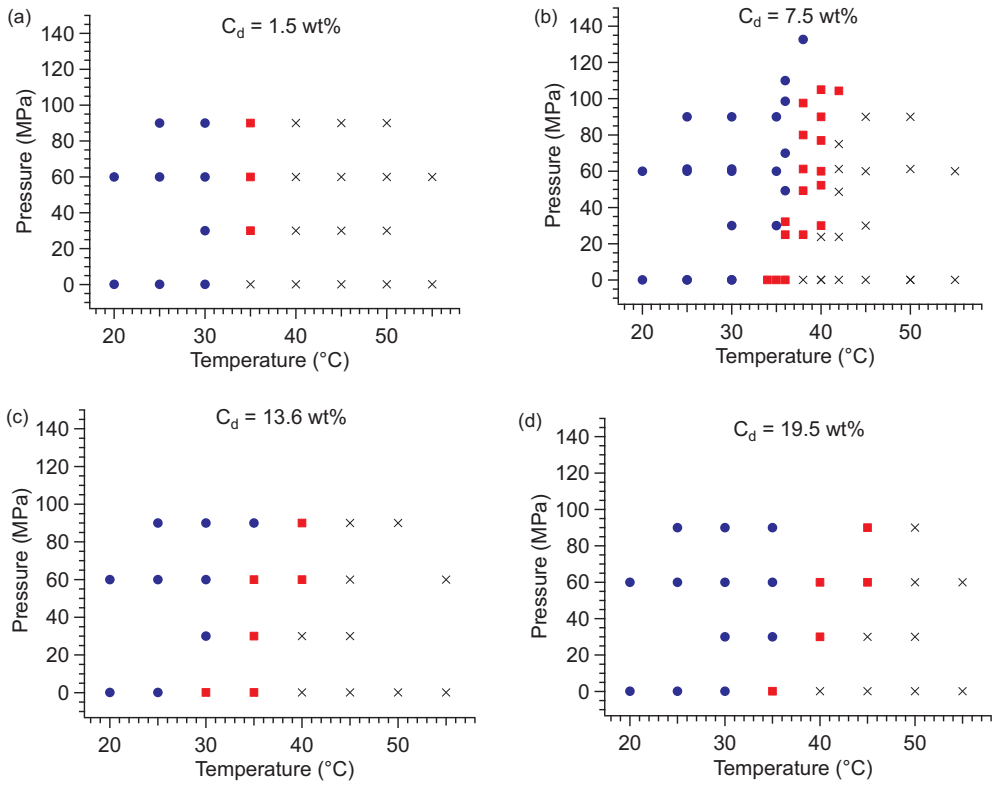

Figure 6.20: Pressure-temperature phase diagrams, derived from variable pressure deuterium NMR spectra, for 20 wt% d3 nipam microgel synthesized with crosslink densities (a) 1.5 wt%, (b) 7.5 wt%, (c) 13.6 wt%, and (d) 19.5 wt% BIS/monomer. The pressure temperature points correspond to (blue circle) swollen, (red square) semi-swollen, and (black cross) collapsed microgel states.

While spacing of points makes it difficult to precisely determine the slope of the coexistence lines in the $P-T$ diagrams of Figure 6.20, comparison does suggest that the least change (increase) in the transition temperature with increasing pressure happens in the lowest crosslink density microgel of C_d=1.5 wt%. The slope of the phase boundary on the $P-T$ phase diagram, $\frac{dP}{dT}$, gives the change in entropy divided by the change in volume $\frac{\Delta S}{\Delta V}$ at the transition, as given by the Clausius-Clapeyron equation (1.3) in Section 1.3.

Kunugi *et al.* [32] suggest that the entropy and volume both increase at the transition from swollen phase to collapsed phase for low pressures. This would imply an increase in total system volume on going from the swollen phase, in which the chains are well solvated, to the collapsed phase, in which the chains interact hydrophobically. The apparent effect

of crosslink density on the slope of the $P-T$ phase diagram coexistence line suggests that the ratio of entropy change to volume at the transition decreases with increasing crosslink density. This dependence on crosslink density could reflect an increase in volume change with crosslink density or a decrease in entropy change with crosslink density or a combination of both effects. Andersson and Maunu [21] investigated the effect of crosslink density on collapse transition enthalpy using differential scanning calorimetry. For synthesis conditions similar to those used in this work, they found that the transition enthalpy decreased with increasing crosslink density. This implies that the change in entropy at the transition should also decrease with increasing crosslink density, a result that, at least in part, could account for observed decrease in $\frac{dP}{dT}$ with increasing crosslink density. This suggests that the largest change in entropy, at the transition, occurs for the smallest crosslink density and thus for the situation in which the largest amount of water is displaced from individual microgel particles at the transition, as shown by DLS results in Section 5.1. This is also corresponds to the largest drop in the ^{2}H NMR signal being for the lowest crosslink density, as shown in Figure 6.16, for the ambient pressure spectra.

Figure 6.21 provides samples of spectra obtained for a series of temperatures at a constant pressure (60 MPa) for all four crosslink densities.

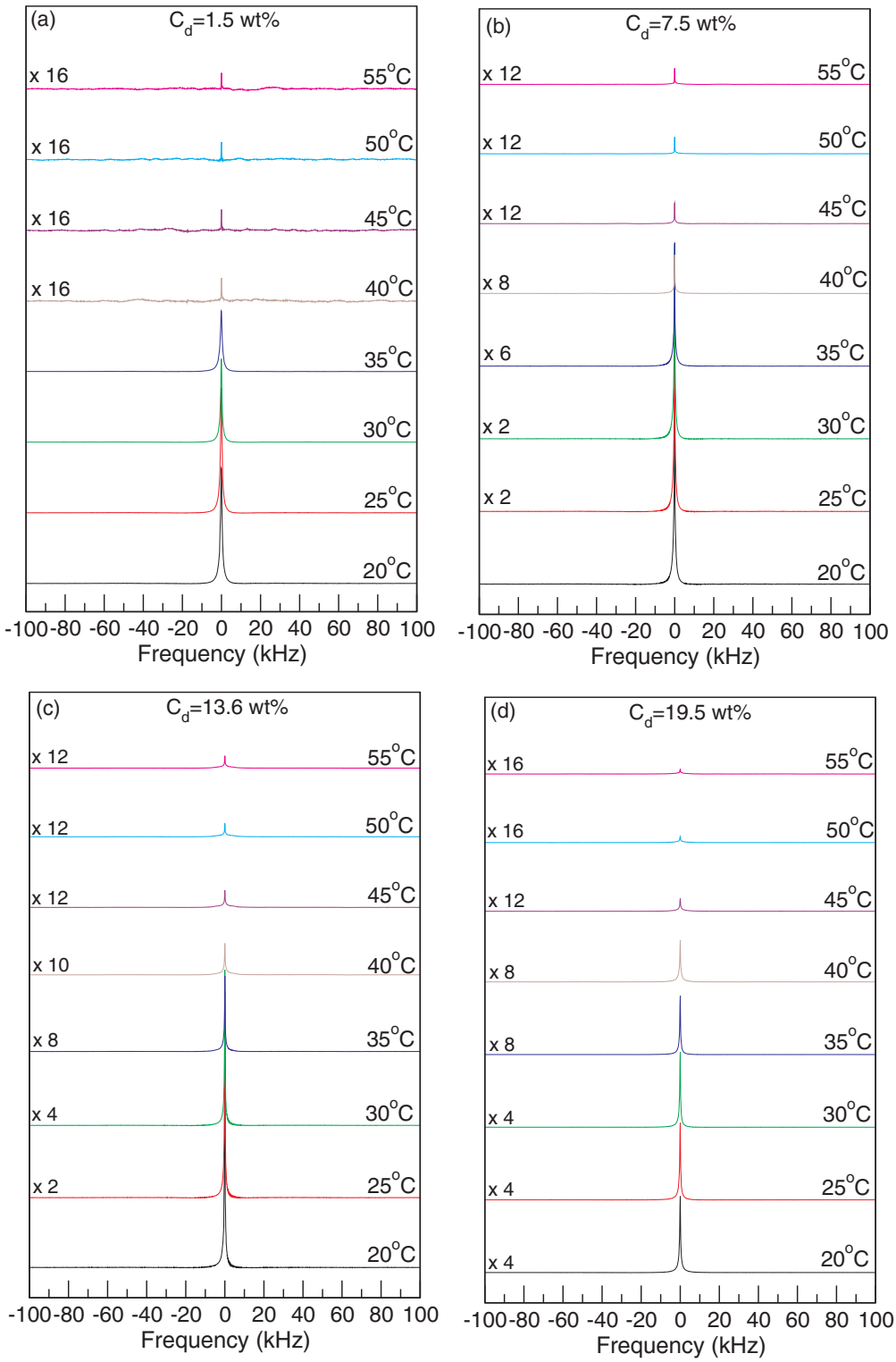

Figure 6.21: Deuterium NMR spectra at 60 MPa and selected temperatures for 20 wt% suspensions of d3 nipam microgel at crosslink densities of (a) C_d=1.5 wt%, (b) C_d=7.5 wt%, (c) C_d=13.6 wt%, and (d) C_d=19.5 wt%.

Because of the low field used for the variable pressure study and the background signal that was coming from different components in the variable-pressure probe, the signal-to-noise ratio was not high enough, in most of the collapsed phase spectra, to show clearly any prominent Pake doublet edges arising from an immobile fraction of microgel segments. For the C_d=19.5 wt% sample, though, edges were seen in some spectra. Figure 6.22 shows normalized spectra for the C_d=19.5 wt% microgel sample at two temperatures for a series of pressures. The spectra are plotted with colors that are consistent with the microgel states as classified previously in the phase diagrams shown in Figure 6.20. The spectra in (blue, red, and black) correspond to swollen, semi-swollen, and collapsed microgel states, respectively. In these spectra, it is possible to see the clear change in the spectral shape as the microgel undergoes the VPT.

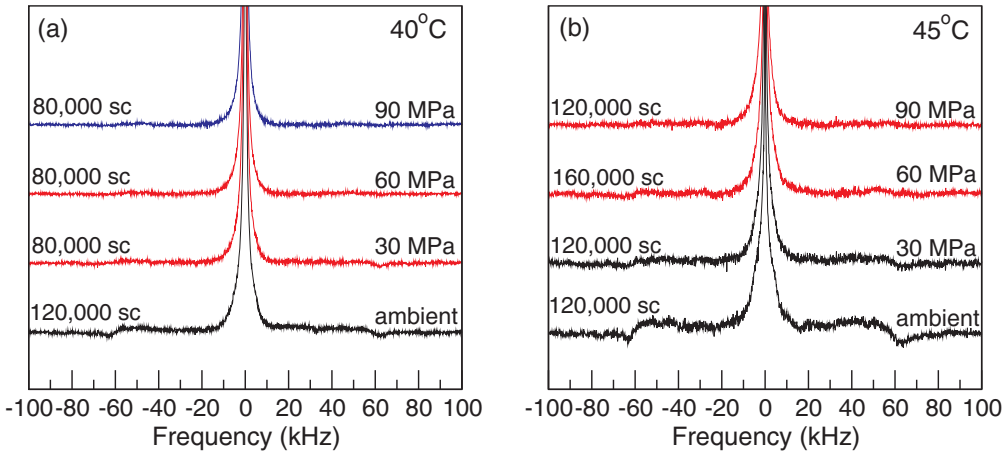

Figure 6.22: Normalized deuterium NMR spectra for a 20 wt% suspension of d3 nipam microgel with a crosslink density C_d=19.5 wt% for a series of pressures at (a) 40°C and (b) at 45°C. The spectra in (blue, red, and black) correspond to swollen, semi-swollen, and collapsed microgel states, respectively.

The spectra in Figure 6.22 (b) shows that with increasing pressure the microgel changes from being in the collapsed phase (indicated from the rigid segment component) back to the swollen phase (indicated from the narrower central peak and no rigid segments component), and thus the transition temperature has shifted to higher temperatures. The baseline distortions in the spectra is coming from a background signal in the probe that we cannot

remove. For the highest crosslink density C_d=19.5 wt%, the transition temperature increases the most as the pressure increases so that this samples gives the smallest slope ($\frac{dP}{dT}$) of the $P-T$ phase boundary. $\frac{dP}{dT}$ is large for all crosslink densities and slightly larger for smallest crosslink density. Regardless of the crosslink density, the steepness of the phase boundary in the $P-T$ diagram suggests that the change in polymer volume at the collapse transition is small.

Chapter 7

Discussion and Conclusion

The microgels prepared for this study consist of particles that are made of a thermoresponsive polymer (polynipam) with varying crosslink density, C_d=1.5, 7.5, 13.6, and 19.5 wt%. Two versions of each crosslinked microgel were made: non-deuterated, and deuterated.

DLS measurements of particle size as a function of temperature showed that the transition temperature for these microgels varies between 32.5°C and 35°C (h nipam) or between 33.5°C and 38°C (d3 nipam), showing a weak increase with C_d. The biggest change in particle volume, and thus swelling factor, corresponds to the smallest C_d. Similar observations were previously reported [18–20]. As the crosslink density was increased the volume transition broadened and the swelling capacity decreased. Table 7.1 below shows the swelling factors at different cross-linking densities of polynipam microgels, that are calculated from DLS data, in different studies from the literature compared to our data.

The swelling behavior can be understood in the context of the discussion of the coil-globule transition in Section 1.2. The balance between the mixing and elasticity osmotic pressures controls the swelling capacity in neutral microgels. As the crosslink density increases, the competition between the solvency and elasticity increases, which makes the system more resistant to the phase transition. In low crosslinked microgels the transition occurs more easily because of the lower elasticity component [14].

Table 7.1: Literature review [18–20] of the C_d effect on the swelling factor in microgels, compared to data presented here.

Current work		Stieger *et al.* 2004	
C_d (wt%)	$(R_{25}/R_{39})^3$	C_d (wt%)	$(R_{25}/R_{39})^3$
1.5	10.4	1.9	12.4
7.5	5.5	7.5	6.1

Senff and Richtering 2000		Current work		Contreras-Caceres *et al.* 2015	
C_d (wt%)	$(R_{20}/R_{40})^3$	C_d (wt%)	$(R_{20}/R_{40})^3$	C_d (wt%)	$(R_{20}/R_{40})^3$
1.9	13.9	1.5	12.5		
7.2	8.5	7.5	6.3	6.9	4.8
		13.6	4.1	13.8	4.4
		19.5	3.0	24.5	3.4

The rheological characterization of these microgels indicated a decrease in viscosity as a function of shear rate. That is consistent with the known shear-thinning behavior in microgels. The measured viscosity dependence on the shear rate, for the concentrated suspensions and at low T, obeyed the Cross model for shear-thinning polymers. Three regions were detected: a low shear plateau; a power law behavior in the intermediate shear rate range; and a high shear plateau. The zero-shear viscosity was obtained using the Cross fit. This high concentration, low temperature regime was found to display gel-like behavior. The microgel in this regime, where particles are in contact and overlapping, is more elastic than viscous. For low concentration samples at high temperature, the stress *versus* the shear rate at low shear was linearly fitted to obtain the zero-shear viscosity. This low concentration and high temperature regime displays a colloid-like behavior. The microgel in this regime, where the particles are far from each other, is more viscous than elastic and the dominant behavior is the behavior of the medium, water. The zero-shear viscosities obtained by both methods, in an intermediate regime when both methods were applicable, were consistent. The zero-shear viscosity was found to decrease with increasing temperature.

The intermediate region of the viscosity-shear rate relation was tested to find the exponent corresponding power law behavior. The exponent $m_{apparent}$ was found to be close to 0.9 in

the gel-like regime, indicating a strong shear-thinning behavior in this regime. On the other hand, in the regime where the microgel behaves like colloid, the exponent was close to a much lower value near 0.1. In between, the suspension viscosities were well fit by Cross equation indicating that this was also in the gel-like regime.

The viscosity of hard-sphere colloidal suspensions is mostly governed by just the volume fraction. An effective volume fraction was calculated by employing the DLS results of the particle volume as a function of T, coupled with the assumption that at low enough concentrations, in the collapsed phase, one could employ the Krieger-Dougherty model for the relative viscosity-volume fraction behavior in hard spheres. The water volume fraction within the particle was found to be ~ 0.6 in the collapsed phase. That result is consistent with previous neutron scattering measurements by Stieger [19].

The relative viscosity behavior as a function of the effective volume fraction ϕ_{eff} was found to be consistent with hard sphere behavior until a volume fraction of ~ 0.6. At higher volume fraction, the viscosity behavior deviates noticeably from hard sphere behavior. At high enough concentration the soft particles might be compressed or overlap, and their viscosity behavior is not hard-sphere-like in this regime. The transition in viscosity behavior can be seen clearly from the individual relative viscosity *versus* volume fraction plots for each C_d (Figures 5.16 (b,d,f,h)). While the KD line reaches a relative viscosity of 10^3 at a volume fraction of 0.62, the microgels reach that value at much higher ϕ_{eff}. This is consistent with earlier studies [4].

In the current work, it was found that lower C_d corresponds to softer particles, i.e. for higher ϕ_{eff} when η_{rel}=10^3. That is probably because of the lower rigidity of the particles at low C_d. This was consistent with the rheological study of microgel by Senff and Richtering [18] in which it was found that the relative viscosity approached hard sphere behavior with increasing crosslink density.

The behavior of the exponent $m_{apparent}$, corresponding to the power law region, also has a transition at $\phi_{eff} \sim 0.6$. $m_{apparent}$ has a value of 0.1 at lower ϕ_{eff} but $m_{apparent} \sim 0.9$

above a threshold volume fraction. This threshold decreased with increasing C_d. This is an indication that the microgel is more like a Newtonian colloidal fluid below this volume fraction and is like an elastic gel above that. The storage modulus G' was larger than the loss modulus G'' in the gel-like regime, indicating the elasticity of the soft particles in that regime. On the other hand, the loss modulus was higher than the storage modulus in the colloidal regime, which is a property of a Newtonian fluid. This observation is consistent to what was found by Senff and Richtering [4], where the sample behaved as a viscoelastic solid; the storage modulus was higher than the loss modulus in the whole frequency range. Upon heating, the sample changed to a viscoelastic liquid with $G'' > G'$.

The NMR study, at ambient pressure, indicated an LCST about 35°C for all samples. The biggest change in particle internal structure at the transition was found to correspond to the lowest C_d. These two findings are consistent with what was indicated by both DLS data, and water fraction - temperature behavior from rheology measurements. The spectra revealed that the particles in the swollen phase, below the LCST, had freely moving polymer segments. Above the collapse transition, a small fraction of immobile segments were detected. At higher C_d, immobile segments were also detected in the swollen phase. A huge loss of the NMR signal intensity above the transition, for the microgel suspensions with lower crosslink densities, suggested that a significant fraction of the segments were reorienting at an intermediate rate that made them spectroscopically invisible. For high crosslink densities, that fraction was smaller.

A similar observation, by Andersson and Maunu [21], of the loss of ^{1}H solution NMR signal above the transition in microgels, due to the line broadening, indicated that segment motion is not as fast in the collapsed phase as in the swollen phase. However, solution NMR presumably would not be able to tell if the loss of signal was due to immobilization or just slowing of the segments. ^{2}H NMR distinguishes segments with intermediate correlation time motions, which can, in effect, be spectroscopically invisible, from nearly immobilized segments, which give a Pake doublet spectral component with the maximum possible quadrupole

splitting. In addition, ^{2}H NMR and rheology both suggest that the collapse phase is still significantly hydrated. This work provides insight into the presence of reorienting segments as well as immobilized segments in the collapse phase, along with an estimation of the fraction of collapsed phase particle volume that is accounted for by water. The findings reported here are thus complementary to the earlier solution NMR results.

Variable pressure NMR (Section 6.6) showed that the collapse transition temperature is increased by raising pressure. It was found that this increase was most noticeable for the highest crosslink density. In other words, the steepest coexistence line, highest $\frac{dP}{dT}$ value of the slope, was for the lowest crosslink density. According to Clausius-Claperyon equation, the slope of the coexistence line $\frac{dP}{dT}$ represents $\frac{\Delta S}{\Delta V}$. The change in volume ΔV is the change in the sample overall volume, including both the water and the polymer molecules.

On warming through the collapse transition at 35°C, the change from hydrated polymer to hydrophobic polymer involves a small increase in sample volume [32]. In the swollen phase, the water molecules and the solvated polymer molecules pack more densely than in the collapsed phase where water and polymer separate and polymer chains interact hydrophobically. Given that ΔV is positive at the transition, the observation that $\frac{dP}{dT}$ is positive indicates that the entropy also increases at the transition. The work reported here suggests that $\frac{\Delta S}{\Delta V}$ is slightly higher at lower crosslink density than at higher crosslink density. This is consistent with the finding by Anderson and Maunu [21], using DSC, that the collapse transition enthalpy decreases slightly with increasing crosslink density.

The collapsed phase, in which polymer chains interact hydrophobically, is more compressible than in the swollen (solvated) phase. The system can thus be driven back, from the collapsed phase to the swollen phase, by increasing pressure to about 50 MPa at 35°C. In effect, increasing pressure and temperature drive the system phase transition oppositely.

7.1 Insights from this study

From DLS work (Chapter 5), our observations that the biggest change in particle's volume occurs at the lowest crosslink density and that the transition temperature shifts most for the highest C_d, were consistent to previous observations [18, 21].

From rheology measurements (Chapter 5), we found measurements of the apparent exponent of the power law region of the viscosity-shear rate curve to be a powerful method to distinguish between the microgel phases. The relative viscosity, obtained from steady shear measurements, approached hard sphere behavior with increasing temperature and crosslink density. The storage and loss moduli, obtained from the SAOS tests, were consistent with the steady shear results.

The ^{2}H NMR results, both at ambient and variable pressure, (Chapter 6) reported here represent the first experiments using ^{2}H NMR to probe microgel structure. The ambient pressure study revealed that the polymer segments within the microgel particle are nearly freely reorienting in the swollen phase while a fraction is completely rigid in the collapsed phase. An earlier study, using ^{1}H solution NMR [21], similarly indicated fast motion of the segments in the swollen phase and slower motion in the collapsed phase. The ^{2}H NMR study reported here provided additional insights regarding the presence of both immobile segments and mobile segments in the collapsed phase. The current work also revealed the presence of immobile segments even in the swollen phase for the highest C_d. The findings reported here complement the earlier solution NMR results.

Similar microgel chain dynamics were observed in the swollen and collapsed phases when obtained through a temperature induced and/or pressure induced phase transition. The pressure induced transition from the collapsed to swollen phase was probed at about 35°C with increasing pressure from ambient pressure (0.1 MPa) to about 50 MPa. This is consistent with previous findings using DLS [32]. The obtained P-T diagram is also similar to what was obtained previously [32].

Both rheology and NMR point to the fact that there is a significant amount of water in the microgel in the collapsed phase. The techniques provide complementary windows into the microgel behavior. Whereas gel-like behavior below the VPTT is most interesting rheologicaly, the ^{2}H NMR shows interesting behavior, the emergence of broad spectral components, above VPTT.

7.2 Implications for future work

It would be helpful to develop a better understanding of the intermediate reorientations that results in the significant loss of ^{2}H NMR signal at the transition. The loss of signal at the transition is smaller for polymer deuterated on the sidechain than for backbone-deuterated polymer. It is possible that selective deuteration could provide a way to usefully separate backbone and sidechain dynamics in the collapsed phase. ^{2}H NMR spectroscopy in a much higher field might also provide a way to observe deuterons on segments with intermediate rate motions directly.

It would be interesting to investigate the effect of varying pressure on the microgel polymer microstructure by using deuterium NMR on smaller temperature steps in order to map the $P-T$ diagram more precisely. It was observed by DLS that at elevated pressures the microgel system has a reversed transition, i.e. back from swollen to collapsed. If one can extend the variable pressure ^{2}H NMR study to elevated pressures to see what happens to the particle structure in that regime. Whether the swollen phase achieved by raising pressure for elevated pressures is similar or different to that achieved by raising temperature at atmospheric pressures, might be helpful for a better understanding of the thermodynamics of the microgel system.

Oscillatory shear measurements might be extended to cover more temperature steps so one can understand the change, on a macroscopic scale, of the microgel visco-elastic properties through the transition from the gel-like to the colloid-like regimes.

The theory and simulation of microgel colloids is actively being developed. Urich and Denton [68] suggest that rheological properties, such as diffusion coefficients, viscosity, *etc.* would be accessible to simulations using their model. Detailed comparisons of the experiments in this study to simulations might therefore be possible in the near future.

Appendices

Appendix A

Small amplitude oscillatory shear results of the storage and loss moduli

In Figure A.1 (a) the SAOS test was carried out at 5°C and 20°C, for the microgel sample of C_d=1.5 wt% and C=1.5 wt%. Both below the collapse transition ,i.e. below T=35°C. In both cases the storage modulus G' (filled symbols) was lower than the loss modulus G'' at low frequencies ω. The storage modulus was very low value, $G' \sim 0.1$ Pa. This is an indication that microgels behaved as a Newtonian fluid with a colloidal behavior at low concentration, even at low temperatures.

In Figure A.1 (b) the SAOS test was carried out at 5°C, 20°C and 35°C, for the microgel sample of C_d=1.5 wt% and C=4.5 wt%. At 5°C and 20°C, the storage modulus G' (filled symbols) was higher than the loss modulus G'' at low frequencies ω, with a $G' \sim 50$ Pa. G' is larger than G'' when the microgel particles are soft (elastic) and in the gel-like regime. At 35°C, the microgel behaved like colloid.

For the higher concentration sample C=8 wt% from the same C_d, shown in Figure A.1 (c), measurements were carried out at temperatures 5°C and 20°C (below the transition) and at T=35°C (at the transition). Same behavior of $G' > G''$ was observed below the transition but with storage moduli that are higher than the ones for the $C = 4.5$ wt% by an order of

magnitude. This is an indicative that the higher the concentration within the same crosslink density, the softer are the particles (more elastic). For the high temperature (35°C), G' still higher than G'' at low ω, but they overlap at high ω.

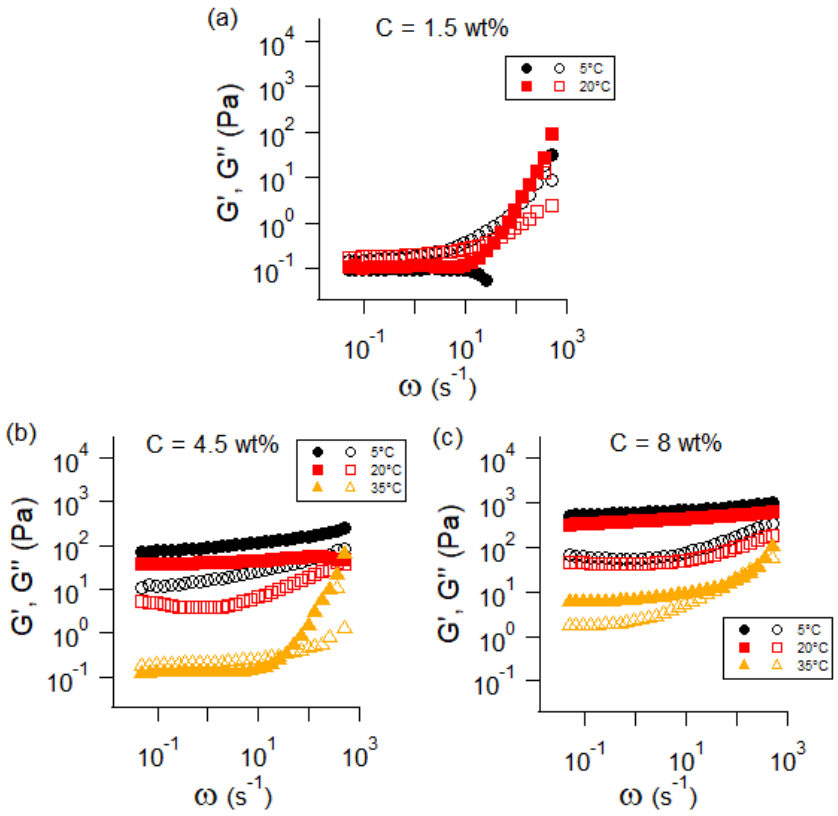

Figure A.1: The SAOS experiment results for the microgel samples of C_d=1.5 wt% at concentrations of: a) C=1.5 wt%, b) C=4.5 wt% and c) C=8 wt%. The storage (filled symbols) and loss (empty symbols) moduli are plotted as a function of frequency at different temperatures.

Figures A.2 and A.3 shows SAOS results for microgels with C_d=7.5 wt% and 13.6 wt%, respectively.

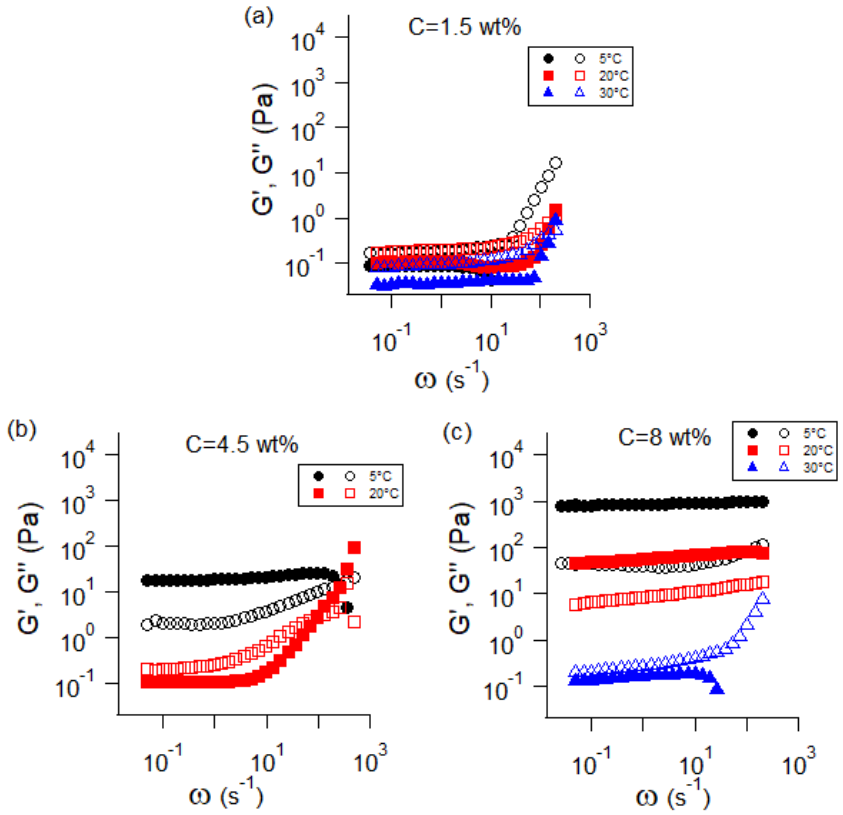

Figure A.2: The SAOS experiment results for the microgel samples of C_d=7.5 wt% at concentrations of: a) C=1.5 wt%, b) C=4.5 wt%,and c) C=8 wt%. The storage (filled symbols) and loss (empty symbols) moduli are plotted as a function of frequency at different temperatures.

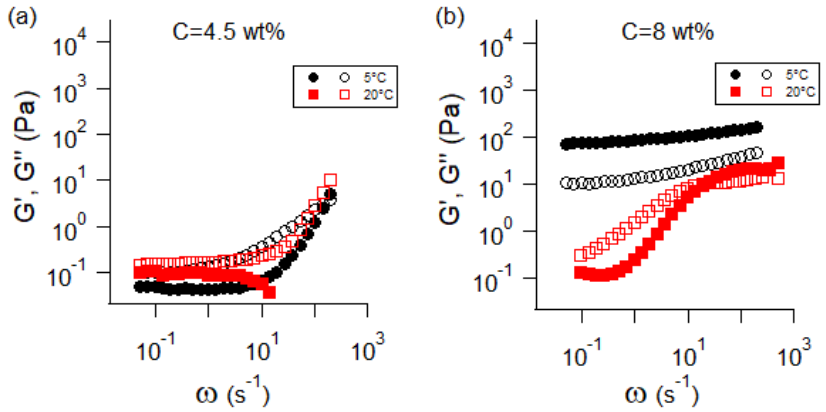

Figure A.3: The SAOS experiment results for the microgel samples of C_d=13.6 wt% at concentrations of: a) C=4.5 wt% and b) C=8 wt%. The storage (filled symbols) and loss (empty symbols) moduli are plotted as a function of frequency at different temperatures.

Figure A.4 (a) shows the SAOS tests results for the microgel sample of C_d=19.5 wt% and C=4.5 wt%, at temperatures 5°C and 20°C below the transition. The G' moduli at both temperatures are low and lower than the G'' moduli. This indicates that at higher C_d, even at the C=4.5 wt% concentration, the microgel behaves as a colloid at low temperatures. Which leads to the conclusion that the higher the crosslink density in microgels, the more it is in the colloidal regime at low concentrations and temperatures.

On the other hand, at high concentration C=12 wt% of the high crosslink density microgel, shown in Figure A.4 (b), the higher is the G' at low temperatures ($G' \sim 10^3$ Pa). An indicative of stiffer particles in the gel-regime for the higher C_d.

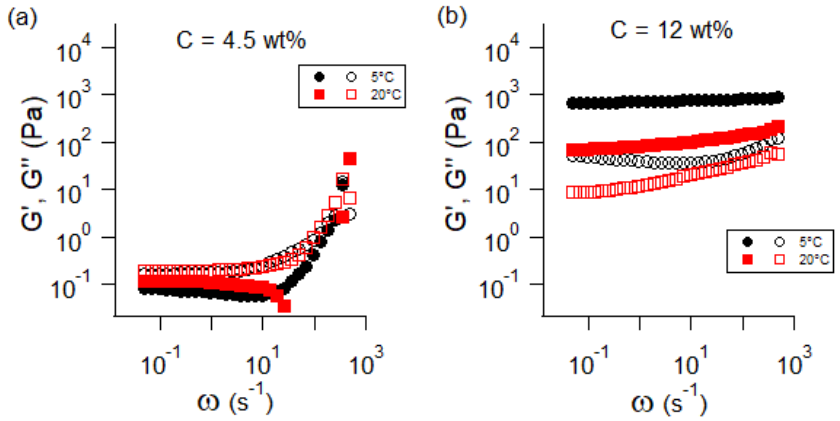

Figure A.4: The SAOS experiment results for the microgel samples of C_d=19.5 wt% at concentrations of: a) C=4.5 wt% and b) C=12 wt%. The storage (filled symbols) and loss (empty symbols) moduli are plotted as a function of frequency at different temperatures.

Appendix B

^{2}H NMR spectral peak simulation

In an effort to understand the narrow spectral components found in the swollen phase, the narrow spectra of the d7 nipam suspension at 5 wt% sample, were simulated using a superposition of Pake doublets with a distribution of very small splittings. A vector of S_{CD} values, along with an initial guess of the weightings for these values, was entered into a simulation code written in the Octave environment, that superimposes spectral doublets with the given S_{CD} values and weights into a spectrum. The simulated spectrum was fit to the experimental spectrum by minimizing the Chi square difference between them. After the Chi square was minimized, the resulting weightings were reported and the residual between the simulated and the experimental spectra was obtained.

In order to approximate the observed narrow spectra, at low temperatures, it was necessary to sum about 60 spectral components having a narrow distribution of splittings (order parameters values (S_{CD})) that was heavily weighted to the smallest splittings. At higher temperatures (broader spectra), fitting required fewer S_{CD} values (about 30 spectral components) distributed over a slightly broader range of splitting that was not as heavily weighted to small splittings as at low temperatures.

Figures B.1 (a,b,c,d) show examples of spectra simulated in this way, for the d7 nipam samples at the temperatures 30°C, 40°C, 50°C, and 60°C, respectively. In each panel, the

weights (frequency) of the S_{CD} values that were used to obtain the plotted simulated spectrum are presented in histograms and plotted in the corresponding panel. One can notice that the black and the green lines, corresponding to the experimental and simulated spectra, respectively, are identical. The red lines represent the residuals.

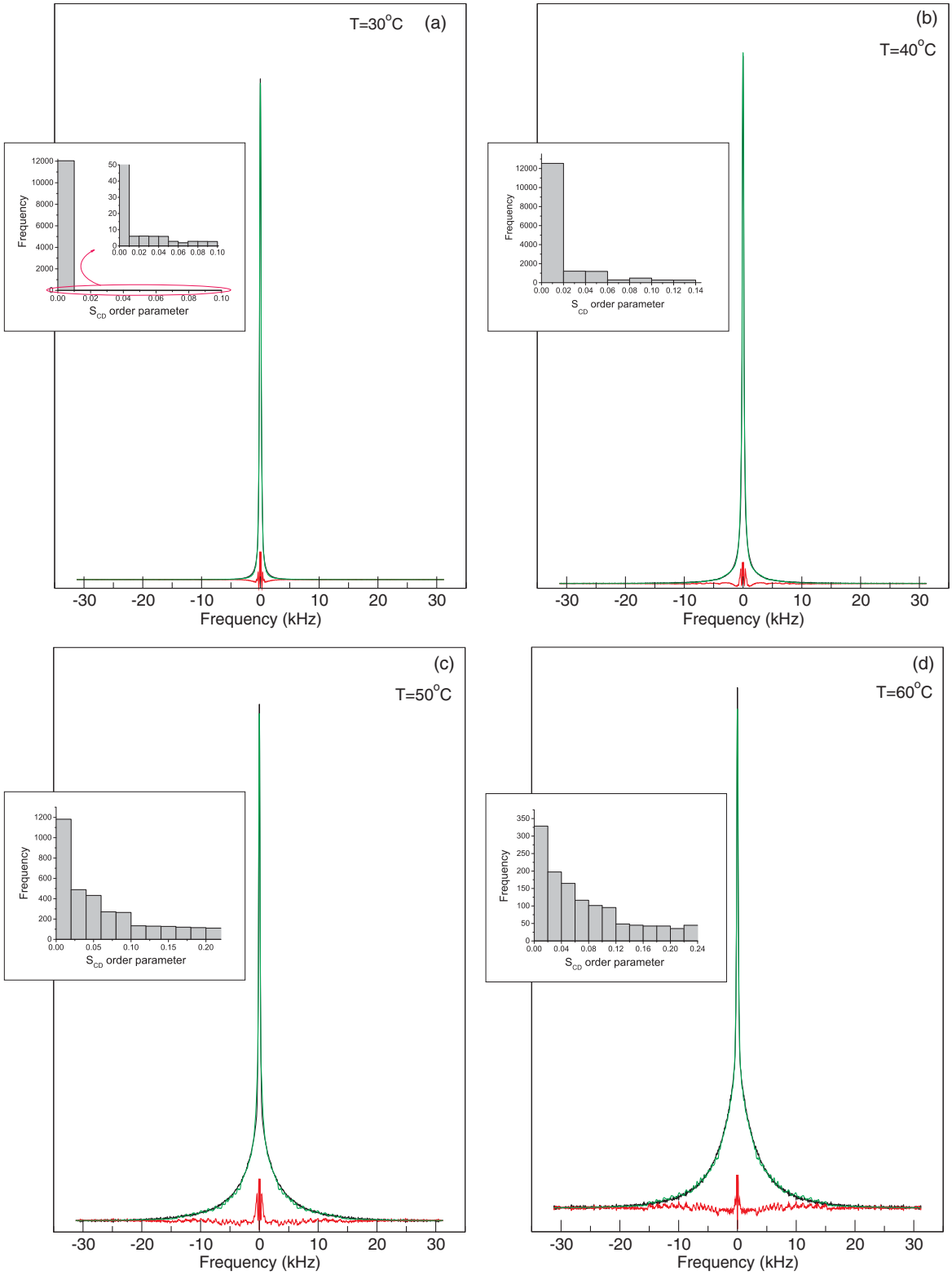

Figure B.1: Simulations of the spectra of the d7 suspension at 5 wt% sample along with the frequency of the order parameter S_{CD} values that are used in the simulated spectrum, at the temperatures (a) 30°C, (b) 40°C, (c) 50°C, and (d) 60°C. The black and green lines represent the experimental and simulated spectra, respectively. The red lines represent the residuals.

Bibliography

[1] B Sierra-Martin, J Retama, M Laurenti, A Barbero, and E Cabarcos. Structure and polymer dynamics within PNIPAM-based microgel particles. *Adv Colloid Interface Sci*, 205:113–123, 2014.

[2] M Das, H Zhang, and E Kumacheva. Microgels: old materials with new applications. *Annu Rev Mater Res*, 36:117–142, 2006.

[3] H Schild. Poly(N-isopropylacrylamide): experiment, theory and application. *Prog Polym Sci*, 17:163–249, 1992.

[4] H Senff and W Richtering. Temperature sensitive microgel suspensions: colloidal phase behavior and rheology of soft spheres. *Chem Phys*, 111:1705–1711, 1999.

[5] J Lietor-Santos, B Sierra-Martin, R Vavrin, Z Hu, U Gasser, and A Fernandez-Nieves. Deswelling microgel particles using hydrostatic pressure. *Macromolecules*, 42:6225–6230, 2009.

[6] K Kratz, T Hellweg, and W Eimer. Influence of charge density on the swelling of colloidal poly(N-isopropylacrylamide-co-acrylic acid) microgels. *Colloids Surfaces A Physicochem Eng Asp*, 170:137–149, 2000.

[7] S Nöjd, P Mohanty, P Bagheri, A Yethiraj, and P Schurtenberger. Electric field driven self-assembly of ionic microgels. *Soft Matter*, 9:9199–9207, 2013.

[8] P Mohanty, A Yethiraj, and P Schurtenberger. Deformable particles with anisotropic interactions: unusual field-induced structural transitions in ultrasoft ionic microgel colloids. *Soft Matter*, 8:10819–10822, 2012.

[9] F Scheffold, P Diaz-Leyva, M Reufer, N Ben-Braham, I Lynch, and J Harden. Brushlike interactions between thermoresponsive microgel particles. *Phys Rev Lett*, 104:128304, 2010.

[10] M Murray and M Snowden. The preparation, characterisation and applications of colloidal microgels. *Adv Colloid Interface Sci*, 54:73–91, 1995.

[11] J Lietor-Santos, B Sierra-Martin, U Gasser, and A Fernandez-Nieves. The effect of hydrostatic pressure over the swelling of microgel particles. *Soft Matter*, 7:6370–6374, 2011.

[12] M Rubinstein and R Colby. *Polymer Physics*. Oxford University Press, New York, 2003.

[13] R Jones. *Soft Condensed Matter*. Oxford University Press, New York, 2002.

[14] P Flory. *Principles of Polymer Chemistry*. Cornell University Press, Ithaca, 1953.

[15] K Sharma. *Polymer Thermodynamics: Blends, Copolymers and Reversible Polymerization*. Taylor & Francis, Boca Raton, 2011.

[16] B Saunders and B Vincent. Microgel particles as model colloids: theory, properties and applications. *Adv Colloid Interface Sci*, 80:1–25, 1999.

[17] A Guillermo, J Addad, J Bazile, D Duracher, A Elaissari, and C Pichot. NMR investigations into heterogeneous structures of thermosensitive microgel particles. *Polym Sci Part B Polym Phys*, 38:889–898, 2000.

[18] H Senff and W Richtering. Influence of cross-link density on rheological properties of temperature-sensitive microgel suspensions. *Colloid Polym Sci*, 278:830–840, 2000.

[19] M Stieger, W Richtering, J Pedersen, and P Lindner. Small-angle neutron scattering study of structural changes in temperature sensitive microgel colloids. *Chem Phys*, 120:6197–6206, 2004.

[20] R Contreras-Cáceres, L Schellkopf, C Fernández-López, I Pastoriza-Santos, J Pérez-Juste, and M Stamm. Effect of the cross-linking density on the thermoresponsive behavior of hollow PNIPAM microgels. *Langmuir*, 31:1142–1149, 2015.

[21] M Andersson and S Maunu. Volume phase transition and structure of poly(N-isopropylacrylamide) microgels studied with 1H-NMR spectroscopy in D2O. *Colloid Polym Sci*, 285:293–303, 2006.

[22] M Badiger, P Rajamohanan, M Kulkarni, S Ganapathy, and R Mashelkar. Proton MASS-NMR: A New Tool To Study Thermoreversible Transition in Hydrogels. *Macromolecules*, 24:106–111, 1991.

[23] W Su, K Zhao, J Wei, and T Ngai. Dielectric relaxations of poly(N-isopropylacrylamide) microgels near the volume phase transition temperature: impact of cross-linking density distribution on the volume phase transition. *Soft Matter*, 10:8711–8723, 2014.

[24] P Chambon, L Chen, S Furzeland, D Atkins, J Weaver, and D Adams. Poly(N-isopropylacrylamide) branched polymer nanoparticles. *Polym Chem*, 2:941–949, 2011.

[25] H Shewan and J Stokes. Viscosity of soft spherical micro-hydrogel suspensions. *Colloid Interface Sci*, 442:75–81, 2015.

[26] M Liu, C Taylor, B Chong, L Liu, A Bilic, N Terefe, R Stockmann, S Thang, and K De-Silva. Conformational transitions and dynamics of thermal responsive poly(N-isopropylacrylamide) polymers as revealed by molecular simulation. *Eur Polym*, 55:153–159, 2014.

[27] Y Wang, M Yan, L Xu, W Zhao, and X Wang. Aptamer-functionalized DNA microgels: a strategy towards selective anticancer therapeutic systems. *Mater Chem B*, 4:5446–5454, 2016.

[28] L Jelinski. Solid state deuterium nmr studies of polymer chain dynamics. *Annu Rev Mater Sci*, 15:359–377, 1985.

[29] J Dechézelles, V Malik, J Crassous, and P Schurtenberger. Hybrid raspberry microgels with tunable thermoresponsive behavior. *Soft Matter*, 9:2798, 2013.

[30] J Callejas-Fernández, J Ramos, J Forcada, and A Moncho-Jordá. On the scattered light by dilute aqueous dispersions of nanogel particles. *Colloid Interface Sci*, 450:310–315, 2015.

[31] G Conley, S Nöjd, M Braibanti, P Schurtenberger, and F Scheffold. Superresolution microscopy of the volume phase transition of pNIPAM microgels. *Colloids Surfaces A Physicochem Eng Asp*, 499:18–23, 2016.

[32] S Kunugi, Y Yamazaki, K Takano, N Tanaka, and M Akashi. Effects of ionic additives and ionic comonomers on the temperature and pressure responsive behavior of thermoresponsive polymers in aqueous solutions. *Langmuir*, 15:4056–4061, 1999.

[33] P Mohanty, D Paloli, J Crassous, E Zaccarelli, and P Schurtenberger. Effective interactions between soft-repulsive colloids: experiments, theory, and simulations. *Chem Phys*, 140:94901, 2014.

[34] B Tan, K Tam, Y Lam, and C Tan. Dynamics and microstructure of charged soft nano-colloidal particles. *Polymer (Guildf)*, 45:5515–5523, 2004.

[35] W Russel, D Saville, and W Scowalter. *Colloidal Dispersions*. Cambridge University Press, New York, 1989.

[36] W Poon. *Colloidal Suspensions*. Clarendon Press, Oxford, 2012.

[37] P Pusey. Dynamic Light Scattering. In P Lindner and T Zemb, editors, *Neutrons, X-Rays Light*. Elsevier, Boston, 2002.

[38] M Rao. *Rheology of Fluid and Semisolid Foods*. Springer, Boston, 2007.

[39] M Cross. Rheoloy of non-Newtonian fluids: a new flow equation for pseudolpastic systems. *Colloid Sci*, 20:417–437, 1965.

[40] U Gasser, J Hyatt, J Lietor-Santos, E Herman, L Lyon, and A Fernandez-Nieves. Form factor of pNIPAM microgels in overpacked states. *Chem Phys*, 141:034901, 2014.

[41] D Sessoms, I Bischofberger, L Cipelletti, and V Trappe. Multiple dynamic regimes in concentrated microgel systems. *Philos Trans R Soc A*, 367:5013–5032, 2009.

[42] L Dahbi, M Alexander, V Trappe, J Dhont, and P Schurtenberger. Rheology and structural arrest of casein suspensions. *Colloid Interface Sci*, 342:564–570, 2010.

[43] C Macosko. *Rheology Principles, Measurements, and Applications.* VCH, New York, 1994.

[44] Z Cheng, P Chaikin, W Russel, W Meyer, R Rogers, and R Ottewill. Phase diagram of hard spheres. *Mater Des*, 22:529–534, 2001.

[45] A Einstein. A new determination of molecular dimensions. *Ann Phys*, 19:289–306, 1906.

[46] G Batchelor. The effect of Brownian motion on the bulk stress in a suspension of spherical particles. *Fluid Mech*, 83:97, 1977.

[47] I Krieger and T Dougherty. A mechanism for non-Newtonian flow in suspensions of rigid spheres. *Trans Soc Rheol*, 3:137–152, 1959.

[48] M Bloom. NMR studies of membranes and whole cells. *Zeitschrift für Phys Chemie*, 153:67, 1987.

[49] M Levitt. *Spin Dynamics: Basics of Nuclear Magnetic Resonance.* John Wiley & Sons Ltd, England, 2008.

[50] J Keeler. *Understanding NMR Spectroscopy.* Wiley, England, 2005.

[51] M Cohen and F Reif. Quadrupole effects in nuclear magnetic resonance studies of solids. *Solid State Phys*, 5:321–438, 1957.

[52] J Davis. The description of membrane lipid conformation, order and dynamics by 2H-NMR. *Biochim Bophysica Acta*, 737:117–171, 1983.

[53] J Seelig. Deuterium magnetic resonance: theory and application to lipid membranes. *Q Rev Biophys*, 10:353–418, 1977.

[54] J Polson, J Fyfe, and K Jeffrey. The reorientation of t-butyl groups in butylated hydroxytoluene: A deuterium nuclear magnetic resonance spectral and relaxation time study. *Chem Phys*, 94:3381, 1991.

[55] E Sternin. *Some mechanisms of transverse nuclear magnetic relaxation in model membranes.* PhD thesis, University of British Columbia, 1988.

[56] J Thewalt. *Deuterium NMR studies of model membranes.* PhD thesis, Simon Fraser University, 1986.

[57] M Nasir-Uddin and M Morrow. Bicellar mixture phase behavior examined by variable-pressure deuterium NMR and ambient pressure DSC. *Langmuir*, 26:12104–12111, 2010.

[58] J Davis, K Jeffrey, M Bloom, M Valic, and T Higgs. Quadrupolar echo deuteron magnetic resonance spectroscopy in ordered hydrocarbon chains. *Chem Phys Lett*, 42:390–394, 1976.

[59] H Singh, J Emberley, and M Morrow. Pressure induces interdigitation differently in DPPC and DPPG. *Eur Biophys*, 37:783–792, 2008.

[60] R Wittebort, E Olejniczak, and R Griffin. Analysis of deuterium nuclear magnetic resonance line shapes in anisotropic media. *Chem Phys*, 86:5411, 1987.

[61] K Pauls, A Mackay, M Bloom, A Tanjea, and R Hodges. Dynamic properties of the backbone of an integral membrane polypeptide measured by 2H-NMR. *Eur Biophys*, 12:1–11, 1985.

[62] PubChem Compound Database. https://pubchem.ncbi.nlm.nih.gov/compound, 2017.

[63] M Morrow. Transverse nuclear spin relaxation in phosphatidylcholine bilayers containing gramicidin. *Biochim Biophys Acta-Biomembranes*, 1023:197–205, 1990.

[64] B Bonev and M Morrow. Effect of pressure on the dimyristoylphosphatidylcholine bilayer main transition. *Phys Rev E*, 55:5825–5833, 1997.

[65] E Fukushima and S Roeder. *Experimental Pulse NMR: a Nuts and Bolts Approach*. Addison-Wesley, London, 1981.

[66] R Prosser, J Davis, F Dahlquist, and M Lindorfer. 2H nuclear magnetic resonance of the gramicidin A backbone in a phospholipid bilayer. *Biochemistry*, 30:4687–4696, 1991.

[67] A Brown, I Skanes, and M Morrow. Pressure-induced ordering in mixed-lipid bilayers. *Phys Rev E Stat Nonlin Soft Matter Phys*, 69:11913, 2004.

[68] M Urich and A Denton. Swelling, structure, and phase stability of compressible microgels. *Soft Matter*, 12:9086–9094, 2016.